SANDIA REPORT
SAND2012-0886
Unlimited Release
Printed February 2012

Development of a Structural Health Monitoring System for the Life Assessment of Critical Transportation Infrastructure

Andrew N. Daumueller
David V. Jauregui
New Mexico State University

Dennis P. Roach
Sandia National Laboratories

Prepared by
Sandia National Laboratories
Albuquerque, New Mexico 87185 and Livermore, California 94550

Sandia National Laboratories is a multi-program laboratory managed and operated by Sandia Corporation, a wholly owned subsidiary of Lockheed Martin Corporation, for the U.S. Department of Energy's National Nuclear Security Administration under contract DE-AC04-94AL85000.

Issued by Sandia National Laboratories, operated for the United States Department of Energy by Sandia Corporation.

Available to DOE and DOE contractors from
U.S. Department of Energy
Office of Scientific and Technical Information
P.O. Box 62
Oak Ridge, TN 37831

Telephone: (865) 576-8401
Facsimile: (865) 576-5728
E-Mail: reports@adonis.osti.gov
Online ordering: http://www.osti.gov/bridge

Available to the public from
U.S. Department of Commerce
National Technical Information Service
5285 Port Royal Rd.
Springfield, VA 22161

Telephone: (800) 553-6847
Facsimile: (703) 605-6900
E-Mail: orders@ntis.fedworld.gov
Online order: http://www.ntis.gov/help/ordermethods.asp?loc=7-4-0#online

SAND2012-0886
Unlimited Release
Printed February 2012

Development of a Structural Health Monitoring System for the Life Assessment of Critical Transportation Infrastructure

Andrew Nicholas Daumueller
David Villegas Jauregui
Department of Civil Engineering
New Mexico State University
P.O. Box 30001 MSC-3CE
Las Cruces, NM 88003-8001

Dennis Roach
Transportation Safeguards and Surety Organization
Sandia National Laboratories
P.O. Box 5800
Albuquerque, NM 87185

ABSTRACT

Recent structural failures such as the I-35W Mississippi River Bridge in Minnesota have underscored the urgent need for improved methods and procedures for evaluating our aging transportation infrastructure. This research seeks to develop a basis for a Structural Health Monitoring (SHM) system to provide quantitative information related to the structural integrity of metallic structures to make appropriate management decisions and ensuring public safety. This research employs advanced structural analysis and nondestructive testing (NDT) methods for an accurate fatigue analysis. Metal railroad bridges in New Mexico will be the focus since many of these structures are over 100 years old and classified as fracture-critical. The term fracture-critical indicates that failure of a single component may result in complete collapse of

the structure such as the one experienced by the I-35W Bridge. Failure may originate from sources such as loss of section due to corrosion or cracking caused by fatigue loading. Because standard inspection practice is primarily visual, these types of defects can go undetected due to oversight, lack of access to critical areas, or, in riveted members, hidden defects that are beneath fasteners or connection angles. Another issue is that it is difficult to determine the fatigue damage that a structure has experienced and the rate at which damage is accumulating due to uncertain history and load distribution in supporting members. A SHM system has several advantages that can overcome these limitations. SHM allows critical areas of the structure to be monitored more quantitatively under actual loading. The research needed to apply SHM to metallic structures was performed and a case study was carried out to show the potential of SHM-driven fatigue evaluation to assess the condition of critical transportation infrastructure and to guide inspectors to potential problem areas. This project combines the expertise in transportation infrastructure at New Mexico State University with the expertise at Sandia National Laboratories in the emerging field of SHM.

Acknowledgments

This work was sponsored by Sandia National Labs under a Laboratory Directed Research and Development (LDRD) Program and the Sandia Labs Campus Executive Program. The Sandia National Labs Campus Executive for NMSU is Anthony Medina and the Deputy Campus Executive for Engineering is Bob Mata. Their support is gratefully acknowledged. This work would not have been possible without the technical foundation provided by of a number of individuals. Steve Dick provided background information and representative historical train configurations and traffic volumes which were critical to the fatigue evaluation. Ted Keener of Herzog and Jimmy Camp, Ray Trujillo, and Jeff Vigil of the NMDOT assisted in planning the diagnostic load test and gaining access to the steel bridge in Angostura, NM. New Mexico State University also provided additional support through research or teaching assistant positions during much of the time that this research was performed.

THIS PAGE INTENTIONALLY LEFT BLANK

Development of a Structural Health Monitoring System for the Life Assessment of Critical Transportation Infrastructure

TABLE OF CONTENTS

THIS PAGE INTENTIONALLY LEFT BLANK

CHAPTER 1

Background

1.1 Rail Transportation in Northern New Mexico

Prior to 2005, the only passenger trains traveling through New Mexico were the Amtrak Rail Service, which has one northbound and one southbound trip per day on the rail between Belen and Santa Fe, NM. In 2003, Governor Richardson's Investment Partnership Plan (GRIPP) was passed through the New Mexico Legislation, which included creating the Rail Runner commuter rail service between Belen and Santa Fe, NM. In 2006, commuter rail service began from Belen to Bernalillo, and in 2008 service was extended to Santa Fe (Heild 2010). To make this route possible, the State of New Mexico purchased a segment of railroad track from Burlington Northern Santa Fe (BNSF). The portion of the rail used for the Rail Runner totals 99 miles and was purchased in two phases. The first phase stretches from Belen to Bernalillo, NM and the second from Bernalillo to Lamy, NM (Heild 2010). The third phase of the sale stretches from Lamy, NM to Trinidad, CO (about 200 miles) and was added to "close the deal" since BNSF did not want to sell only the railroad between Belen and Lamy (Stone 2006). This third phase of the purchase has not been completed since the state has no clear use for the track. The costs of maintaining this latter portion of the track would exceed $8.5 million per year. Potential environmental issues exist in some areas of this third phase (Heild 2011), further dissuading the state from closing this deal. In addition to the existing track, some new rail and bridges were constructed between the Tewa Pueblo and Santa Fe to make the Rail Runner route more efficient.

This commuter route was created to reduce traffic on the interstate between Albuquerque and Santa Fe, NM since this is a very busy commuter route. The estimated travel time from

downtown Albuquerque to downtown Santa Fe was projected to increase from 75 minutes in 2004 to 104 minutes in 2025 according to the *Final Alternatives Analysis* report prepared by URS Corp. (2005). This can be attributed, at least partly, to the fact that there are many government jobs in Santa Fe since it is the state capital, but a lower cost of living in Albuquerque, Bernalillo, and Belen, encourage commuter traffic.

1.2 Inspection of Railroad Bridges

Railroad bridges must be inspected at regular intervals to ensure that major deterioration does not occur without the knowledge of the owner. The components inspected and the types of flaws to be detected vary depending on the type of structure. Inspectors are trained to identify potentially dangerous conditions, typically using visual inspection supplemented by visual enhancement tools. Until recently, railroad bridge inspection frequency and reporting requirements were not established by federal law, but rather by the owners of the railroads who have the greatest incentive to ensure the safe passage of trains. However, as a result of a catastrophic bridge failure in 2007 along with findings that various small railroad owners did not have sufficient bridge management programs in place, the Federal Railroad Administration (FRA) issued regulations in the *Federal Register* (2010). These regulations include a requirement that bridge inspections must take place every calendar year and no more than 540 days apart. There are also regulations in place that specify the qualifications for the bridge inspector and engineer involved in the work.

For steel bridges, inspection of the superstructure tends to focus on corrosion and cracking of the steel members. If cracks are found in steel members, the situation must be addressed quickly, since fatigue can lead to catastrophic failure. Corrosion can also lead to failure; however the development of corrosion to critical levels may take much longer than the

propagation of a fatigue crack. Many other conditions must also be evaluated as part of a standard inspection, including loose connections, bearings that are not moving freely, and settlement of the foundation. During an inspection, the inspector takes note of any conditions that require attention or monitoring. The observations made by the inspector are then used to create an inspection report, which includes condition rating which is a single digit that describes the condition of a member, the bridge location, the bridge number, the date inspected, and recommendations for repairs based on the findings from the inspection. Bridge inspections are helpful to the engineer evaluating the structure for strength and service since the geometry of the structure can be verified and any conditions that are not in the plans (e.g. loss of cross section from corrosion) can be located and quantified.

1.3 Evaluation of Railroad Bridges

Upon initializing the acquisition of the rail mentioned previously, the State of New Mexico released a request for proposals for inspection and evaluation of the bridge structures on this rail line. The winner of this bid was Wilson & Company, Inc., who subsequently subcontracted with the Department of Civil Engineering at New Mexico State University (NMSU) to load rate the steel bridges on this line, along with some of the prestressed concrete bridges. The evaluation of these structures required modifying the NMSU procedures developed to evaluate highway bridges (Castro 2008) due to differences in load distribution and dynamic impact factors. Many of the steel structures were evaluated using Virtis (AASHTOWare 2010), which is a software package designed for load rating of highway bridges. This work is described in detail in the master's thesis of Muro Villanueva (2010). The load ratings performed for these bridges only evaluates the strength of the structures but does not consider fatigue. To obtain a

remaining fatigue life, further analysis must be performed. This fatigue analysis to assess remaining life will be described in more detail in chapter 6.

Virtis could not be utilized for the more complex structures that NMSU was contracted to rate, namely the steel through-girder and through-truss bridges, because the highway-specific loading models used by the program allow the rating vehicle to move transversely to maximize the effects on each member, however for the railroad, the path is predetermined. A through-girder bridge has two main load carrying members that span the entire length of the structure and floorbeams that run in the transverse direction. The deck is directly supported by the floorbeams for one configuration of the through-girder bridge. Other through-girder bridges also include longitudinal stringer members which carry the deck and frame into the transverse floorbeams (see figure 1.1). Through-trusses are similar; however, the main girders are replaced with trusses.

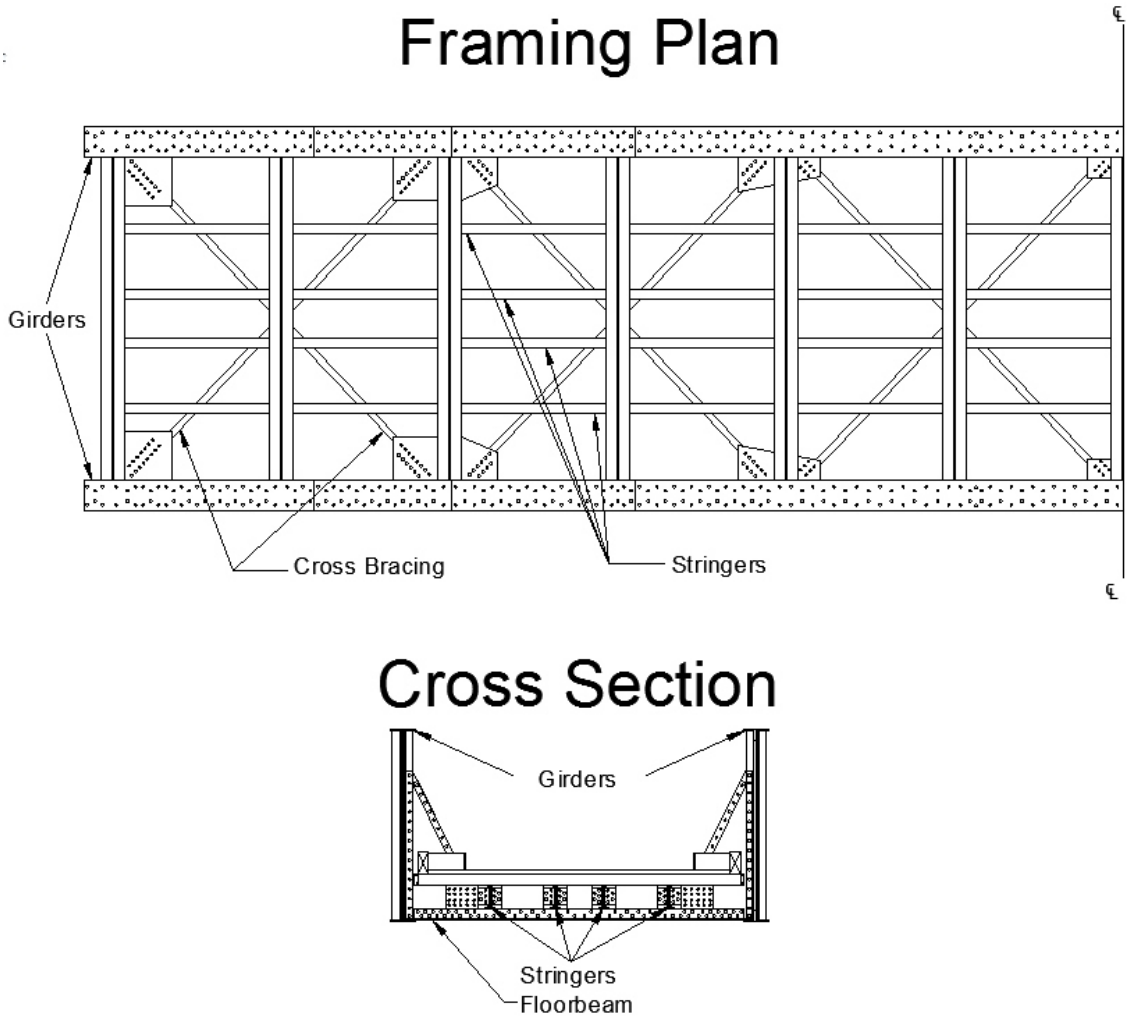

Figure 1.1: Through girder floor system.

1.3.1 Evaluation for Strength

For through girder bridges a two-dimensional structural analysis is performed to determine the shear forces and bending moments in the stringers (if present), floorbeams, and girders. For load rating purposes, the structure is analyzed under dead load (including the weight of the structural members, deck, ballast, ties, and rails) and live load (including the standard E80 and alternative rating vehicle). The section properties (mainly the section modulus about the weak and strong axes, cross-sectional area, and shear area) of all the load carrying members are also determined. Dead and live load stresses are then calculated at the tenth points and at all changes in the cross-

section. The allowable stress rating (ASR) equation is then used to determine the rating factors at each of the various locations and estimate the load carrying capacity of the structure at each of the various locations as follows:

$$Rating\ Factor = \frac{\sigma_{all} - \sigma_{dead}}{\sigma_{LL+IM}} \quad \text{EQ 1.1}$$

where the rating factor is a value that indicates the suitability of the structure for a given load; σ_{all} is the allowable stress (which is determined based on the type of member and force effect), σ_{dead} is the stress in the member due to dead loads, and σ_{LL+IM} is the stress in the member due to the applied live loads plus the dynamic impact factor. The rating factor equals 1.0 when the applied dead load and live load plus impact cause the stress in the component to equal the allowable stress minus the dead load stress. The rating factor is multiplied by 80 to obtain the bridge capacity in terms of a Cooper E loading, which is the standard way to report ratings for railroad bridges. A Cooper rating of E80 corresponds to a structurally sound bridge designed to current standards.

In the computation of the load ratings, there are two levels at which the allowable stress is determined; one corresponds to the "normal" rating and the other the "maximum" rating. The rating factor obtained for the "normal" rating represents the maximum load that can be carried safely on a regular basis. The rating factor obtained for the "maximum" rating indicates the heaviest vehicle that can safely cross the bridge at infrequent intervals, as defined by the engineer. Frequent loading at the maximum rating level is likely to reduce the useable life of the structure due to fatigue (AREMA 2007).

1.3.2 Evaluation for Fatigue

Aside from strength, it is often necessary to perform a fatigue evaluation to estimate the remaining fatigue life of a steel structure. There are a number of ways to estimate the remaining

fatigue life and these will be discussed in detail in Chapter 2. A fatigue evaluation can be used to estimate if and when a structure will crack due to fatigue of the metal. The simplest way to perform a fatigue analysis is to determine the areas that are critical for fatigue, determine the imposed nominal stress (without considering stress concentrations) at these locations, identify the fatigue category of the detail at each location, and then find the maximum stress that allows for infinite life for that fatigue category (stress levels below that which is necessary to produce crack onset and growth). If the computed stress range caused by the rating vehicle is less than the maximum stress range for infinite life for the detail at that location, infinite life is declared. If infinite life cannot be declared, either a fracture mechanics approach or an approach based on S-N curves can be adopted to determine the remaining life of the member. Fracture mechanics methods can be used to estimate the rate of crack growth based on a detailed analysis of the connection being considered. One major drawback to fracture mechanics methods is the relatively large amount of information and sophisticated analysis required, which makes this method unsuitable for routine evaluation. The simpler method for evaluating the remaining fatigue life, and the one outlined in the AREMA (2007) specification, is to use curves that relate the estimated stress range (S) to the number of cycles to fracture (N) corresponding to the type of metal and type of detail under consideration. These charts are called S-N curves and are widely used for fatigue evaluation. The remaining life of a structure that experiences variable loading (which is the case for all bridges) is typically estimated using one of two methods. With the first method, an effective stress range is determined based on measured or simulated traffic data. The effective stress range is the constant amplitude stress range that causes the same fatigue damage as the actual loading. The second method uses Miner's rule which is a summation of the number of stress cycles at each of the stress range magnitudes divided by the corresponding number of

cycles that can be withstood at that magnitude. For both of these methods, rainflow counting can be used to obtain the stress ranges required. See Chapter 2 for more details on the methods used for fatigue evaluations.

A fatigue analysis requires a good estimate of the traffic that has previously crossed the structure and that will cross the bridge in the future. A model that can accurately simulate the stresses experienced under these loads is also needed. Traffic estimates can be obtained from the owner of the structure, or the current traffic can be measured and a rate of traffic growth (e.g. a 5% increase in weight per vehicle and/or number of vehicles per year) can be used to estimate historic and future loads. The structure can be modeled in a simple way that will yield conservative results, or a more complex and accurate model can be developed and calibrated using a controlled load test. To develop the most representative model, sources of uncertainty that may be encountered must be accounted for appropriately.

1.4 Uncertainties in Railroad Bridge Behavior

Previous work has shown that the simplified methods used by bridge engineers to estimate the stresses in structural members of railroad and highway bridges tend to overestimate the actual stresses encountered in the field (Imam et al. 2008). One possible explanation for this is that connections that are assumed to be pins in design calculations actually behave as semi-fixed joints. Another possible explanation for the reduction in measured strains is that the ballast significantly dampens the vertical impact on the structure, thus reducing the actual stresses in the structure. Still other possible causes of these discrepancies include unintended composite action of members, support restraint, and incorrect assumptions about load distribution (Imam et al. 2008). Of these, two that appear to have the strongest effect on the measured strains are the floor system connections and improper modeling of load distribution and impact.

1.4.1 Floor System Connections

One structural detail that has the potential to be a fatigue concern is the riveted double-L connection (see figure 1.2) between the stringers and floorbeams that is common in steel railroad bridges constructed in the late 1800s and early 1900s.

Figure 1.2: Example of a riveted double L stringer to floorbeam connection (the same detail is present on other side of the stringer).

This connection is generally assumed to provide no rotational stiffness in design; however, it has been found that these connections can develop a significant level of fixity (Al-Emrani and Kliger 2003). In cases where significant negative moments develop at these connections, fatigue can become an issue. This is because transverse and short longitudinal floor system members experience a relatively large number of cycles at a relatively high stress range since they are likely to be fully loaded and unloaded with each passing axle. In addition, the fatigue category for this type of detail is Class D, which furthers the criticality of this detail for fatigue (AREMA 2007). There have been a significant number of documented fatigue failures at riveted double-L connections such as the one shown in figure 1.2 as a result of the connection fixity (Al-Emrani and Kliger 2003). The fixity causes significant stress in the clip angles and in the rivets, leading to fatigue cracks at the corner of the L members and at the rivet heads (Al-Emrani and Kliger 2003) (see figure 1.3).

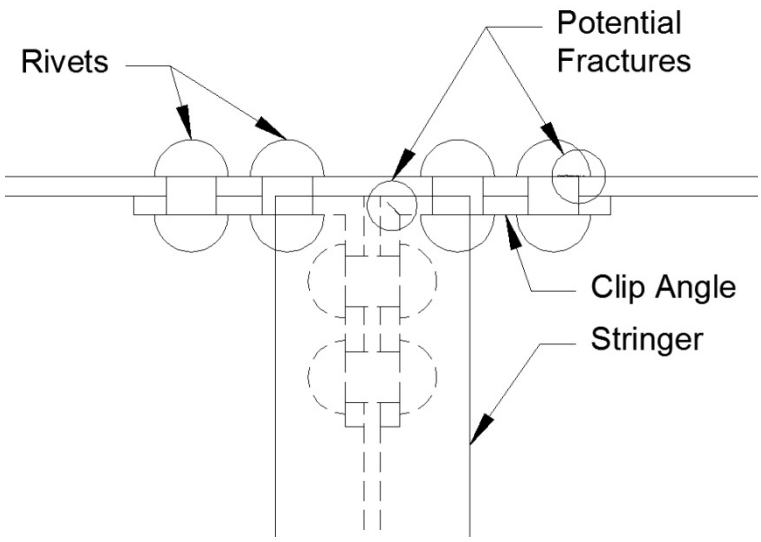

Figure 1.3: Potential fracture locations for riveted double angle.

Another implication of the fixity of the riveted connections is that the actual stresses in the members away from the connections will be lower than what is calculated assuming that the connections act as pins (Philbrick et al. 1995).

To obtain a realistic estimate of the remaining life of a steel railroad bridge built in the late 1800s, the double-L connections are a detail that should be studied closely for fatigue performance. The allowable stress range for infinite fatigue life, based on a riveted class D fatigue detail (more information is provided on fatigue details in Chapter 2), for over 2 million cycles is 6 ksi (48 MPa). This is less than 25% of the yield stress of the steel used in many railroad bridges (AREMA 2007). Thus, it is likely that this stress level will be exceeded.

Aside from the connections, the flange plate cutoff locations and midspan of the riveted built-up members are potential critical locations for fatigue. According to the *AREMA Manual* (2007), tension on the net section of riveted members fall into the fatigue category D, which is a more critical category in terms of stress range compared to category A which corresponds to the gross section.

1.4.2 Load Distribution and Impact

For railroad bridges with ballasted decks, the complexity of the finite-element model may need to increase in order to properly capture the load distribution between the rails, ties, ballast, and deck. In the *AREMA Manual* (2007), the axle loads are distributed evenly in the transverse direction to all members supporting a track (i.e. 25% of the axle load to each of 4 stringers, and half the axle load to each of 2 girders) which can be seen in figure 1.4. In the longitudinal direction, an axle load may be applied as a single point load (recommended) or evenly to each of the three closest rail ties (AREMA 2007). Some researchers have modeled the track, ties, and ballast in an effort to more accurately capture the distribution of load to the underlying bridge elements. Modeling of the ballast is complex, however, since the behavior of fill materials is much more variable than engineered materials and since crushed stone ballast is a nonlinear material. Ballast decks, or bridge decks that carry ballast between the deck and the rail ties, have been modeled through the use of springs under the railroad ties (Lee and Chiu 2005), or elastic solid elements for the ballast, ties, and rail (Yang et al. 2009).

a)

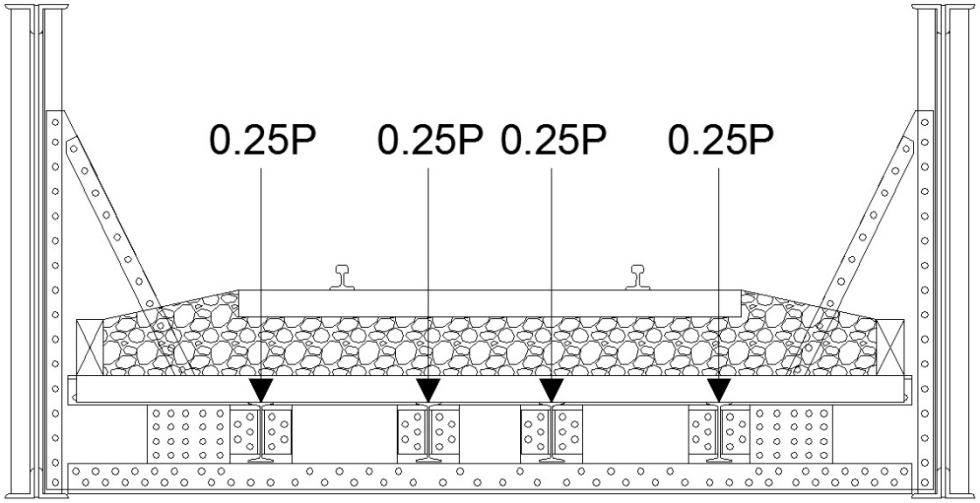

b)

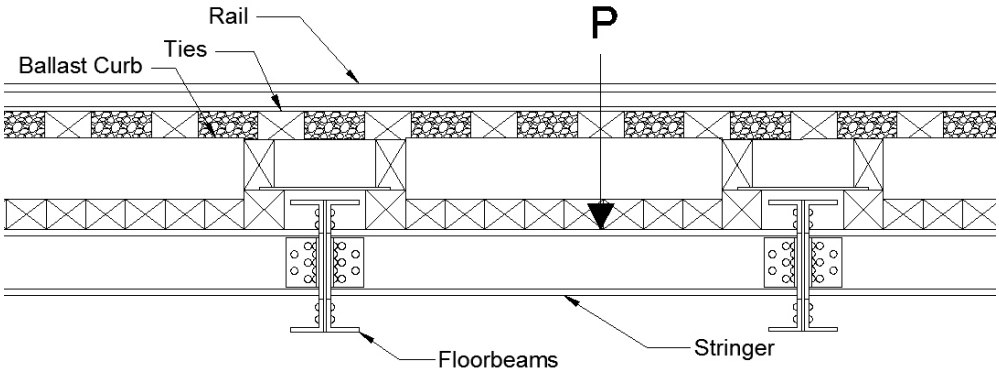

c)

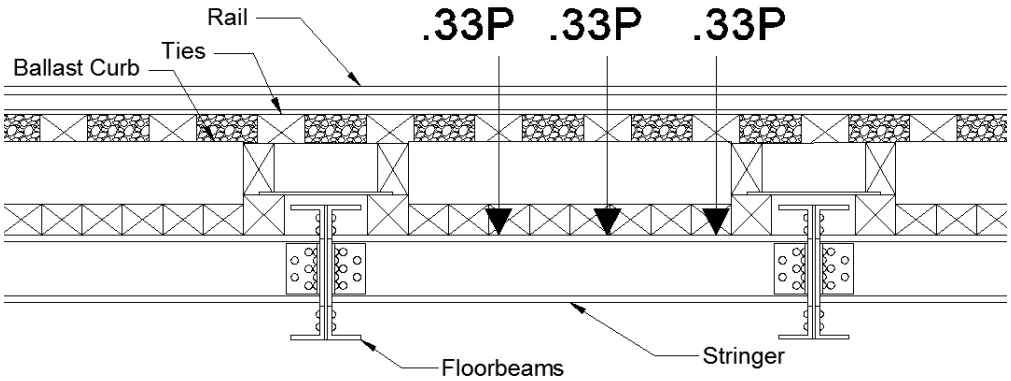

Figure 1.4: Illustration of AREMA load model: a) Standard AREMA transverse load distribution b) Standard longitudinal load distribution c) Modified longitudinal load distribution.

The presence of ballast on the deck of railway bridges also greatly reduces the dynamic impact on structural members. This has been shown by DeCorte and VanBogaert (2006) who measured the stresses in the steel orthotropic deck of a ballasted-deck railroad bridge in Belgium. It was found that the ballast was beneficial in reducing the stress ranges experienced by the deck structure because it spread the load longitudinally and transversely and dampened the vertical impact imparted by the train (DeCorte and VanBogaert 2006). Hence, the presence of ballast may greatly reduce the actual stresses experienced by the structural members, and increase the remaining fatigue life of these structures.

1.5 Bridge Management

As the infrastructure owned by an agency ages, it is important to have the ability to accurately prioritize maintenance, rehabilitation and replacement activities based on sound engineering judgment. The ideal circumstance would be to have knowledge of the expected remaining service life of each structure (based on its current condition) along with the limiting factor such as fatigue, steel corrosion, or concrete decomposition due to sulfide or chloride intrusion. This knowledge could be used to make appropriate decisions to retrofit, rehabilitate, or replace a structure so that resources can be allocated appropriately. Structural Health Monitoring (SHM) can be very helpful in addressing this concern, particularly if a portable (i.e., capable of being used on multiple structures) system were in place that could be used to assess the health of multiple structures. Bridge management software capable of interpreting and using the information gathered from SHM systems could then determine the expected remaining life of structures based on fatigue models and/or corrosion models in addition to considerations such as functional obsolescence and structural deficiency. If such a system were available, a great deal

of expense would be spared since structures would not be replaced simply because of age, but because the structure is rationally shown to be insufficient for continued service.

There are various methods used for bridge management. When considering a relatively short stretch of railway or highway, the management process can be simplified somewhat for portions of rail or highway that experience the same traffic. In these cases, load monitoring only needs to be performed at one location to determine the loads traversing that particular stretch of rail or highway. If desired, the information gathered from load monitoring can be used to determine a site-specific fatigue vehicle, which can be used to perform a more accurate fatigue evaluation, rather than the standard fatigue vehicle from the AASHTO or AREMA design manuals (Laman and Nowak 1996). The actual traffic loads determined from load monitoring data can also be directly applied to a structural model which can be developed for each structure along the line. The models created can be used to estimate the remaining fatigue life and to perform a load rating (Mencik et al. 2007).

Various computer programs have been developed for the purpose of bridge management. One of the more established programs in the U.S. is Pontis, which is utilized by state departments of transportation for the management of highway bridges. This program takes various inputs (some of which are qualitative ratings based on the observations of bridge inspectors), and determines a sufficiency rating which is a score from 0 to 100. A state can then use the sufficiency rating to prioritize repair and replacement activities (http://www.fhwa.dot.gov/infrastructure/asstmgmt/pontmore.cfm 2011). Other bridge management programs have been proposed in the literature. Sharma and Choros (1996) reported on a computer program developed by the Association of American Railroads (AAR) that can be used to estimate the remaining fatigue life of railway bridges using information provided about

the member or detail of interest and the estimated historical, current, and future loading. This program uses rainflow counting and Miner's rule to estimate the remaining fatigue life (Sharma and Choros 1996). Another research program that could be adapted for more widespread use was performed by Tobias and Foutch (1995) which involved instrumenting a number of structures to collect data representative of the location of interest. Once the data was gathered and the model for each bridge calibrated, the remaining fatigue life of the structures could be estimated and the probability of an overload could also be predicted (Tobias and Foutch 1995). Farhey (2005) discusses the usefulness of SHM technology to reliably determine the condition of the structures under investigation and how prognostic bridge management should be the ultimate goal. Farhey (2005) also discussed the shortcomings of long-term monitoring of bridges including the fact that many sensor types require periodic recalibration. In the literature, there did not appear to be any bridge management software that incorporates a fatigue model along with a damage model for the aging of the structural materials. This would be a valuable contribution for agencies that have a large number of metallic structures, particularly when many of those structures are relatively old and susceptible to fatigue and corrosion. The repair and maintenance of these structures could be planned using a condition-based method as opposed to a time-based method which may take a structure out of service significantly earlier than what is required based on its condition. A program to predict the remaining life could also be helpful in identifying structures that may have a shorter life than initially expected.

In addition to planning maintenance and repairs, bridge managers need to dictate the inspection intervals. This is currently done according to Federal guidelines. For highway bridges, the typical inspection interval for a structure is 24 months unless there is a need for more frequent inspection, in which case a 12 month interval is used (Code of Federal Regulations

2006). For railroad bridges, a 12 month frequency is used unless a shorted interval is required (Federal Register 2010). For other structures, such as aircraft, it may be common to determine the inspection interval based on a fracture mechanics study of a particular detail. Using this approach, the time between a crack becoming detectable and failure is determined, and the inspection interval is set such that two inspections occur during this period (Roach and Rackow 2007).

1.6 Goals and Objectives

The goal of this study is to contribute to the fields of SHM, bridge inspection, and bridge management by developing an efficient method for evaluating steel bridges for fatigue and developing recommendations for applying the results to bridge inspections. To do this, the following objectives must be met: 1) Research the work of others in the areas of fatigue and SHM; 2) Develop an advanced structural model that accurately describes a structure; 3) Perform a load test to validate the model; 4) Perform a fatigue evaluation to determine the estimated remaining life for the structure; 5) Use these results to make conclusions about the current health of structures and to guide inspectors to potential critical locations which should be closely monitored for signs of distress.

1.7 Report Layout

This report is divided into 8 chapters. The first chapter was an introduction and background of the topics to be discussed throughout the report. Chapter 2 covers the methods available for fatigue analyses and concludes with a recommendation for the method best suited to evaluating railway bridges. Chapter 3 discusses various SHM methods and systems and the advantages and disadvantages of each. Chapter 4 describes the specific bridge used for this study and the load testing procedure and results. Chapter 5 covers the analytical model produced

to simulate rail traffic on the structure and evaluates how well the simulated data matched the measured data from the load test. Chapter 6 discusses a load rating method for fatigue that compares the effective stress range to the constant amplitude fatigue limit (CAFL). Chapter 7 gives details about the fatigue life estimation for a structure and the results thereof. Finally, Chapter 8 discusses the conclusions drawn from the work performed and gives recommendations for the application of the methods developed for this study.

THIS PAGE INTENTIONALLY LEFT BLANK

CHAPTER 2

Fatigue Evaluation

2.1 Load Induced Fatigue

In many steel structures, particularly those constructed with "brittle" steel and/or poor connection details, one of the most likely factors to limit the life of the structure is fatigue. The term "Fatigue" can be defined as "the progressive, localized, permanent structural change that occurs in a material subjected to repeated or fluctuating strains at stresses having a maximum value less than the tensile strength of the material" (Boresi and Schmidt 2003). There are two basic approaches for estimating the remaining fatigue life of a structure with a given detail. The first is to utilize charts that plot the number of cycles that a detail is expected to withstand before failure as a function of the constant stress amplitudes (S-N curves). The second approach uses methods that implement fracture mechanics. An accurate estimate of the remaining fatigue life of a structural detail can be extremely useful in prioritizing bridge rehabilitation and replacement intervals, and in ensuring the safety of the structures. Fatigue life is difficult to evaluate accurately because factors such as the initial size of voids or cracks in a weld and the stress concentrations at a particular detail can only be approximated and are dependent on various factors. As a result, experimental S-N charts have a large degree of scatter. For this reason, many studies in the literature use random variables to account for the probabilistic nature of the fatigue problem.

Perhaps the simplest and most practical approach to estimate the remaining fatigue life of a bridge is to determine the stress ranges at critical details under a standard fatigue vehicle, which is meant to conservatively approximate the effect of routine traffic on the structure. Once the stress range is determined, the corresponding S-N curve (see Figure 2.1) can be used to

estimate the total number of cycles that can be withstood by a particular detail under the design fatigue vehicle.

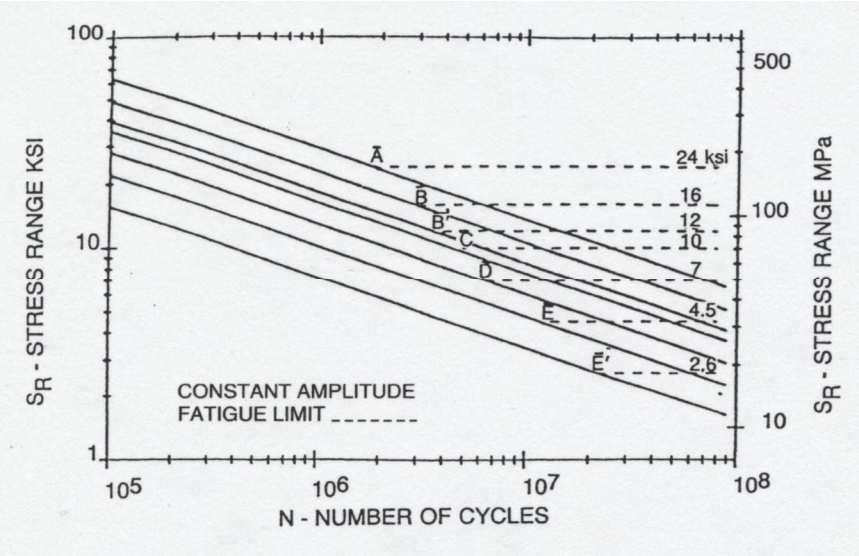

Figure 2.1: Design S-N curves from AREMA (2007).

The life of the structure can be estimated by dividing the total number of cycles to failure by the number of cycles anticipated annually. The S-N curves provided in the AASHTO and AREMA codes plot the number of cycles to failure with respect to the constant amplitude stress range for various fatigue categories (see figure 2.1). The fatigue categories represent the different types of details that are used in bridge construction and are specified as categories A, B, B', C, C', D, E, and E' from best to worst, based on the stress concentration and other geometric considerations at the detail. For instance, the net section of a riveted connection (e.g. riveted cover plates and double angle connections) falls under category D while plain rolled or cleaned members (e.g. steel plates or rolled sections with no holes, welds, notches, etc) fall under fatigue category A (see figure 2.2). In recent codes, the design for infinite life has become popular, which requires that the maximum stress range for a tensile component to be less than the constant amplitude

fatigue limit (CAFL) or some fraction of it. The CAFL is plotted in figure 2.1 as a dotted horizontal line for the corresponding fatigue detail category.

a)

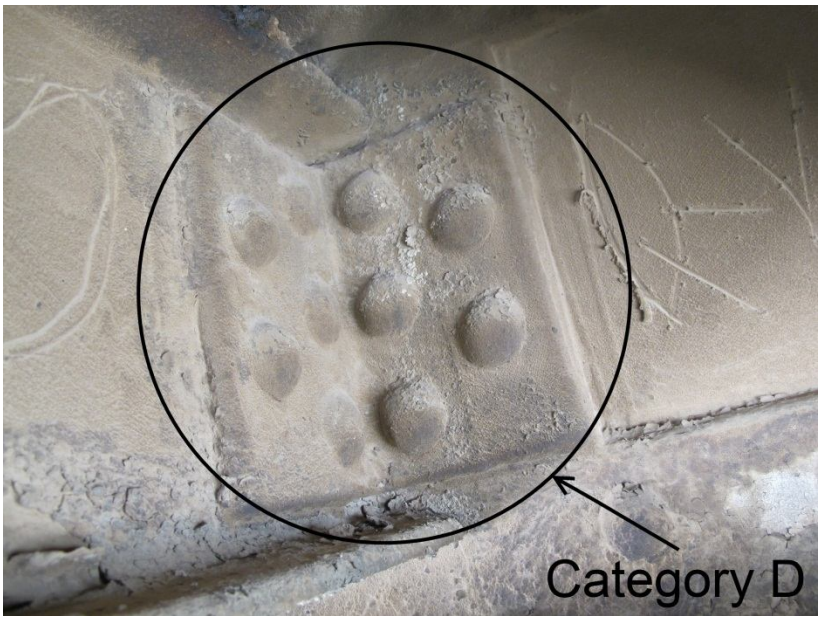

b)

Figure 2.2: Fatigue details in riveted railroad bridges. a) Typical stringer-to-floorbeam connection (category D). b) Typical stringers (category A).

The S-N curves can also be used along with measured strain data to approximate the fatigue life of an element by estimating the number of stress cycles within various stress range magnitudes. To this point in the discussion, only one stress range is used to describe the fatigue susceptibility of a member. This is reasonable when checking for infinite life using the AASHTO or AREMA code since the loading is conservative and every loading cycle is assumed to have the same magnitude (i.e. the design fatigue truck passes over the bridge 2 million times). In reality, the loading that a bridge experiences will be variable since not all trucks crossing a bridge will have the same weight and configuration. Therefore the actual stress history must be reduced to the number of stress ranges experienced at various magnitudes. Rainflow counting is a method used for calculating the number of stress cycles for various stress range magnitudes (e.g., the number of stress cycles experienced between 1 ksi and 2 ksi in a measured or simulated stress history). Once the numbers of cycles for various stress range magnitudes are found, Miner's rule (which is discussed in detail in Section 2.1.1) can be used to determine the accumulated fatigue damage of a detail for variable amplitude loading and estimate the remaining fatigue life.

As mentioned earlier, methods that implement fracture mechanics can also be used. In using a fracture mechanics approach, the problem may be split up into two parts, crack initiation and crack propagation. In practice, an initial flaw size is often assumed, and therefore the time required for crack initiation is zero. Methods to describe crack propagation typically implement the work of Paris (1961), which related the rate of fatigue crack growth to the geometry of the detail, the magnitude of the stress range, and the material used. Paris' law (1961) assumes that there is an initial flaw in the detail with a finite size such as micro cracks caused by welding or by punching holes. This initial crack size is important in determining the number of cycles to

failure, and therefore must be estimated accurately. For bridges, it is much simpler to perform the analysis using S-N curve based methods since the AREMA (2007) and AASHTO (2010) codes include provisions for fatigue that use this methodology.

2.1.1 S-N Curve Based Methods

A significant amount of research has been focused on predicting fatigue induced-failure since fatigue can cause sudden failure and since this issue is more complex than many others in the area of structural performance. In the early 1970s, Fisher et al. (1973) performed tests on various details used in steel construction, and subsequently developed a series of curves that relate a given constant amplitude stress range to the corresponding number of cycles to failure for a particular material. As stated earlier, these curves are referred to as S-N curves (see figure 2.1). It has been shown that the primary factors that dictate the fatigue life are the stress range magnitudes, the detail geometry, and the manner in which the members are connected since stress intensity factors are significantly affected by these factors. Previous research has also shown that full-sized specimens (as opposed to scaled-down specimens) of similar geometry and material characteristics as the actual member must be tested to obtain the representative performance. This is because larger specimens are more likely to have realistic flaws which are the starting points for fatigue cracks (Imam et al. 2008). In the design codes for railroad bridges (AREMA 2007) and highway bridges (AASHTO 2010), S-N curves developed by Fisher et al. (1973) are referenced for various fatigue categories (see Figure 2.1). The S-N curves were developed through regression of test data and are linear when plotted on a log-log scale from N = 1 to the knee point, which varies depending on the detail of interest (see Figure 2.1). In the AREMA and AASHTO specifications, for increasing cycles beyond the knee point, the curve is either constant (in which case the value of the stress range at this point is called the constant

amplitude fatigue limit, or CAFL, as shown in figure 2.1) or continues at the same slope. It has been shown that the CAFL must be ignored when more than ≈ 0.01% of the stress cycles exceed the CAFL when the detail experiences variable amplitude loading (Imam et al. 2008). For railroad bridges this is often the case due to variability in the weight of rail cars.

The S-N curves provided in the AREMA and AASHTO codes can be used to estimate the remaining fatigue life of a structure in various ways. In bridge design, a connection detail may be designed for infinite life, which is done by ensuring that the expected effective stress range, S_R, for a tensile component under a standard fatigue design vehicle is less than 50% of the CAFL for the particular detail (AASHTO 2007), or under a pre-determined stress range (AREMA 2007) as shown in table 2.1.

Table 2.1: Allowable fatigue stress range (ksi).

Stress Category	No. of Constant Stress Cycles, N	
	2,000,000	>2,000,000
A	24	24
B	18	16
B′	14.5	12
C	13	10 or 12 (Note 3)
D	10	7 (Note 4)
E	8	4.5
E′	5.8	2.6
F	9	8

Note 1: This table is based on bridges designed for live loading specified in Article 1.3.13e. For bridges designed for other live loadings see Part 9, Commentary, Article 9.1.3.13.
Note 2: For Fracture Critical Members, See Article 1.3.13i
Note 3: For transverse stiffener welds on webs or flanges.
Note 4: For base metal in members with riveted or bolted connections with low slip resistance, use the variable amplitude stress range of 6.

Table 15-1-10 (AREMA 2007)

For riveted through-girder bridges, notes 2 and 4 may apply since the girders are considered fracture critical and since the slip resistance is unknown in the riveted connections. In order to be conservative the slip resistance in the connections are assumed to be low. Note 2 refers to a

provision that states that category E and E' connections are not appropriate for fracture critical members and that category D connections should be discouraged (AREMA 2007). If higher stress ranges are expected than the limits given in table 2.1, the fatigue life must be calculated. Either a standard fatigue vehicle or an estimated traffic model may be used to obtain a stress history to be used in the fatigue evaluation. Once the number and range of the stress cycles are determined, Miner's rule (Miner 1945) can be applied or the effective stress range can be determined and used to estimate the remaining life of the structure.

To estimate the remaining fatigue life of existing structures based on actual traffic data, two methods are commonly implemented. The first method directly applies Miner's rule (Miner 1945). First, the stress ranges are determined based on measured strain histories, which are further analyzed using a rainflow counting method to determine the number of cycles at each stress range magnitude (Caglayan et al. 2008). The rainflow counting method involves measuring or simulating a stress history. Then the stress history is reduced to local maxima and minima, or turning points. These turning points are plotted and the graph is rotated 90 degrees clockwise as shown in Figures 2.3 to 2.5. Stress ranges are determined by imagining the graph to be a solid surface, and following the "rainflow" until it falls off the page or collides with the "flow" from above.

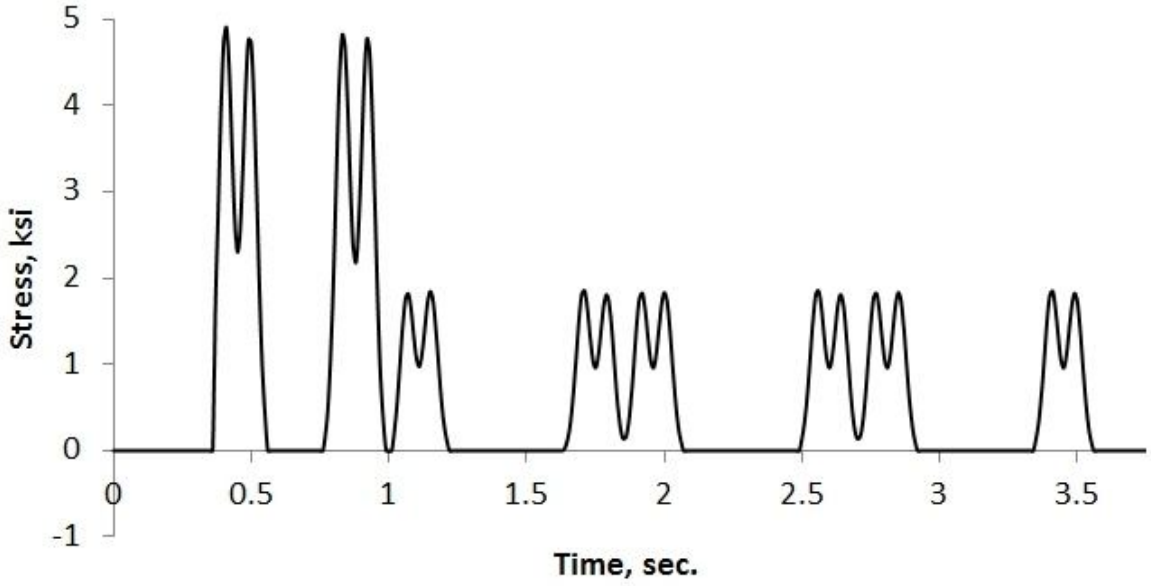

Figure 2.3: Original stress history.

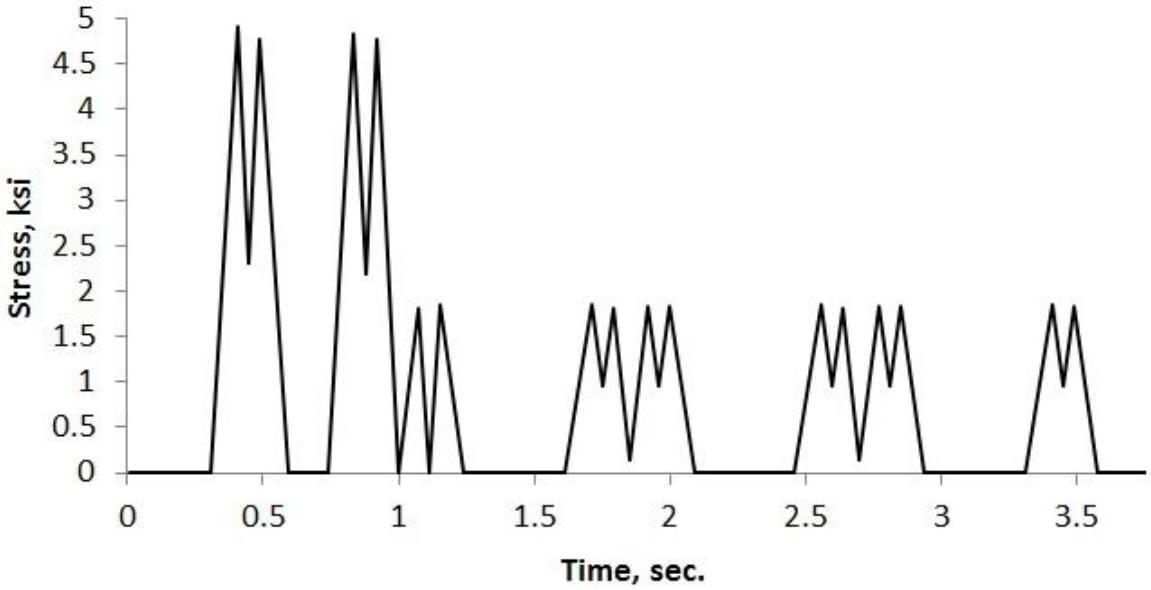

Figure 2.4: Stress history reduced to turning points.

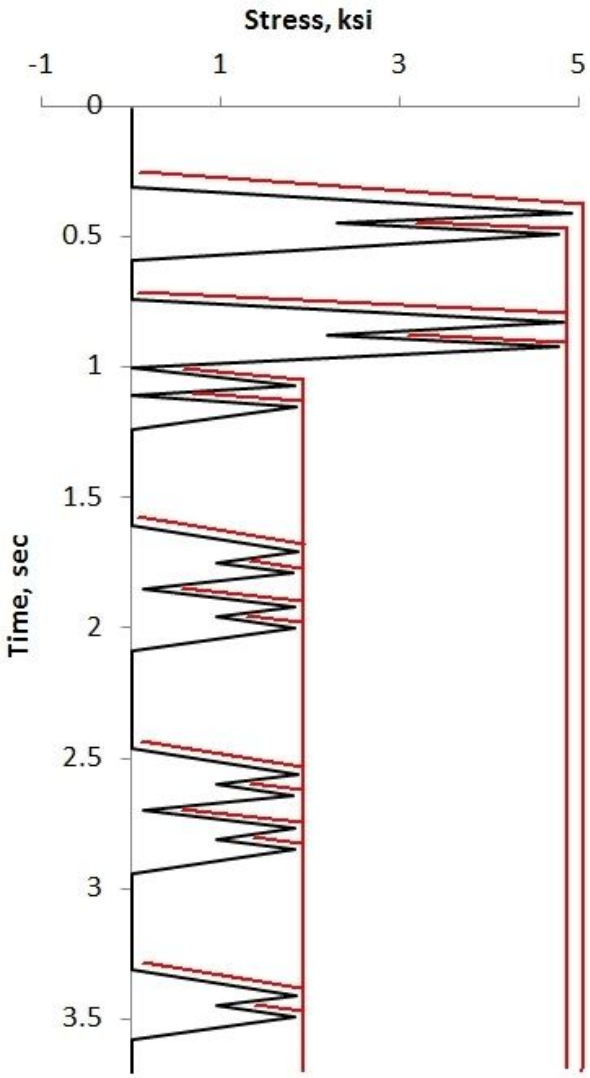

Figure 2.5: Representation of rainflow counting (only tension half cycles illustrated).

Each turning point is the starting point for a stress range, as seen in Figure 2.5. The horizontal distance it flows before falling off the page or running into another "flow" is the magnitude of one half-cycle. Tension and compression half cycles of the same magnitude are paired to make full cycles. Stress range "bins" are then created, which represent the number of stress cycles of a certain range of magnitudes. For example, all stress ranges with magnitudes between 1 ksi and 2 ksi are all grouped together in one "bin". When performing later calculations, all cycles in each "bin" are treated as if they have the same magnitude, which would be 1.5 ksi for this

example. Once the number of cycles in each "bin" of stress ranges is determined, Miner's rule (Miner 1945) may be applied which states that

$$D = \sum_i \frac{n_i}{N_i} \quad \text{EQ 2.1}$$

where D = the damage accumulated (a value of unity theoretically indicates failure); n_i is the number of cycles at the i^{th} stress range magnitude; and N_i is the corresponding N value from the S-N curve at the i^{th} stress range magnitude (Miner 1945). However, it has been found that Miner's rule can be unconservative when variable amplitude loading is present (Agerskov 2000), particularly when the magnitudes of the stress cycles increase over time. In such circumstances, a value for D less than unity is a better indicator of failure. Imam et al. (2008) recommended using a lognormal distribution for D with a mean of 0.9 to take into account the possibility of Miner's rule being unconservative. A value of 0.30 for the coefficient of variation of D at failure has been found to be reasonable by Wirsching (1995).

The second method is essentially a rearrangement of Miner's rule in which an equivalent constant amplitude effective stress range is determined and applied along with the S-N curve to estimate the remaining fatigue life. The effective stress range represents the root mean cube of the stress ranges and is calculated as follows:

$$S_{Re} = \left(\sum_i \left(\frac{n_i}{N_{total}} S_i^3 \right) \right)^{1/3} \quad \text{EQ 2.2}$$

where n_i is the number of cycles at stress magnitude S_i; N_{total} is the total number of stress ranges of all magnitudes; and S_{Re} is the effective stress range (Dexter et al. 2004). To accurately represent the effective stress range, it is important to include all stress ranges since it has been found that stress cycles can be considered damaging if at least 0.01% of cycles exceed the CAFL (Dexter et al. 2004).

The methods mentioned above are based on Miner's rule and may be applied using simulated or measured data. The simulated number and magnitude of stress cycles from a fatigue design truck can be used; however this is typically conservative since the design truck is often heavier than typical traffic and the relatively simple models used for determining the stresses in members often overestimate strains. To more accurately estimate the remaining life of the structure, actual traffic loads (along with simulations of historical and future traffic) can be used. It is recommended that a relatively simple preliminary fatigue evaluation be conducted to determine if the structure satisfies the infinite fatigue life requirements using the standard fatigue design truck when initially evaluating a structure for fatigue. If the existing structure has components that do not satisfy the infinite life requirements based on the preliminary evaluation, a more in-depth fatigue study may then be performed to more accurately determine the actual stresses the structure experiences under traffic. The results of the advanced analysis are likely to be less severe than those determined under the standard fatigue design loading and are more representative of the true remaining life of the structure.

The S-N curves used in fatigue analysis were developed for a particular detail category and material, and as such require no adjustments to account for the stress concentration or fracture toughness. For a detail for which there is no S-N curve available, a "hot spot" analysis may be performed. A "hot spot" analysis uses a single S-N curve for the connection in a nominal stress field (with no stress concentrations). The stress used when going to the S-N curve is the actual stress, which is obtained by taking the nominal stress and using the appropriate stress concentration factor for the detail under investigation (Connor and Fisher 2006). The adjustment is difficult to quantify and is dependent on the method used to acquire it. The stress concentration factor (SCF) determined through modeling will vary significantly depending on

the mesh size used in the model. The problem is similar if the SCF is determined through measurements since the strain gauge used has a finite size, and therefore cannot necessarily measure the absolute highest strain. Another problem with this type of analysis, however, is that it specifies using a single CAFL for all details, which is not accurate (Connor and Fisher 2006).

Due to the random nature of live loads and the random distribution of flaws within metallic details, probabilistic methods are often used to estimate the remaining fatigue life of a structure. Even the methods that are deterministic in their application use S-N curves that are based on a predefined confidence level and probability of failure. Since experimental data displays significant scatter in terms of the fatigue life, AREMA (2007) uses a 95% confidence limit for 95% survival based on test data. The primary advantage of using deterministic methods is that such methods are simpler to implement and more suited for use in a bridge design office. A deterministic approach also causes all results to be reported at a standard confidence level. The use of random variables is advantageous in that the confidence level and probability of failure can be established by the bridge owner, since various agencies will have different levels of acceptable risk.

To implement a deterministic approach, the past, present, and future loading are needed to estimate the effects of such loading on the structure (i.e., the number and magnitude of stress cycles). Critical details and locations must also be identified for the fatigue evaluation. Given this information, the problem is relatively simple in that a damage model (typically one that is based on Miner's rule) may be used. In the literature, the steel of old steel railway bridges is often tested to determine the grade and chemistry of the metal and to determine if there are inclusions that may be detrimental to the fatigue behavior (Caglayan et al. 2009). A finite element model is then developed and often verified by load testing for the purpose of simulating

the effects of historical and future loading on the structure to arrive at a fatigue life estimate (Kim et al. 2001).

To implement a probabilistic approach, more information is needed than that required for a deterministic analysis. For each random variable, the type of distribution, the mean value, and the standard deviation must be determined (Ebrahimpour et al. 1992). Random variables may include the Miner's sum at failure, the dynamic amplification factor, traffic volume on the bridge, S-N curve characteristics, and modeling uncertainty (Imam et al. 2008). Due to the extensive information required for a probabilistic fatigue life estimate, applications of this method are found less frequently than deterministic ones.

2.1.2 Fracture Mechanics Based Methods

Although many codes use methods that implement S-N curves to estimate the remaining fatigue life of uncracked members, there is a fair amount of interest in using fracture mechanics for this purpose. The most attractive facet of fracture mechanics based methods is that they are adaptable to many types of details. Unfortunately, the information required to accurately predict the time to develop a crack and to determine the rate of crack growth is difficult to quantify (Connor and Fisher 2006). According to AASHTO (2010), cracked members must be evaluated using methods based on fracture mechanics rather than S-N curves.

In cases where it can be assumed that there is an initial flaw at a particular detail (e.g., at locations of welds or punched holes), the equation developed by Paris et al. (1961) can be used to predict the rate of crack growth as follows:

$$\frac{da}{dN} = C_c(\Delta K)^{m_c} \qquad \text{EQ 2.5}$$

where a is the crack length, N is the number of stress cycles, and C_c and m_c are material constants, often obtained from experimental results. The stress intensity factor, ΔK, is defined as follows:

$$\Delta K = F_e F_w F_s F_g f_r \sqrt{\pi a} \qquad \text{EQ 2.6}$$

where F_e is the crack shape correction factor, F_w is the width correction factor, F_s is the free surface correction factor, F_g is the stress gradient, and f_r is the applied stress range (MacDougall et al. 2006). The factors involved in computing the stress intensity factor are clearly problematic in evaluating a large structure, since the factors are difficult to accurately evaluate in practice. Under variable loading, the effective stress range is computed by Equation 2.2 which is the root mean cube of the stress history (MacDougall et al. 2006). To determine the remaining life of a detail (Paris et al. 1961), the differential equation is solved as follows:

$$N = \int_{a_0}^{a_c} \frac{da}{C_c * (\Delta K)^{m_c}} \qquad \text{EQ 2.7}$$

where a_o and a_c are the initial and critical crack lengths, which is determined as the crack length that makes the actual stress intensity factor equal to the critical stress intensity factor, K_{IC}. At this point the crack grows very quickly until failure occurs. The critical crack length is computed as:

$$a_c = \frac{{K_{IC}}^2}{\left(F_e F_w F_s F_g f_{max}\right)^2 \pi} \qquad \text{EQ 2.8}$$

where f_{max} corresponds to the highest stress experienced by the detail. All of the other terms are as defined above.

If it is assumed that there is no initial crack at a particular detail, the fracture mechanics method is performed in two parts. First, the time before crack initiation is determined. Then, the amount of time for the crack to reach a critical length is determined (Makkonen 2009). This is

the case when the initial cracks within a detail are removed by peening, which is striking of the surface of a metal in order to induce compressive residual stresses, or when the stress ranges are relatively small in magnitude and the initial cracks take longer to form (Connor and Fisher 2006). The crack initiation phase may exhaust a significant portion of the total fatigue life, between 40% and 90% of the duration (Makkonen 2009). The crack initiation phase is very difficult to predict, however, since the initial crack growth is irregular. Consequently, experimental values are invaluable in estimating the crack initiation period (Makkonen 2009).

In using a fracture mechanics approach, just as in S-N curves, there are various parameters that are probabilistic in nature. In the former approach, some of the required information is difficult or impossible to determine without extensive testing such as the initial size of cracks in a weld and the stress intensity factor (Cheung and Li 2003). Consequently, it is reasonable to use random variables to represent some of the values needed for the fatigue evaluation. Such variables include the C_c and m_c values in the Paris equation (see Equation 2.7). Other variables that can be represented using random variables include the initial and critical crack sizes, modeling uncertainties (i.e., differences between measured and simulated stresses), and the probability that a visible crack will not be detected during inspection (Righiniotis 2004).

Although fracture mechanics techniques may be a good tool for evaluating crack growth and estimating the remaining life of well-defined details, these methods were not used in this study since the goal of this research was to develop a method for estimating the remaining life of a civil structure in an efficient manner. Fracture mechanics methods require information that is difficult to quantify and that varies from detail to detail, such as the stress gradient and the crack shape.

2.2 Distortion Induced Fatigue

In some types of connections, fatigue cracks can be initiated due to out-of-plane distortions. This fatigue issue is somewhat prevalent in steel highway bridges built in the late 1960s and early 1970s, during which time the AASHTO design specifications discouraged welding transverse attachments to the girder flanges (Cousins et al. 1998). The problem typically exists when the flange of the girder is unable to rotate due to the rigidity of the deck above or due to the out-of-plane stiffness of the flange itself. These conditions can cause significant moments and forces to develop in the connection that is not attached to the flange. Many bridges were designed and constructed with a small gap between the top of the connecting stiffener (for the diaphragm or cross frame) and the girder flange resulting in a "web gap." This type of detail has been found to cause very high levels of stress fluctuation and deformation, leading to potential fatigue issues for these connections (see Figure 2.6). Furthermore, distortion-induced fatigue cracks are more difficult to predict than load-induced fatigue cracks because the deformations and stresses are more difficult to quantify (Roddis et al. 2003).

It has been found by various authors that the out-of-plane forces applied to the webs of steel girders cause significant distortion which, in turn, causes significant tensile stresses at the end of the fillet weld on the transverse member (Zhou 2006). Typically, smaller web gaps experience greater distortion-induced stresses than larger gaps since the distortion occurs over a relatively short distance (Zhou 2006). Oftentimes, a relatively simple change to the geometry of a detail, such as welding or bolting a stiffener to the girder flange, is enough to reduce or eliminate the potential for distortion-induced fatigue issues (Cousins et al. 1998). Sophisticated finite-element models of the connection detail in question have been used to evaluate various retrofit options (Roddis et al. 2003).

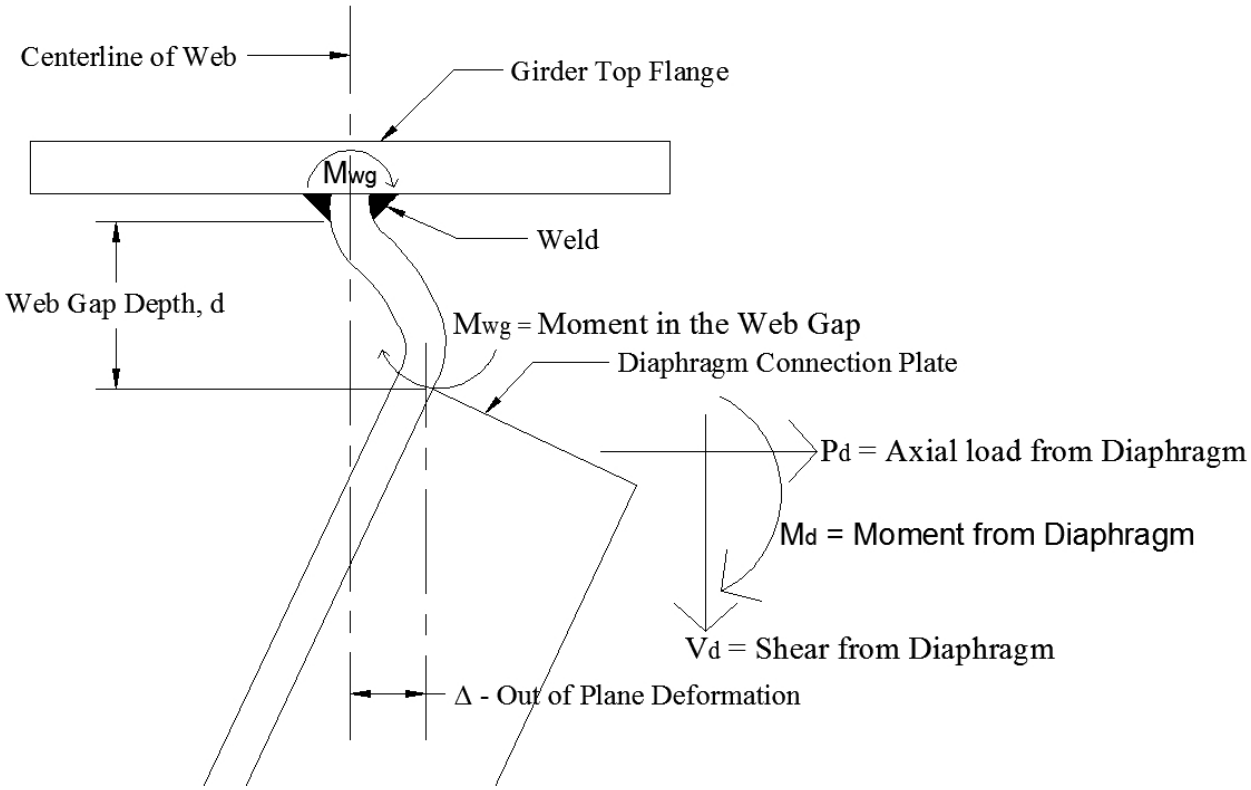

Figure 2.6: Illustration of "web gap" detail for steel bridges.

AASHTO (2010) mandates that transverse members must either be connected to both the top and bottom flange of the member or that the termination of the transverse member must be sufficiently distant from the nearest flange of the longitudinal member. This provision effectively eliminates connections that lead to distortion induced fatigue and therefore this type of fatigue is unlikely to be a problem in bridges built since 1985, when the AASHTO Specifications began including these provisions (Roddis et al. 2003).

2.3 Summary

Load-induced fatigue can lead to the failure of steel members that experience a large number of loading cycles. The remaining life of a particular detail can be estimated using fracture mechanics; however, this method requires a great deal of data specific to the detail. Distortion induced fatigue has been a problem on structures that contain details that induce large

out-of-plane stresses in the connections. This type of fatigue is typically handled by retrofitting the connections that are susceptible to this type of failure. Since distortion induced fatigue is a low-cycle phenomenon, the prediction of the remaining life of connections under distortion induced fatigue is not addressed in the AASHTO (2010) or AREMA (2007) specifications.

The standard method for estimating the fatigue life of highway and railroad bridges uses Miner's rule in conjunction with S-N curves that are based on the type of detail being studied. This method results in a reasonably accurate prediction of the remaining life of the structure and can be performed relatively simply, which makes it well suited for use in a bridge design office. Therefore, this is the method that was used in this study. Since bridges experience variable amplitude loading, the stress histories must be reduced to stress ranges, which were determined using rainflow counting in this study.

CHAPTER 3

Literature Review

3 Structural Health Monitoring

As the infrastructure around the world ages and approaches or exceeds its design lifespan, methods have been developed and studied to better determine the current condition and remaining life of these structures. Structural health monitoring (SHM) techniques are used to determine the condition or "health" of a structure based on nondestructive measurements. The most common type of SHM system found in the literature uses measured acceleration readings to determine mode shapes, damping, and/or natural frequencies. These dynamic properties are then compared against baseline measurements to detect the presence of damage. Some methods in the literature even attempt to determine the location and extent of damage. Alternatively, other SHM methods use measured strain readings to determine changes in the structure such as shifts in the neutral axis location and/or load distribution. Strain based systems have also been used to estimate the remaining fatigue life of a structure by determining the magnitude and frequency of stress cycles experienced by critical structural components. Various acceleration- and strain-based methods are discussed in the following sections.

Essentially all SHM systems require a measured or simulated baseline against which measured-response parameters can be compared for locating and quantifying damage. Many structures in need of evaluation are relatively old so it is virtually impossible to develop a baseline model that accurately depicts the pristine as-built structure since it is likely that the structure has changed over time. Some parameters that may influence the effectiveness of a dynamic-based SHM algorithm are changes to the boundary conditions, material properties,

connection fixity, dead load, live loads, etc. Consequently, the baseline model typically will represent the existing structure at the time the SHM system is deployed or it is developed based on the as-built plans. The complexity of the models can vary from simple two-dimensional models (Jerez 2007) to complex three-dimensional models with thousands of elements (Fei et al. 2007).

Model calibration is typically performed to ensure that the analytical behavior is consistent with that of the real structure. The complexity of the calibration may vary significantly from project to project. In general, parameters are either adjusted manually until the model matches the measured data reasonably well or complex algorithms may be used to iteratively adjust parameters within reasonable bounds until the analytical and experimental responses converge.

In the area of SHM, two approaches are available. Global SHM, as discussed thus far, uses a relatively low density of sensors to monitor for global changes in bridge response resulting from events such as fracture of a member or changes in temperature or boundary conditions experienced by the structure. "Hot spot" SHM involves heavy instrumentation of localized regions, such as the steel area near a rivet hole or termination of a weld, where fracture may be expected (Roach and Rackow 2007). This type of SHM utilizes non-destructive testing equipment such as comparative vacuum monitoring, piezoelectric transducers, or fiber optics to identify the existence of damage. To be effective, however, monitoring of numerous details that may potentially fail may be required (Roach and Rackow 2006; Roach 2009). For a bridge, the number of sensors may likely become prohibitive due to the large number of locations of potential failure (e.g., the riveted structure described in Chapter 4 contains over 7000 rivets, with hundreds in potentially fatigue-critical areas). Nevertheless, hot spot SHM is a valuable tool

particularly for monitoring known fractures, or for applications such as aircraft, where visual inspection and non-destructive testing can require significant disassembly and related downtime (Roach 2009; Roach and Pinsonnault, 2009). The remainder of this chapter will focus on global SHM techniques since the fatigue-life evaluation of steel bridges is the focus.

3.1 Sensors Available for Structural Health Monitoring

A variety of sensors are available for SHM purposes. Some have been in use for a relatively long time, such as electrical resistance strain gauges, and others are emerging, such as electromagnetic sensors that can directly measure the stress in a steel cable. Fiber optic sensors have caught the interest of researchers in SHM due to their insusceptibility to electromagnetic and radio frequency interference (Tennyson et al. 2001) and since they are moderately durable when embedded in concrete (Fuhr et al. 1999). Vibrating wire strain gauges have also been used for long-term, low-frequency measurements. It has been found, however, that most sensor types require periodic calibration, and many experience significant random drift even before the recommended calibration date has arrived (Farhey 2006). For dynamic testing of a structure, the accelerometer is the most common sensor.

There are three common types of sensors currently used to measure strain for highway and railroad bridges: 1.) strain transducers based on a Wheatstone bridge 2.) fiber optic sensors that relate strain to the change of a light source as it travels through the fiber, and 3.) vibrating wire strain gauges that relate strain to the measured frequency of a vibrating wire. Strain transducers are fairly common in bridge diagnostics and SHM for measuring strains in structural members; however, they are often used for relatively short-term measurements and zeroed between measurement sessions to eliminate the effects of temperature and random drift (Cardini and DeWolf 2009).

Fiber optic strain gauges have recently been implemented in some SHM systems. Advantages of fiber optic sensors include "good precision and accuracy over large ranges, immunity to electromagnetic interference, versatility of application, stability of material, and operability under extreme climatic conditions (temperature and moisture)" (Brownjohn 2007). One of the more widely used fiber optic sensors is the Fiber Bragg Grating (FBG) sensor, which can be multiplexed, meaning that multiple measurements from a single fiber can be made (Kister et al. 2007). It has been found, however, that fiber optic sensors can also have problems with random drift and must be periodically recalibrated (Farhey 2006).

Vibrating wire gauges (VWG) are composed of a taught wire held in place by two small steel bars. As the bars move away from each other under strain, the wire becomes more taught, and the frequency of vibration when disturbed by an electromagnet changes. Strain is determined based on the frequency at which the string vibrates. However, determining this frequency takes time and thus, readings cannot be taken as rapidly as with other sensor types. In the study by Farhey (2007), for example, VWG strain readings were only taken once per minute, whereas typical reading frequencies for other strain sensors are on the order of 100 Hz. When used on a steel structure, these sensors do not require temperature correction since they have nearly the same coefficient of thermal expansion; but they have been found to exhibit random drift as mentioned earlier (Farhey 2007).

Accelerometers are by far the most common sensor for measuring the dynamic characteristics of a structure. However, very little is mentioned in the literature concerning the long-term durability or susceptibility to temperature and drift of common accelerometers.

A few studies address the use of GPS for displacement monitoring. As of 2006, there are systems capable of providing 2 mm accuracy at a rate up to 20 Hz for real time measurements.

The systems include a base unit and rover units that are placed on the structure where displacements are desired (Li et al. 2006). When not measured in real time, the accuracy can be improved by comparing the data stored on each of the receivers and accounting for the errors (Li et al. 2006).

Vision-based methods have been developed to directly measure the displacements of a structure using a digital camcorder and a laptop computer loaded with image processing software. One example of such a system was developed by Lee et al. (2007). The camcorder recorded frames at 30 Hz, and the image processing software was used to determine the displacements in real time. A wireless network was used to synchronize measurements from multiple points to create mode shapes of the structure. The results using this system compared well with a laser vibrometer in field tests and LVDT sensors in the laboratory. The cost per channel was about $2000 in 2007 for the two channels used in the test, which is expected to decrease over time, but is still costly when compared to accelerometers and other strain measurement alternatives.

3.2 Methods using Acceleration Measurements

Acceleration-based methods of SHM are far more common than strain-based methods in the literature. In general, dynamic measurements and sophisticated algorithms are aimed at detecting reductions in structural stiffness, which is typically the definition of "damage" for an SHM system, and for some systems the location and magnitude of damage are also estimated. Much of the research in this area has focused on creating a system that can work in a real-world environment and compensate for signal noise, temperature fluctuations, and changes in boundary conditions.

The excitation source for an acceleration-based SHM system varies based on the data requirements for the algorithms being used. In general, there are three types of excitation sources: 1.) ambient vibration where the bridge is monitored under regular vehicular traffic and environmental loading while in-service 2.) forced vibration where traffic is halted and a known loading, such as the vibration from a "shaker" or instrumented hammer is applied at one or more known locations, and 3.) free vibration where the structure is released from a displaced shape, after which no additional force is applied while measurements are taken (Hsieh et al. 2006). Ambient vibration is often preferred for SHM of bridges since traffic is not disrupted and monitoring can be continuous. This excitation has limitations, however, since many algorithms used for structural identification require knowledge of both the loading and the response. In the SHM systems that utilize ambient vibration, either (1) specific sensors are used to estimate the traffic and wind loading, or (2) algorithms are chosen that do not require loading information. Systems based on forced vibration are less common than those using ambient vibration for SHM on bridges since the structure must be closed to traffic. However, forced vibration methods do have the advantage of requiring less sophisticated algorithms and sensor setups than those based on ambient vibration. Free vibration is not well suited for SHM systems since the bridge must be virtually free of external forces from traffic or weather during testing, and the structure must be released from a displaced shape, which is typically difficult and/or dangerous to accomplish. For this reason, very little was found in the literature concerning the use of free vibration for system identification and SHM of bridge structures. Nevertheless, the primary advantage of free vibration methods is that the analysis is easier relative to ambient and forced vibration methods.

3.2.1 Acceleration-Based Systems Using Ambient Vibration

The most favorable acceleration-based SHM system would use ambient vibration and be capable of detecting the existence, location, and severity of damage on a structure in real-time. Many researchers have pursued this goal; however, none were found that created and validated a system capable of reliably detecting damage with sufficient sensitivity and spatial resolution while being rugged enough to remain functional over an extended time frame. Systems using ambient vibration can be permanently installed on the structure of interest and monitoring can be scheduled, triggered or continuous. Alternatively, sensors can also be installed periodically to take discrete measurements. In the attempt to detect damage by tracking changes in the dynamic properties of a bridge, it is desirable to take readings continuously or at relatively short intervals (i.e., multiple times between visual inspections) so that when damage is present, action can be taken as soon as possible.

Under ambient vibration, numerous measurements are often taken along with the accelerations and/or displacements. These measurements include the wind direction, temperature, seismic activity, and traffic loads. For example, the Wind and Structural Health Monitoring System (WASHMS) developed by Li and Chan (2006) comprises 774 sensors including accelerometers, strain gauges, displacement transducers, level sensors, anemometers, temperature sensors, and weigh-in-motion sensors spread out over three bridges. More modest SHM systems use a much smaller array of sensors, such as the system implemented by Liu et al. (2008). This SHM system was deployed on an interstate highway in Connecticut and used 16 accelerometers, 6 tilt meters, and 14 temperature sensors. The number and type of sensors used is dictated by the budget of the project and the information required by the algorithm implemented. For example, more sensors are typically needed to determine the location and

extent of damage than when only the existence of damage is sought. Systems developed to use ambient vibrations tend to require more sensors due to the additional environmental information required.

Structural identification methods used with ambient vibration to obtain dynamic properties (i.e., mode shapes and natural frequencies) include the eigensystem realization algorithm (ERA), and the time domain decomposition (TDD) method. In the ERA method, the original data must be presented as free response data, which is accomplished by an impulse response synthesis (Jerez 2007) or by using the Natural Excitation Technique (NExT), which allows data obtained using ambient vibration to be represented as equivalent free responses (Caicedo et al. 2004). The ERA method is then performed by forming a Hankel matrix, which is a matrix that has constant skew diagonals, as illustrated in EQ 3.1

$$H(k-1) = \begin{pmatrix} Y(k) & Y(k+1) & \cdots & Y(k+p) \\ Y(k+1) & \ddots & & \\ \vdots & & & \vdots \\ Y(k+r) & \cdots & & Y(k+p+r) \end{pmatrix} \quad \text{EQ 3.1}$$

where p and r are the number of columns and rows, Y represents the i^{th} output due to the j^{th} input at time k. The Hankel matrix is then evaluated at $H(0)$ and EQ 3.2 is used to determine the matrices P, D, and Q which represent the left eigenvector *of H(0),* the diagonal matrix of singular values, and the right eigenvector of *H(0)*, respectively.

$$H(0) = PDQ^T \quad \text{EQ 3.2}$$

The rows and columns that can be attributed to noise can then be removed, and the reduced matrices can be used to determine the mode shapes and frequencies (Caicedo et al. 2004). Time domain decomposition can also be used to obtain the dynamic properties. This method involves

taking the raw data and applying a band pass filter to obtain the data that pertains to only one mode of vibration. Once the data for one mode is obtained, singular value decomposition is performed to obtain the modal parameters (Guan et al. 2006).

Once the structural identification is complete, a damage detection algorithm can be used to find the presence of damage and in some cases the location and/or severity of the damage. In the literature, various methods have been developed, including the modal assurance criterion (MAC), damage index methods, and methods that simply compare the calculated natural frequencies, modal displacements, and/or modal curvatures to those of a baseline model. Damage is typically defined as a loss of stiffness in these algorithms. For example, comparing the natural frequencies of a structure over time, a decreased frequency may indicate damage since a less stiff structure will vibrate at a lower rate (Reynders et al. 2007). Similarly, changes in the modal displacements and modal curvatures can be used to deduce the presence and location of damage (Reynders et al. 2007). The MAC is a method that gives a scalar value to describe how closely two mode shapes match. The MAC is defined as follows:

$$MAC(\varphi_a, \varphi_e) = \frac{|\varphi_a^T \varphi_e|^2}{(\varphi_a^T \varphi_a)(\varphi_e^T \varphi_e)} \quad \text{EQ 3.3}$$

where φ_a is the mode shape from an analytical model (or baseline measurements) of the pristine structure, and φ_e is the mode shape of the structure in its service condition at a later time (Reynders et al. 2007). A value of unity indicates perfect correlation between the two mode shapes, and lower values indicate a lesser agreement. Damage index methods, which can be defined as a difference (Guan et al. 2007) or a ratio (Wang et al. 2000) between a measured value and a baseline value, have also been used. The damage index developed by Wang et al. (2007) was defined as the ratio of the baseline and measured stiffness of the structure. The damage

index developed by Guan et al. (2007) was the difference between the measured and baseline mode shape curvatures.

One damage detection algorithm that was successfully employed in a SHM system to locate damage in a real structure is the Time Domain Decomposition (TDD) method. Using this method, damage in the form of a failing expansion joint was identified within one year of installing the SHM system and before the damage was observed in a visual inspection (Guan et al. 2007). The structure on which this system was installed was composed of carbon composite shells filled with lightweight concrete for the girders and a composite deck system. Accelerations were measured using 63 accelerometers that were installed permanently on the structure. Although the system was capable of detecting the damaged expansion joint, it was found that the dynamic properties may change as much or more from environmental effects than from the existence of damage (Guan et al. 2007). It should also be noted that the damage indicator itself gave no indication of the remaining service life or load carrying capacity of the structure.

3.2.2 Acceleration-Based Systems Using Forced Vibration

Although less common, forced vibration can be used in the attempt to detect and locate structural damage. The primary lure of forced vibration is the relative simplicity of analysis that comes with knowing the force inputs along with the measured response of the structure. Another advantage is that fewer sensors are required depending on the desired resolution since the test is performed when there are no significant environmental or traffic loads and therefore these parameters need not be measured. Much of the research using forced vibration has been performed on scale models in a laboratory setting (Caicedo and Dyke 2005, Owen 2003, Owen and Haritos 2003) with promising results. However, it cannot be assumed that similar results

could be achieved on a full-scale bridge in the field since environmental conditions have been found to affect dynamic properties and since the large mass of real structures make it difficult to adequately excite the various modes. Furthermore, the structure must be taken out of service during testing since traffic and environmental loads are difficult to quantify when using forced vibration techniques. Another potential issue is that forced vibration requires a large amount of energy to excite the vibrational modes of interest on a large structure.

Forced vibration on a full-sized bridge structure has been induced various ways including an instrumented hammer (Lynch et al. 2004), a specialized vibrating machine (Hsieh et al. 2006), or even a person jumping on the structure (Brownjohn et al. 2005). Excitation is often achieved with a specialized machine that spins an unbalanced weight and can be adjusted for loading amplitude and frequency. In many cases, excitation is induced at more than one location to excite various modes. Accelerometers are typically placed on a grid and no other instrumentation is required for environmental data since forced vibration testing is performed over a short period of time.

Structural identification techniques that are used with forced vibration include the ERA method and frequency response functions (FRF). Similar to using ambient vibration response data, the ERA method requires that the forced vibration response is processed using a technique such as NExT. Frequency response functions relate the frequency of the excitation to any of the various response parameters, such as the ratio of acceleration to force (accelerance) or the ratio of force to displacement (dynamic stiffness) (Irvine 2000). These frequency response functions can be determined by varying the frequency of a vibrating machine, and measuring the response of the structure, from which the natural frequencies can be determined by finding peaks in the plot.

Once the structural identification has been performed, a damage detection algorithm can be implemented. Since the damage detection algorithms typically quantify changes in dynamic properties, many of the algorithms used for ambient vibration can also be used for forced vibration such as the modal assurance criterion (Brownjohn et al. 2005). One method that is exclusive to forced vibration is the global flexibility index (GFI) which tracks the changes in the flexibility of the structure. This method requires calculating a frequency response function by using a fast Fourier transform of the time domain equations of motion, from which the flexibility matrix can be established as follows:

$$[F] = [\Phi]\left[\frac{1}{\omega^2}\right][\Phi]^T \qquad \text{EQ 3.4}$$

where $[F]$ is the modal flexibility matrix, $[\Phi]$ is the mass normalized modal vectors, and $\left[\frac{1}{\omega^2}\right]$ is a diagonal matrix containing the reciprocal of the square of natural frequencies from largest to smallest (Patjawit and Kanok-Nukulchai 2005). The global flexibility matrix can then be used to determine the global flexibility index as follows:

$$[GFI] = \sqrt{\lambda_{max}(F^T F)} \qquad \text{EQ 3.5}$$

where $\lambda_{max}(F^T F)$ is the largest eigenvalue of the $F^T F$ matrix. This method was found to be effective in a laboratory setting; however, no tests were performed in the field (Patjawit and Kanok-Nukullchai 2005).

3.2.3 Strengths and Weaknesses of Acceleration-Based SHM Systems

In theory, SHM methods using acceleration measurements have potential for locating and quantifying damage since damage often presents itself as a reduction in stiffness, and this can be determined using acceleration data. In practice, however, it has been observed that the change in

stiffness due to damage is often too small to consistently be detected under actual field conditions. Several damage detection methods have been successful but mainly in a laboratory setting (Jerez 2007; Caicedo and Dyke 2005; Owen 2003; Owen and Haritos 2003; Patjawit and Kanok-Nukulchai 2005; Wang et al. 1998). The primary advantage of dynamic SHM systems is that ambient vibrations may be used, which allows for continuous real-time monitoring without interrupting traffic. Other advantages include the ability to quickly assess the global condition of the structure and of the boundary conditions.

There are, however, significant drawbacks to using acceleration measurements for SHM applications. For the most part, the systems described in the literature were unable to detect critical damage in a structure that could be overlooked during a standard visual inspection. One major reason for this shortcoming is that the available SHM methods are focused primarily on global behavior and as a result, are not well suited for finding local damage. Also, SHM systems that evaluated temperature effects showed that the dynamic properties may change significantly more due to temperature fluctuations than from structural damage. For example, the Xupu cable-stayed bridge in Shanghai, China showed natural frequency changes of merely 1% due to modeled damage, while the daily fluctuation in natural frequency was of the same magnitude (Zhang and Zhou 2007). In addition to temperature issues, errors are introduced from the sensors and from signal noise, making it difficult to identify the subtle changes in the structure due to damage (Zhang and Zhou 2007).

Other drawbacks of acceleration-based SHM systems are that data processing requires significant computational capacity and sophisticated algorithms due to the large volume of data collected. This is particularly true for large structures that are heavily instrumented such as the bridges that are part of the Weather and Structural Health Monitoring System (WASHMS) in

Japan. For just one bridge, data from approximately 300 sensors are continuously measured and processed in real time (Ni et al. 2008). A significant number of these sensors are used to measure the environmental loading from wind, temperature, and seismic activity since this information is needed to accurately account for changes in behavior due to changing environmental conditions. The large quantity of data also makes it difficult to transfer the information from on-site to those responsible for reviewing the information. Such systems can gather more information than what can be streamed via common communication methods, particularly if a wireless system is implemented. The large volume of data also creates a need for an easily understood presentation of the data (Brownjohn 2007). To be practical, a SHM system should be installed for operation by existing bridge maintenance crews and engineers, who most likely will not be familiar with the dynamic-based SHM algorithms.

3.3 Methods Using Strain Measurements

Although less popular in the literature than acceleration-based SHM, systems based on strain measurements have also been developed. Some of these systems require less complicated processing since they are not set up to continuously monitor the bridge behavior. Systems that are used for fatigue life prediction of the structure require periodic (rather than continuous) measurements, thus reducing the per-structure monitoring cost. Since a bridge is monitored over a relatively short time period, portable strain-based SHM systems can be used on multiple bridges, which reduces the cost of instrumentation and data acquisition. Also, sensor drift due to temperature or random drift is not as significant as with continuous monitoring since the sensors are in place for a relatively short period of time. Generally speaking, SHM systems that use strain and/or deflection measurements are based on concepts that are more familiar to the practicing bridge engineer than the acceleration-based methods discussed previously.

There are three basic types of systems found in the literature that use strain measurements for the purpose of SHM of bridge superstructures. The first type uses strain measurements taken under regular traffic for a limited period of time. Based on an estimate of the accumulated historical fatigue damage, the measured response can then be used to predict the remaining fatigue life of the structure. The second type of SHM system is one that uses measured girder strains to compute structural properties such as the load distribution factors and/or neutral axis locations which can be compared to baseline values to evaluate the performance of the superstructure. The third type is one that takes infrequent strain readings (e.g. once per hour), and performs signal processing to identify relatively sudden (as opposed to seasonal) changes in the structural behavior that indicate damage.

3.3.1 Strain Methods for Estimating Remaining Fatigue Life

The remaining fatigue life of a structure can be approximated using the methods discussed in Chapter 2 where the historical loading is estimated and the current and future traffic can be measured. Data must be collected over a sufficiently long time period to be considered representative. A week long period is typically sufficient for a highway bridge since different days of the week may have different traffic characteristics (Post et al. 1988). For a railroad bridge, fewer days of monitoring may be required since the schedule of trains is known. Methods that utilize Miner's rule and rainflow counting are far more popular when monitoring civil infrastructure than fracture mechanics methods due to the relative ease of implementation.

One example of a system that utilized the effective stress range is the Tsing Ma Bridge in Hong Kong. The steel orthotropic deck was instrumented with 110 strain gauges at three critical locations identified during the design phase of the structure (Li et al. 2003). These sensors were used to continuously measure strains, thus producing a very large volume of data. In this study,

strain histories were taken from 6 different days and various statistical analyses were performed to determine which could most accurately represent the actual strain histories. It was found that the method of multiple linear regressions in the frequency domain was best suited to obtain a representative loading block. This method involved taking a strain history and using the Fast Fourier Transform (FFT) to represent the data in the frequency domain. The equation for multiple linear regressions can then be applied as follows:

$$y^* = b_o + b_1 x_1 + b_2 x_2 + \cdots + b_n x_n \qquad \text{EQ 3.6}$$

where y^* is the estimated set of objective variable y; b_o is a constant and b_1, b_2,…, b_n are partial regression coefficients corresponding to each set of independent variables, x_1, x_2,./.., x_n, respectively (Li et al. 2003). After this regression equation is applied, the frequency data can be transformed back into the time domain using the Inverse Fast Fourier Transform (IFFT). It was found that the data that resulted from the statistical analysis matched the actual strain history well, as determined using a parameter called the mean of absolute percentage error which is the sum of the error at each point between the original and predicted strain divided by the number of points. Using this method a "loading block" that represents the stress history at a particular location over a known period of time (e.g., one week) can be determined. The block is assumed to be representative of traffic for each following time period (i.e., traffic will be the same each week) and will repeat itself without change until a new "loading block" is obtained. This method can be used in a fatigue life evaluation to determine the accumulation of fatigue damage under actual traffic (Li et al. 2003). In this paper, the fatigue life was ultimately determined for various probabilities of failure. To adjust the estimated life, the S-N curve was adjusted based on the probability of failure. The Nanjing Yangtze River Bridge in China was studied in a similar way (He et al. 2006). On this structure, 50 strain gauges were installed on various truss members to

obtain measured strains, which were then used in a fatigue evaluation based on Miner's rule and rainflow counting. In this study, the Miner's sum was calculated for a certain time period. The remaining life of the structure could then be calculated assuming that traffic would remain constant in the future or by assuming some annual rate of traffic growth.

A much more modest system that uses measured strains for fatigue life estimation but with far fewer gauges was developed by Howell and Shenton (2006). This portable system used only two sensors and could be quickly and easily installed on a bridge for a relatively short time period, then removed and moved to another bridge. This system is capable of processing strains using a rainflow counting algorithm, storing peak strains, and recording stress histories of passing trucks. Since the raw data is processed using the rainflow algorithm and the result is a histogram of stress ranges, the volume of data is small. Power consumption is relatively low since readings are only taken when triggered by a truck causing a strain greater than a pre-defined threshold. Data may be transmitted via a wireless device that communicates over a cellular network. This allows it to be used anywhere within range of a cellular network tower. The data can be used to update fatigue life evaluations.

One unique aspect of methods that use strain measurements to improve a fatigue model of a structure is that the remaining life can be estimated whereas all other methods, whether they use acceleration or strain data, attempt to identify damage in the structure after it occurs. This prognostic approach is very attractive in the area of bridge management since agencies must work within a budget, and therefore do not want to replace a structure (or structural members) before it is necessary. If the remaining life of the bridge can be estimated based on the fatigue evaluation, the bridge owner can plan for repairs, retrofits, or replacements using this knowledge coupled with the results of visual inspections and load rating calculations. If all of this

information for all of the steel structures owned by an agency is placed in a database, repairs, retrofits, and replacements of structures can be prioritized rationally, thus saving money and reducing the probability that structures will experience fatigue failure.

3.3.2 Strain Methods that Detect Damage based on Structural Properties

Another approach for SHM using strain measurements focuses on continuous monitoring of multi-girder structures to track changes in the load distribution and/or section properties. It is preferred that at least one controlled load test be performed to create and validate a finite-element model. The model can then be used to simulate damage scenarios (e.g., loss of stiffness in the deck or a crack in a member) for comparison with actual measurements for the purpose of damage detection. Alternatively, strains can be measured over a representative time period and a statistical analysis of measured structural properties can be performed to identify outliers (Cardini and DeWolf 2009). In addition to continuously tracking changes in the load distribution factors and/or neutral axis depths, the remaining fatigue life of the structure can also be predicted using the gathered strain data.

A strain-based SHM system was developed by Cardini and DeWolf (2009) to track changes in the peak strain, neutral axis location, and load distribution factors of the main girders of an interstate bridge in Connecticut. Strain gauges were placed near the top and bottom of the web of the 8 girders midway across the end span, and 4 gauges were placed in the adjacent interior span (near the bottom of selected girders) at the mid-span and first quarter point to determine the speed of passing trucks. This system was designed to record data only when triggered by a sufficiently heavy vehicle in order to reduce data volume, reduce power consumption, and eliminate the effect of sensor drift and temperature effects since the sensors are periodically reset to zero strain (Cardini and DeWolf 2009). To determine acceptable ranges

for the distribution factors, measurements are first taken under normal traffic and analyzed. Upper and lower bounds on the load distribution factors were then established based on a pre-determined number of standard deviations from a Gaussian distribution for each girder (Cardini and DeWolf 2009). Outliers in the measured data, which may indicate damage, can then be identified.

Another system that uses measured strains was implemented to evaluate the Pioneer Bridge in western Singapore. This bridge was retrofitted by modification of the support conditions such that the simple supports were made integral with the abutments (Moyo et al. 2004). To determine the effectiveness of this retrofit, the structure was instrumented with strain gauges to identify the peak strains under traffic. The Method of Independent Storms (MIS), which is a method that can be used to estimate the return period of independent maximum strain values, was used on the peak strain data to determine the probability that an overweight (potentially damaging) vehicle would cross the bridge over a given time period (Moyo et al. 2004).

3.3.3 Strain Methods that Detects Damage using Signal Processing

The third type of strain-based SHM system uses measured strain and pressure measurements (from embedded vibrating wire strain gauges and pressure cells) to detect damage. In the study by Omenzetter et al. (2004), hourly measurements of strain and internal pressure (i.e. stresses) were taken during and after construction of the Singapore-Malaysia Second Link Bridge, which was built using the balanced cantilever method over a two month period. The data was subsequently analyzed using wavelet transforms to identify sudden changes in the strain history. According to the authors, sudden changes in the behavior of the structure can easily be overlooked when manually reviewing strain histories, and therefore an automated approach to

seeking sudden changes is important in detecting damage (Omenzetter et al. 2004). The data processing involved determining the wavelet coefficients, then performing a statistical analysis to locate outliers in the data. Outliers in the data indicate a sudden change in the system and therefore may represent damage, unusual traffic, or a weather related event. Once the outliers are located, each one can be investigated to determine the cause. It was found that the method used was able to accurately identify the time at which additional segments were added to the bridge. It was also noted, however, that this method is not an ideal SHM system since only the presence of an unusual event can be determined. The cause of the anomaly must be determined separately, which may restrict this method from being adopted in its current form (Omenzetter et al. 2004).

3.3.4 Strengths and Weaknesses of Strain-Based SHM Methods

There are a number of advantages of using strain-based SHM methods as opposed to acceleration-based methods. First, strain-based SHM methods that track changes in structural properties and those that involve fatigue life estimates rely on concepts that are familiar to a practicing civil engineer. This is advantageous because such methods would ideally be implemented by an agency that owns civil structures such as state departments of transportation and railroad owners. Second, the amount of instrumentation can be reduced since the engineers at the agency are able to determine efficient sensor layouts using knowledge of fundamental principles (e.g., maximum moments occurs at approximately mid-span for simply supported members). Third, the reduction in instrumentation leads to a reduction in the amount of data collected. Also, less hardware is required which makes these systems less expensive to implement. The fourth advantage is that a SHM system can be developed that only requires periodic strain measurements, allowing the same system to be used on multiple structures. This

further reduces the instrumentation and data acquisition needs for an agency (i.e., a fleet strategy). Fifth, loading conditions are much simpler to accommodate for using strain-based SHM systems than systems that require forced or free vibration. The sixth, and perhaps one of the greatest strengths of the systems that utilize fatigue models to predict the remaining life of structural components, is that a failure prediction can be made instead of being detected after the fact. This allows for a prognostic approach to maintenance and repair as opposed to the time-based methods that are often implemented. This approach can be much more efficient since structures are not replaced before it is required simply because of age.

Strain-based methods do have some limitations, however. One such limitation is that these methods are generally unable to quantify damage. The systems found in the literature do not attempted to pinpoint the location or severity of damage; instead, critical locations are usually pre-determined before the system is implemented so that potential damage can be evaluated. Another disadvantage of systems using fatigue evaluation is that the live loading of the past must be estimated and therefore the fatigue analysis is only as reliable as the quality of historical information that is put into the model. Another weakness of strain measurements, as with acceleration measurements, is that changes in temperature can cause fluctuations in the data that must be accounted for in the analysis. The sensors used for strain measurements can also be problematic, particularly if continuous monitoring is required since strain transducers have a tendency to experience significant random and temperature drift. This must be removed from the data to make it useable. Finally, the critical locations must be accurately identified for these systems to work since monitoring only occurs at a limited number of locations.

3.4 Challenges of Long-Term Continuous Monitoring

In practice, multiple difficulties have been encountered in developing SHM systems that are suitable to continuously take readings under variable traffic and environmental conditions. When monitoring is continuous, variations in temperature may cause changes in the measured mode shapes, natural frequencies, and strains of a structure (Brownjohn 2007). Another significant problem is the tendency of gauges placed on a structure to experience random drift, which over time, can make the readings from a sensor useless (Farhey 2005). Data storage and processing becomes an issue for large structures in cases where many sensors are read on a continuous basis and/or readings are taken at a high frequency. The per-structure cost of an SHM system is much higher when the system is designed to remain permanently installed on a given structure for the life of the system as opposed to temporary installations on multiple structures for periodic monitoring. Another challenge is that, in order to most accurately detect damage or predict fatigue failure, the structure should ideally be monitored at the beginning of its service life to create a true baseline. This is problematic because today's array of aging civil structures was not monitored to create such a baseline. It is also problematic because no system has shown the ability to continuously monitor a structure's behavior for the length of time that is typically expected for a civil structure to be in service, which may be 100 years or more.

One issue that requires significant attention in the design of a SHM system for use on a structure exposed to variable environmental conditions is the effect of temperature on the behavior of the structure. This issue has been addressed in various ways by numerous authors. One approach to eliminate the temperature effect is to develop a relationship between temperature and the parameter being determined. An example of such an approach was presented by Liu et al. (2008), who developed linear relationships between temperature and the

first three natural frequencies of the bridge being studied. Another method to account for temperature is to analyze the data over a prolonged period of time (i.e., years) and determine the fluctuation in the behavior over time. These diurnal fluctuations can then be removed by subtracting the temperature effects from the future data (Catbas et al. 2008). Another way to avoid problems with temperature change is to set the gauges to zero before measurements are taken. With this approach, both the temperature and drift effects are removed from the data. This method requires knowledge of when the bridge will be unloaded and of when vehicles of interest are approaching the structure, which can be accomplished by the trigger system described by Cardini and DeWolf (2009).

Still another challenge in long-term SHM is sensor drift, which was discussed earlier in greater detail (see Section 3.1). Various authors have found that the sensors used for SHM systems installed on bridge structures have a tendency to experience random drift. In one study, the sensor drift rendered the readings from Fiber Optic Bragg Grating (FBG) sensors and vibrating wire strain gauges unusable before the recalibration date approached (Farhey 2006). Problems with sensor drift are difficult to account for since they are random in nature and are different from one sensor to another. This problem can be addressed by installing "witness sensors" which are not rigidly attached to the structure, but instead take readings that represent only the effect of temperature and random drift on the gauge itself. For strain readings taken continuously without periodic zeroing, drift can be accounted for by determining when the structure is unloaded and manually adjusting the data to compensate. However, this method may eliminate the effects of temperature on the structure which may be significant as shown by Guo et al. (2008).

Data storage and processing can be a significant hurdle for large-scale SHM systems since suitable hardware can be expensive. The volume of data is also an important consideration when data needs to be transmitted. If the data cannot be transmitted faster than it is being collected, it must be processed on-site, which requires on-site hardware and perhaps a climate controlled enclosure for protection against environmental elements. This problem can be minimized by logging measurements only when triggered by a sufficiently significant event, as shown in Howell and Shenton (2006).

One challenge that is universal to all SHM systems is the fact that a baseline model and/or traffic patterns from the time of construction are needed to most accurately detect damage or predict the remaining life. For damage detection algorithms, a baseline model is important because there must be a pristine condition state against which current measurements can be compared. If measurements were not taken at the beginning of the structure's service life, the structure in its current condition can be taken as the baseline, or a finite-element model can be developed based on the as-built construction plans. If a structure is first monitored late in its life, it is probable that some changes have already occurred before the system was put in place. For fatigue-based SHM systems, a representative strain history is necessary to obtain an accurate remaining life since all stress cycles above a certain level are damaging. To address the need for historical traffic loading, traffic loading can be estimated based on past traffic studies. If no prior data is available, a current loading block can be obtained, and a historical rate of traffic growth can be assumed. Once the current traffic and a rate of growth are determined, the historic traffic can be estimated by adjusting the current traffic data through a reduction in the weight and/or frequency of trucks crossing the bridge.

3.5 Summary

Many systems have been developed with the purpose of either identifying or predicting structural damage through *in-situ* measurements. Methods that implement dynamic measurements typically use measured accelerations to periodically obtain natural frequencies and mode shapes. These dynamic properties are then compared over time either directly (e.g., observing changes in the natural frequency of the first few modes) or by using an algorithm that extracts information from the measured data that may be indicative of reduced stiffness (e.g., mode shape curvature). These methods have been thoroughly studied in an attempt to find a method that accurately and consistently detects structural damage. However these systems are typically only able to describe global rather than local behavior, and therefore are not well suited to detecting small but significant flaws such as cracks. These systems also require a high density of instrumentation to be most effective.

Methods that use strain to detect damage are also available, although there are far fewer studies in the literature than for methods using dynamic measurements. These systems can detect changes in structural properties, such as the neutral axis location or live load distribution factors. These methods can be effective and are based on principles that are well understood by a typical bridge engineer. However, significant damage must occur before these systems can identify damage and the structure must be instrumented at all cross sections of the bridge that are most susceptible to failure.

Methods that use measured strains to update a fatigue model are very attractive for the management of bridges. Using this method, the remaining life of structural components can be estimated, thus allowing for a prognostic approach for the replacement of structural members versus the actual real-time detection of structural damage. These methods usually require

relatively light instrumentation once a structural model is established. Another disadvantage is that instrumentation can be installed periodically to update the traffic model as opposed to being left in place for the life of the structure. Assuming that historical data can be estimated, a reasonable remaining life for the structure can be calculated and used in a bridge management program to prioritize maintenance and replacement activities. For these reasons, this method is the focus of this study. Difficulties with this method include accurately determining historical loading and finding the most critical members and connections. Historical traffic may be estimated using data from the bridge owner such as the gross weight per year carried by the line or historic train schedules. Critical details can be determined by carefully examining the types of details that contain significant stress risers, particularly in areas of high nominal stresses.

CHAPTER 4

Bridge Description and Diagnostic Load Testing

The state of New Mexico's purchase of the railroad track between Belen and Lamy, NM to carry the New Mexico Rail Runner requires the state to inspect and evaluate all the bridges on the line according to federal guidelines. Since many of these bridges are steel structures that are over 100 years old and due to the large number of trains that have crossed these structures, there is reason to suspect that there may be fatigue issues. Another reason to suspect fatigue is a concern is that the first fatigue provisions entered the AREMA Specifications in 1910 (AREMA 2007) after some of these structures were designed, including the structure being studied in this paper. The structure evaluated in this study is on the portion of the railroad that carries Rail Runner and Amtrak passenger rail between Albuquerque and Santa Fe, NM.

4.1 Bridge Description

The bridge investigated for this SHM investigation is at mile post (MP) 880.37 near Algodones, NM which carries the railway over the Angostura Arroyo as shown in Figure 4.1.

Figure 4.1: Photograph of Rail Bridge at MP 880.37 (Algodones, NM).

This structure is a ballast-deck, steel through-girder bridge that was built in 1898. Ballasted decks have a timber, steel plate, or concrete slab deck that supports crushed stone, which in turn

supports the ties and rails on which the trains travel. Through-girder structures consist of two deep plate girders on either side of the railway; floorbeams are placed transversely and support smaller longitudinal members called stringers, which in turn carry the deck. Currently, this bridge only carries Rail Runner and Amtrak trains, but historically freight trains and other passenger trains crossed this structure on a regular basis.

4.1.1 Rails, Ties, and Ballast

The ballast depth of Bridge 880.37 is approximately 10 in. (25.4 cm) from the top of the timber deck to the bottom of the ties based on measurements taken during the last inspection in March of 2011. The ballast consists of crushed stone. The treated timber ties are spaced 19.5 in. (49.5 cm) center-to-center and are 6.5 in. (16.5 cm) high, 8.5 in. (21.6 cm) wide, and 8.5 ft. (2.59 m) long. The rails are spaced at 4.71 ft. (1.44 m) from inside to inside (i.e., gauge distance) and weigh 136 lb/yd (67.5 kg/m) with the dimensions shown in Figure 4.2. The steel of the superstructure and rails is assumed to have an elastic modulus of 29,000 ksi (200 GPa), a yield stress of 30 ksi (206.8 MPa), and an ultimate stress of 60 ksi (413.7 MPa) (AREMA 2007).

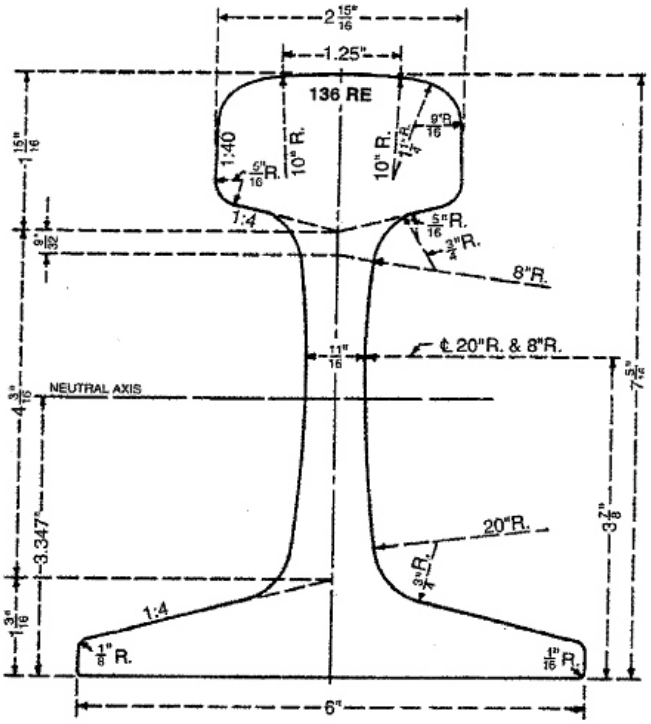

1. Rail Area (square inch)	
Head	4.8187
Web	3.6375
Base	4.8702
Whole Rail	13.3263
2. Rail Weight (lb/yd) (based on specific gravity of rail steel = 7.84)	135.8826
3. Moment of Inertia about the neutral axis (in^4)	94.20
4. Section modulus of the head (in^3)	23.70
Section modulus of the base	28.20
5. Height of neutral axis above base (in.)	3.34
6. Lateral moment of inertia (in.)	14.44
7. Lateral section modulus of the head (in^3)	9.83
Lateral section modulus of the base	4.82
8. Height of shear center above base (in.)	1.64
9. Torsional rigidity is 'KG' where G is the modulus of rigidity and K = (error for K greater than 10%) (psi)	6.24

Figure 4.2: Rail dimensions and section properties (AREMA 2007).

4.1.2 Floor System

The floor system of Bridge 880.37 consists of two riveted plate girders that are built-up using a 99.75 in. x 3/8 in. (2.53 m x 0.953 cm) web plate and two 6 in. x 6 in. x 7/8 in. (15.2 cm x 15.2 cm x 2.22 cm) structural L shapes for the top and bottom flanges. Cover plates that are 16 in. x 5/8 in. (40.6 cm x 1.59 cm) are also used as the maximum moment in the girder increases.

At mid-span a total of 4 cover plates are used on both the top and bottom flanges (see Figure 4.3 and Table 4.1). The floorbeams are also built-up steel members that consist of a 24 in. x 9/16 in. (61.0 cm x 1.43 cm) web plate and 6 in. x 6 in. x 13/16 in. (15.2 cm x 15.2 cm x 2.06 cm) double angles. Near the ends of the floorbeams, knee braces are provided by extending the web plate up towards the top of the girder (see Figure 4.4).

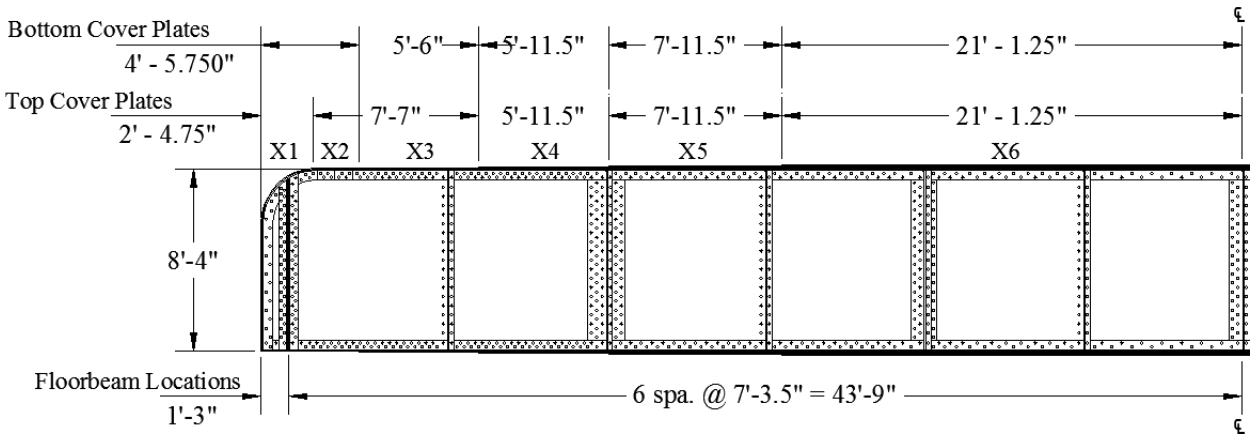

Figure 4.3: Girder profile of Bridge 880.37.

Table 4.1: Description of girders sections X1 through X6 for Bridge 880.37.

Section	Total Thickness of Top Cover Plates (in.)	Total Thickness of Bottom Cover Plates (in.)
X1	0.375	0.000
X2	0.625	0.000
X3	0.625	0.625
X4	1.250	1.250
X5	1.875	1.875
X6	2.500	2.500

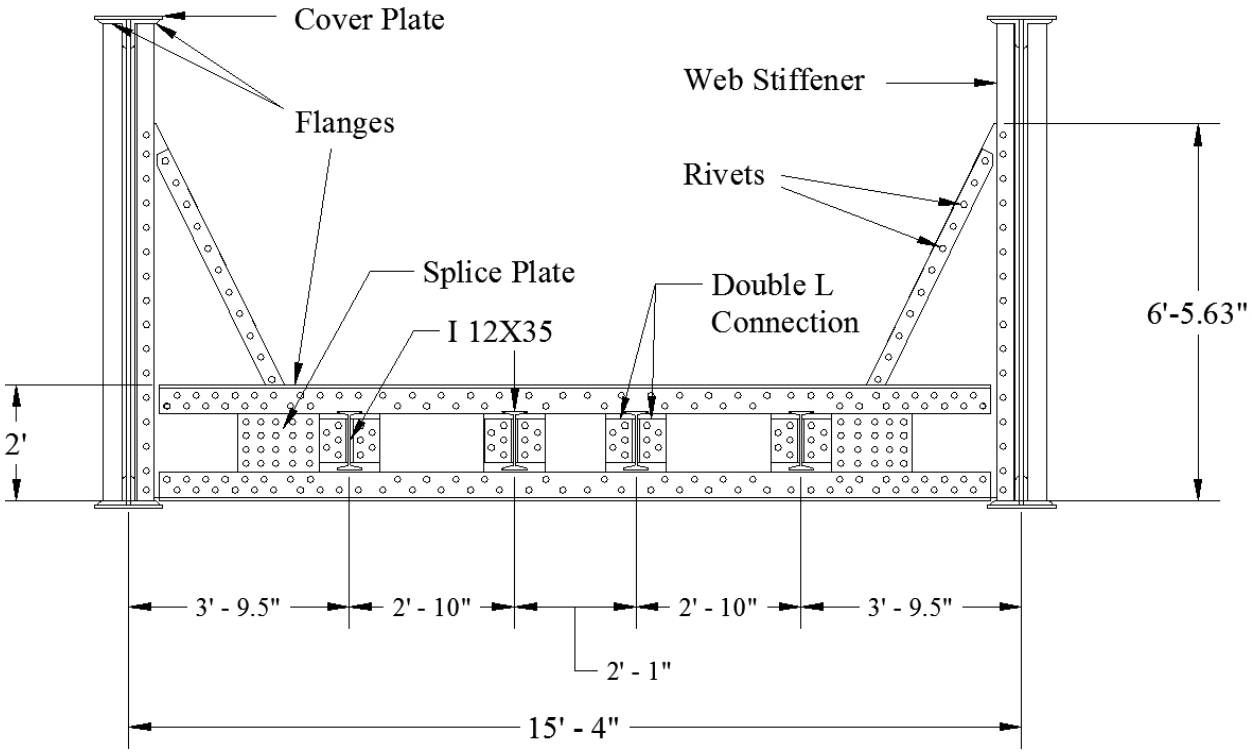

Figure 4.4: Floorbeam profile of Bridge 880.37 (deck removed for clarity).

The stringers are rolled steel I 12X35 shapes that are rivet connected to the floorbeams using 6 in. x 6 in. x ½ in. (15.2 cm x 15.2 cm x 1.27 cm) double angles (see Figure 4.4). The girders are spaced transversely 15.33 ft. (4.67 m) center-to-center, the floorbeams are spaced 7.29 ft. (2.22 m) in the longitudinal direction, and the stringers are spaced transversely 2.83 ft. (86.4 cm) from the exterior stringer to the interior stringer and 2.08 ft. (63.5 cm) between interior stringers (see Figure 4.5). All connections for this structure are made using rivets with a shank diameter of 7/8 in. (2.22 cm).

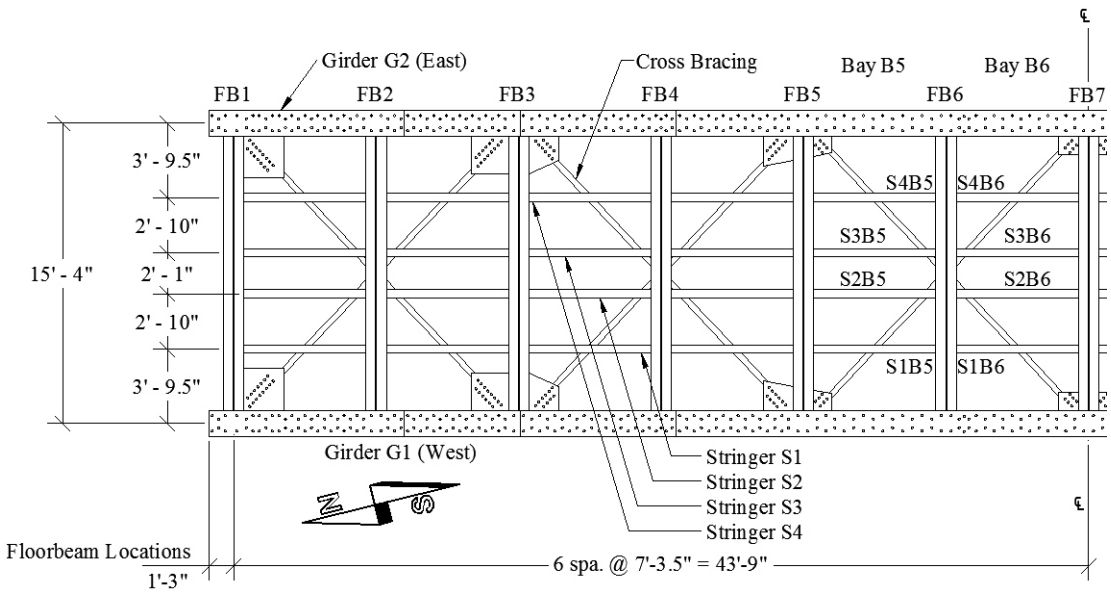

Figure 4.5: Framing plan for Bridge 880.37.

The deck between the floorbeams consists of 6 in. x 8 in. x 14 ft. (14.0 cm x 19.1 cm x 4.27 m) treated timbers placed perpendicular to the stringers and resting directly on the top flanges as shown in Figure 4.6. All cross sectional dimensions provided for timber members are nominal, which is ½ in. (1.27 cm) larger in both dimensions than the actual size. Over the floorbeams, ½ in. (1.27 cm) thick steel apron plates bridge over the flange of the floorbeams so that all loads are distributed to the floorbeams via the stringers. Timber ballast curbs are placed along the edges of the deck to ensure that the ballast remains in place. At the floorbeam locations, the web plate that extends upwards necessitates a special detail of the curb timbers that go around the web plate as shown in Figures 4.6 and 4.7.

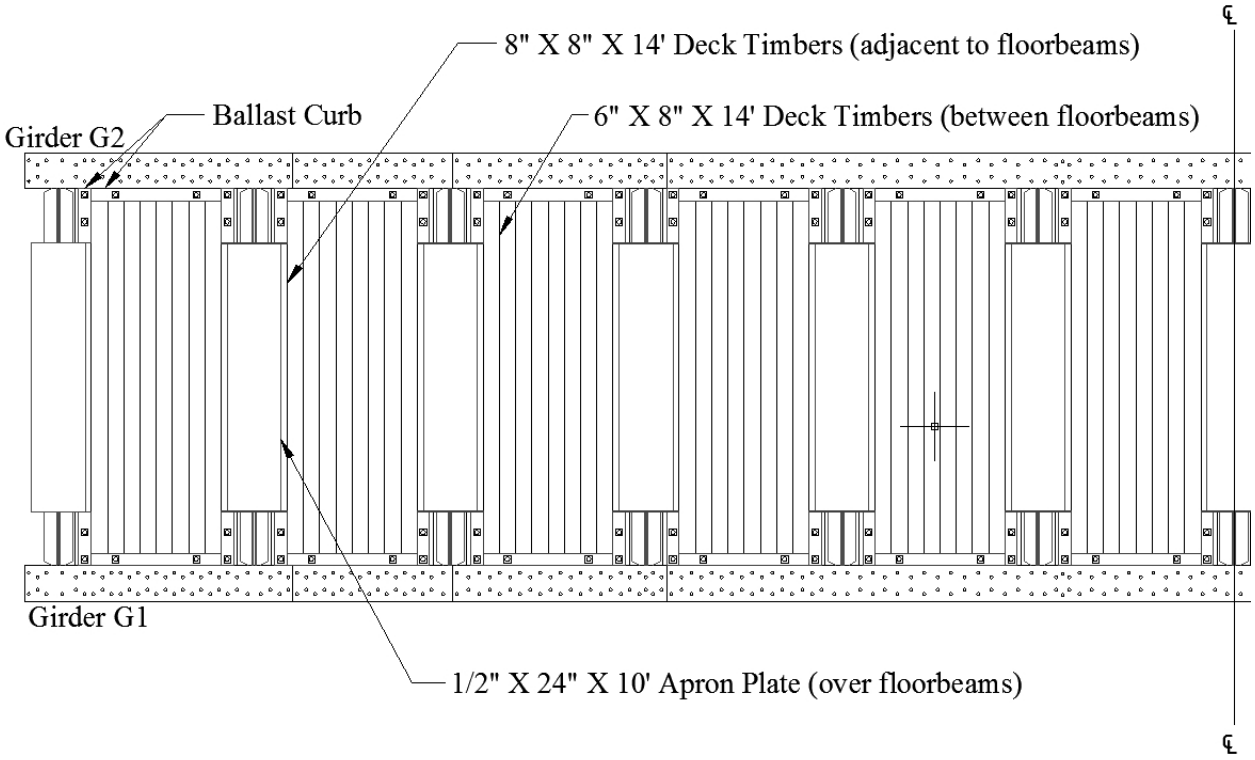

Figure 4.6: Deck plan for Bridge 880.37.

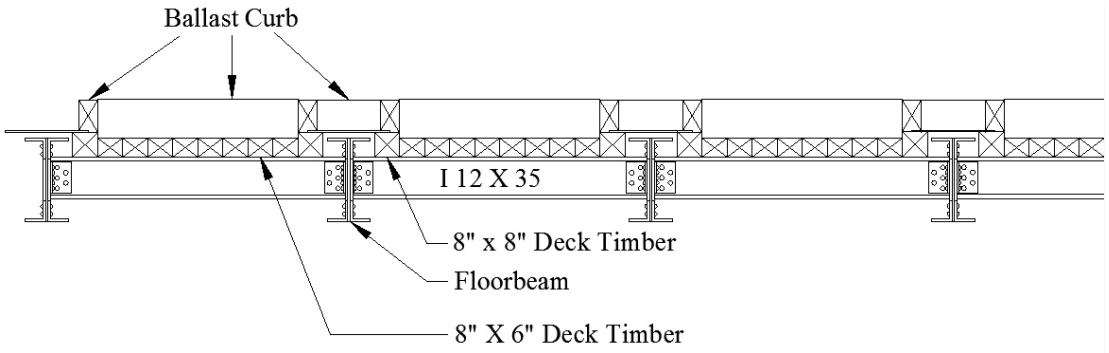

Figure 4.7: Stringer profile for Bridge 880.37.

4.1.3 Inspection Report

The inspections of the bridges on the newly acquired line were performed by Wilson & Company, Inc., the contractor to the state for inspecting and load rating each structure. During bridge inspections, the structure is visually inspected for flaws or any signs of deterioration. Once all potential problems have been documented, the deck, superstructure, substructure,

channel, and channel protection are all given a condition rating. The condition rating given to the deck, superstructure, and substructure components takes a value that ranges from 0 (failed) to 9 (excellent). A condition rating of 4 or lower indicates that the bridge may have lost structural capacity and requires special consideration when evaluating the load carrying capacity.

The most recent inspection for Bridge 880.37 took place on March 26, 2011. This structure is on a 12-month inspection schedule. The 2011 inspection found that the superstructure is in generally good condition and was given a condition rating of 6 due to some small areas of pack rust between cover plates on the girders and on the gusset plates attaching the cross bracing to the girders. The substructure was given a condition rating of 5, which is considered fair. Some cracks, spalling, and efflorescence were found in the abutments and backwalls. The paint on the abutments was also peeling and no settlement was evident. The channel was given a condition rating of 6. No evidence of scour was present, but there were signs that water may have reached the bottom flanges of the girders. Overall the structure requires minimal attention at this point in terms of maintenance. The inspection report can be found in its entirety in Appendix A.

4.2 Diagnostic Load Testing

To better understand the load distribution of Bridge 880.37 and to calibrate the finite element models, a diagnostic load test was performed. To prepare for the load test, the bridge was first studied to find the optimal sensor locations including the approximate locations of maximum stress and fatigue prone areas. The sensors used in this study were strain transducers from Bridge Diagnostics, Inc. (BDI), and the data acquisition system was the STS II structural testing equipment and software (BDI 2005).

4.2.1 Instrumentation Plan and Setup

To obtain the most useful strain data, the sensor locations were carefully selected. One of the primary purposes of the load test was to capture the live-load distribution through the structure so sensors were placed on selected girders, floorbeams, and stringers. To evaluate the level of rotational restraint provided by the riveted connections between the primary members, gauges were placed near the ends of selected stringers and floorbeams. To determine the transverse load distribution, sensors were placed on all four stringers and on both girders in one of the stringer bays near the center of the structure. Most sensors were located in high moment regions to ensure a significant level of strain. This reduces the effects of signal noise. To avoid local effects, the fixity between members was not monitored directly at the connections, but instead approximately 1 ft. (30.5 cm) from the connection. Thirty six sensors were used; 6 on the girders, 12 on the floorbeams, and 18 on the stringers. Figures 4.8 through 4.10 show the locations of all sensors.

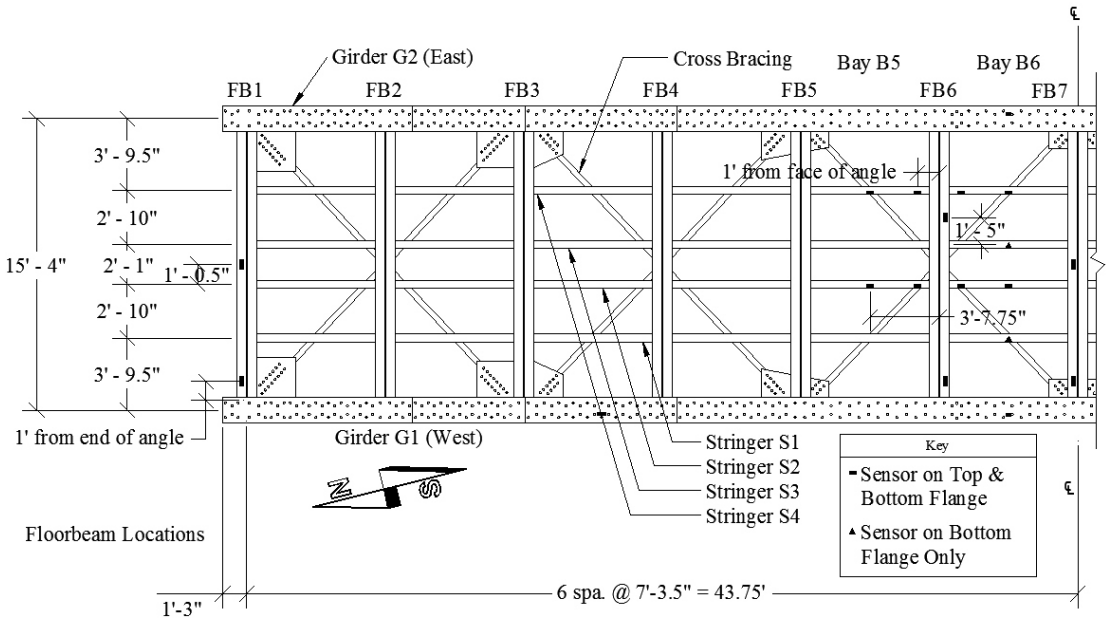

Figure 4.8: Plan view of Bridge 880.37 with sensor locations.

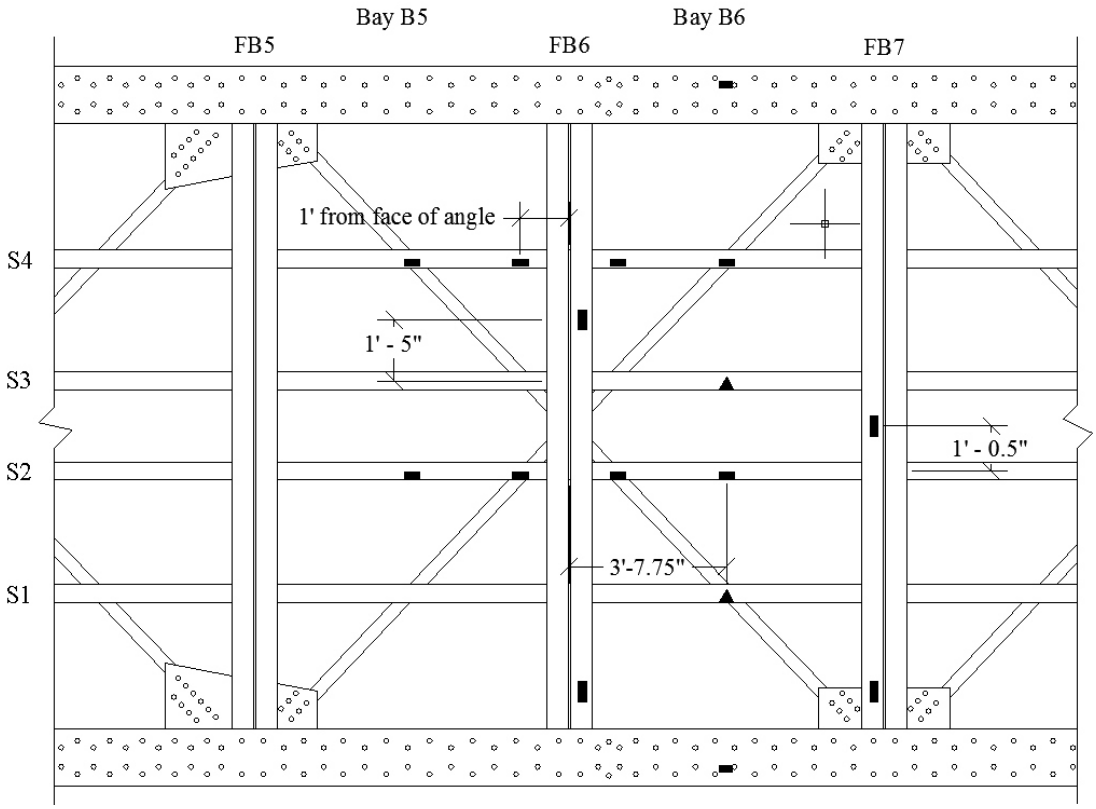

Figure 4.9: Detailed view of bays 5 and 6 with sensor locations for Bridge 880.37.

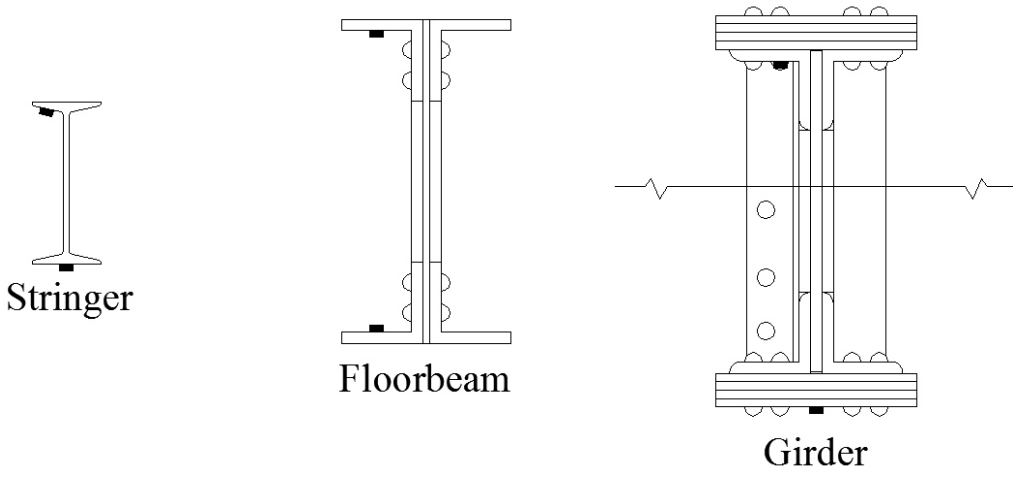

Figure 4.10: Cross-sectional views of a typical stringer, floorbeam, and girder showing sensor locations for Bridge 880.37.

4.2.2 Train Loading and Testing Procedure

Once the sensor locations were determined, the field work was planned and performed. The first step was to schedule a meeting with the railroad maintenance company, Herzog, to discuss the logistics of the test. Due to scheduling issues, it was decided that the trains could not be slowed from the normal operating speed of 79 mph (127.13 kph) for load testing. It was also stated that the proposed test set-up was not problematic to the maintenance company (Ted Keener, personal communication, June 16, 2010).

The next step was to travel to the Angostura Arroyo Bridge and mark the sensor locations. During this visit, some minor adjustments were made to the original instrumentation plan based on site conditions. All dirt and paint were removed from the steel members at the sensor locations (A total of 36). This involved scraping the top layers of dirt and paint from the steel, followed by cleaning the surface with an electric grinder.

The strain transducers also needed to be prepared prior to installation. To attach the gauges to the steel members, tabs were fastened to the sensors. The tabs allowed for a secure bond to the steel and relatively easy sensor removal since the strain gauge itself can be unbolted from the tabs. The tab installation involved cleaning the tabs with acetone to remove the adhesive from the previous use, placing the tabs in a special jig that spaces the tabs to the correct gauge distance, and fastening the tabs to the strain transducer using nuts and washers (see Figure 4.11).

Figure 4.11: Strain transducer in tab jig.

Setup of the instrumentation and data acquisition system, execution of the load tests, and takedown required approximately one day to complete. Setup involved attaching the strain transducers to the structure using a high-strength, quick setting epoxy along with a bond accelerator. Loctite Prism 410 instant adhesive and Loctite 7452 accelerator were used as recommended by BDI. First, a layer of epoxy was placed on the tabs, next the epoxy was sprayed with the accelerator, and finally the sensor was firmly held in place for 15 - 20 seconds. At this point, the sensor was securely attached to the structure (see Figure 4.12).

Figure 4.12: Strain gauges attached to a stringer.

Once the sensors were installed on the structure, they were each connected to one of the BDI-STSII units, which in turn were connected to the data logger using the cables provided by BDI. The sensors were automatically identified by the system, and therefore the channel into which each sensor was connected did not need to be recorded. Only the sensor number, which was clearly labeled on the transducer as shown in Figure 4.9, and its location on the structure were logged for each transducer. The data logger was then connected via a USB cable to a laptop equipped with the BDI software (WinSTS) for the purpose of controlling the test measurements and saving the strain data collected.

Once the test equipment was connected, the software was activated and the system was initialized. During this time the system identified the boxes and strain transducers. The data acquisition rate and the calibration file were then specified, along with a location to save the data files. The maximum data acquisition rate of 100 Hz was used due to the high speed of the trains. At this point, the BDI system was ready to take readings. Shortly before a train approached, the sensors were all set to a zero reading to remove the effects from temperature and random drift. Once a train came into view, the system was triggered and strain data was acquired until after the

last axle exited the structure. The data was then saved and reviewed during the time between load tests to ensure that all of the readings were reasonable, and corrections were made as needed. This process was repeated for each passing train.

Strain measurements were taken during the passage of six trains, five Rail Runner trains and one Amtrak train. Table 4.2 lists, in order of passing, the train type, the time that the train crossed the structure, the direction in which it crossed the bridge, and the train configuration based on observations made as the trains passed. Through consultation with a railroad engineer (Steven Dick, personal communication, October 19, 2010) the types of cars and engines were determined. The PhD dissertation of Steven Dick (2002) lists the configuration of each car and locomotive, in terms of the overall length, distances between wheels, and gross weight for all equipment that crossed the bridge during load testing except for the locomotives used for the Rail Runner. The configuration of the Rail Runner locomotive was found on the manufacturer's website (MotivePower 2010). The axle weights and spacing of each of the engine and car types that were carried by the bridge during the load tests are shown in Figures 4.13 and 4.14.

Table 4.2: Load test trains.

Test Run	Train Type	Time of Crossing	Direction	Configuration
1	Rail Runner	12:30 PM	Southbound	1 engine; 3 passenger cars
2	Amtrak	3:10 PM	Southbound	2 engines; 1 baggage car; 4 coach; 1 diner; 1 lounger; 3 sleepers
3	Rail Runner	4:45 PM	Northbound	3 passenger cars; 1 engine
4	Rail Runner	5:05 PM	Southbound	1 engine; 4 passenger cars
5	Rail Runner	5:59 PM	Northbound	2 passenger cars; 1 engine
6	Rail Runner	6:15 PM	Southbound	1 engine; 3 passenger cars

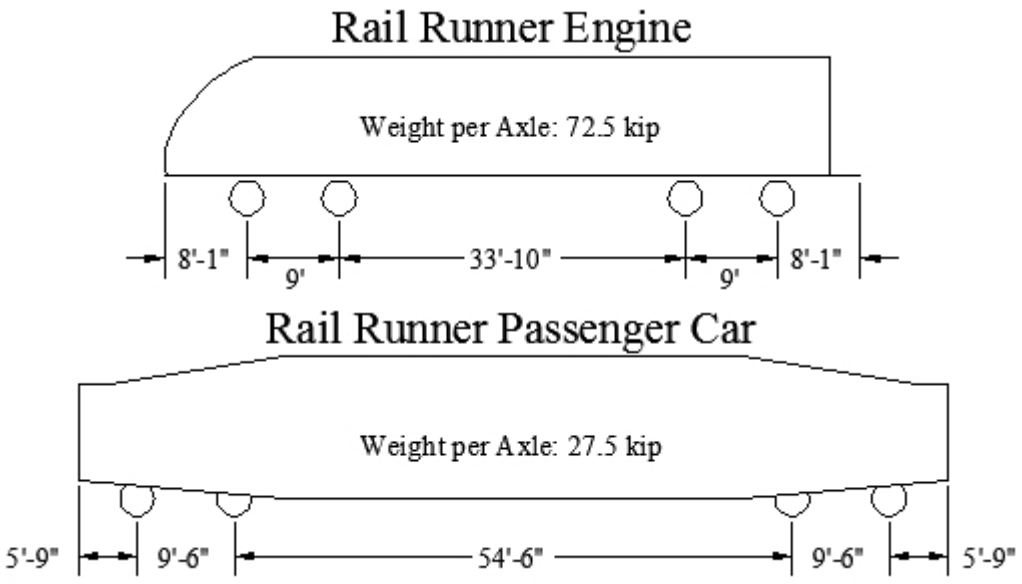

Figure 4.13: Engine and railcar configurations for Rail Runner Trains.

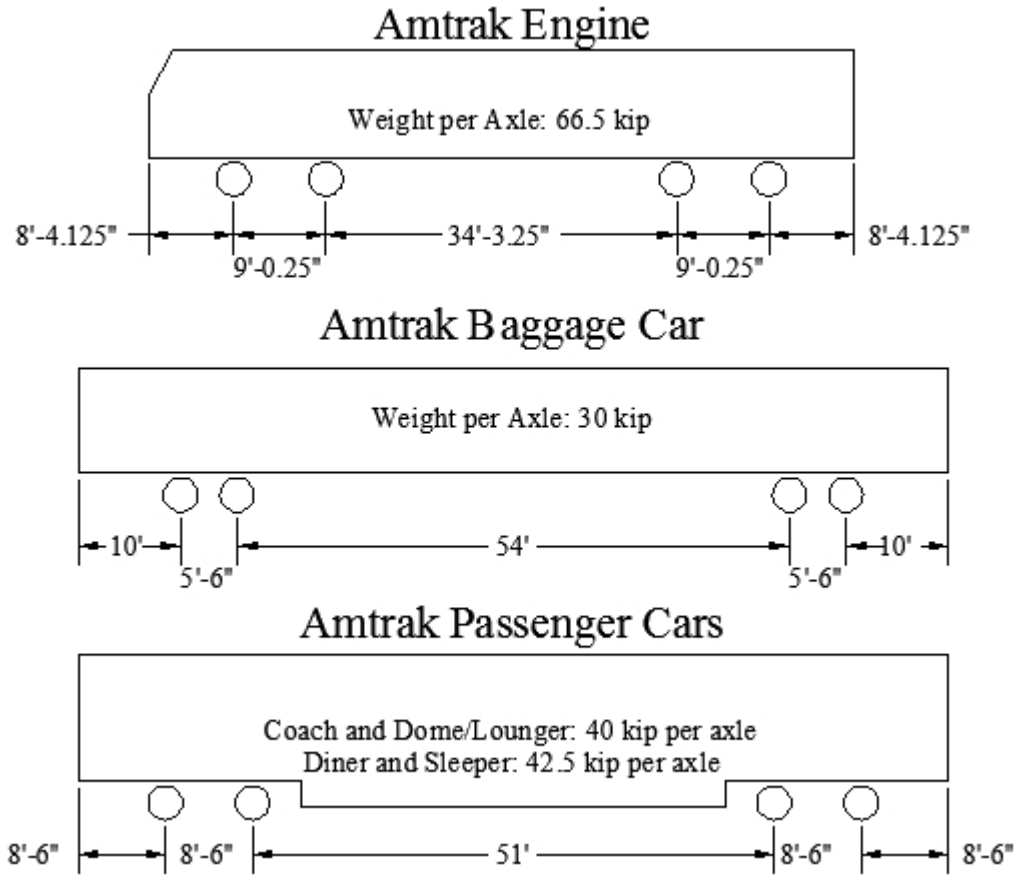

Figure 4.14: Engine and railcar configurations for Amtrak Trains.

4.3 Processing of Strain Measurements

Following the load tests, the measured strains were processed. First, the reading that occurred when the train entered the structure was determined. For southbound trains, this was taken as the first peak in the measured response at FB1 (see Figure 4.5 for member designations). For northbound trains, the reading corresponding to the front axle of the train directly above FB13 requires more effort to obtain since no strain gauges were placed on the southern half of the bridge. The strain at Fb13 was estimated by first identifying the data point that corresponded to the front axle of the train placed directly above FB1, which is the first peak in the data. At this point, the reading numbers must be represented as a distance traveled, so initially the speed of the train is assumed to be 79 mph (127.13 kph). The point corresponding to the train directly above FB1 is assigned a distance of 87.5 ft. (26.67 m), and each point before corresponds to front axle locations that are 1.17 ft. (35.7 cm) apart (i.e. 0.01 sec * 79 mph or 0.01 sec * 115.87 ft./sec = 1.17 ft. since time interval between measurements is 0.01 sec at 100Hz). Once each data point was assigned to a front axle location, the point corresponding to the front axle directly above FB13 could be determined.

To determine when the train exited the structure, a front axle location equal to the bridge length plus the length of the train was used as an approximation. At this point, the raw data chart (Figure 4.15) was cropped to include only the relevant strain readings (see Figure 4.16).

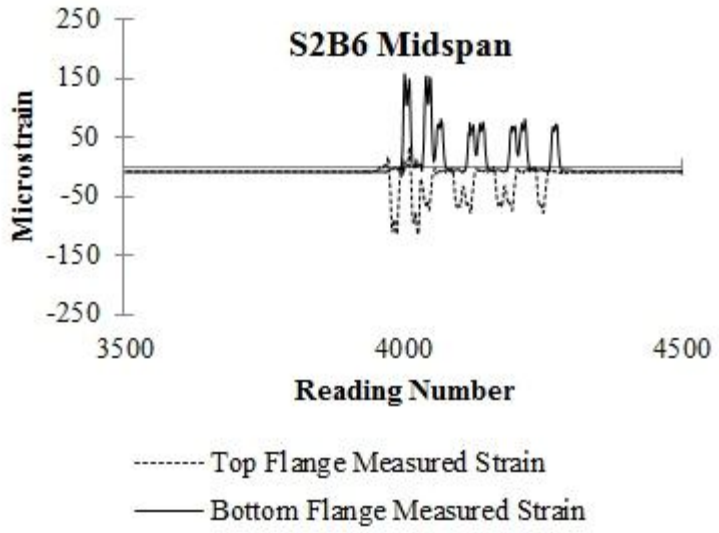

Figure 4.15: Raw strain data.

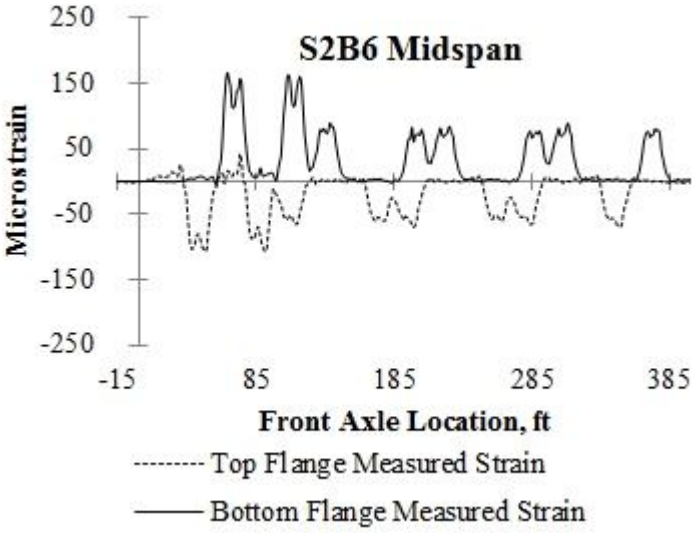

Figure 4.16: Raw data cropped and reading number converted to front axle location.

When comparing the raw strains with the simulated strains (which will be discussed in Chapter 5), it was found that there was a time lag in the readings from 20 of the gauges. This may have been caused by an anomaly in the equipment, causing some of the data to be shifted in time. The following gauges were affected (see Figures 4.5 and 4.8 through 4.10 for gauge locations): the top and bottom gauges at FB6 between S3 and S4; FB7 midspan and end; S2B5 midspan and

end; S2B6 end; S4B5 midspan and end; S4B6 midspan; and the bottom gauges at S2B6 and S3B6 midspan locations. This time lag appeared to be a malfunction of the testing equipment. At one location (S2B6 midspan), the bottom sensor was affected by this lag and the top one was not, which made correcting this error relatively simple. The time at which the first peak in the data occurred for each sensor could be compared and the time lag determined for each train (see Table 4.3). To correct for the time lag, the strain data that were affected by the lag were shifted to the left (see Figure 4.17).

Table 4.3: Calculated time lags.

Train	Time Lag (sec)
1	0.22
2	0.20
3	0.12
4	0.22
5	0.18
6	0.20

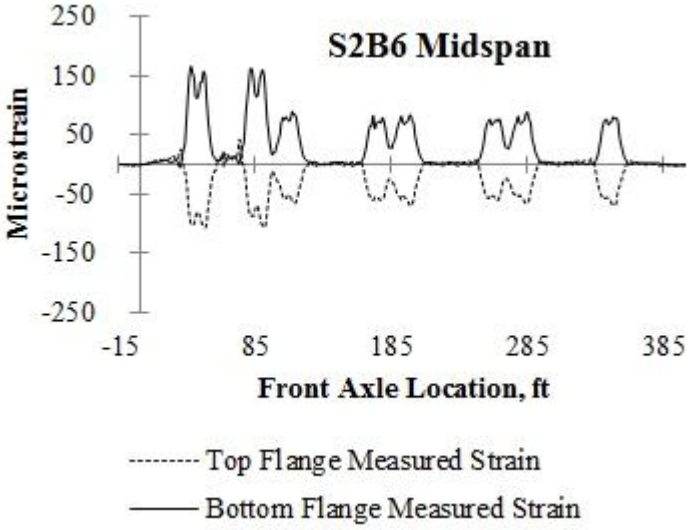

Figure 4.17: Data with all processing completed.

The data was also adjusted to remove the small drift that occurred while the train crossed the structure by subtracting the average reading before the train entered the bridge from the first reading, and the average reading after the train left the bridge from the last reading. Between the first and the last readings, the measured strains were adjusted based on a linear relationship as follows:

$$\varepsilon_{n.adj} = \varepsilon_{n.measured} - \varepsilon_0 + \frac{n}{N} * (\varepsilon_N - \varepsilon_0) \quad \text{EQ 4.1}$$

where $\varepsilon_{n.adj}$ is the adjusted strain reading; $\varepsilon_{n.measured}$ is the raw measured strain; ε_0 is the average of the strain readings before the train enters the structure; n is the reading number; N is the total number of readings during the period between the front axle of the train entering and the last axle leaving the bridge; and ε_N is the average of the strain readings after the last axle leaves the structure.

4.4 Discussion of Measured Data

All of the measured data were processed as described for each of the six trains. Once the charts were created, observations were made concerning the bridge behavior (e.g., load distribution, dynamic impact, rocking). The locations of maximum strain were determined, along with the maximum strains at critical fatigue details, namely the midspan locations of the floorbeams and girders. The measured strains were also used to determine the neutral axis location, which were compared against the values calculated based on the as-built drawings of the structure. The measured strains for Train 1 are shown in Figures 4.18 and 4.19. For Trains 2 through 6, the corresponding charts are available in Appendix A.

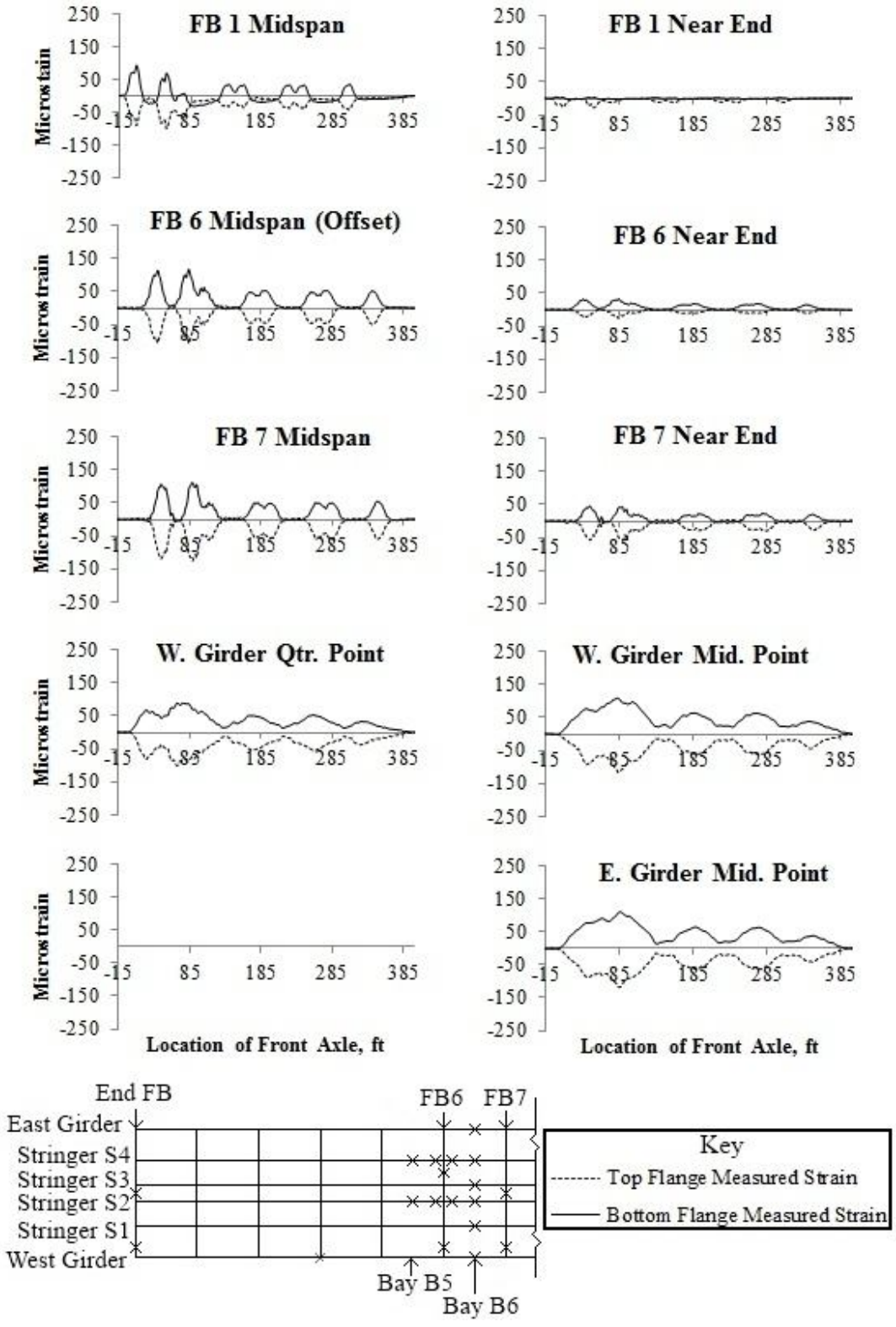

Figure 4.18: Measured strain data for Train 1.

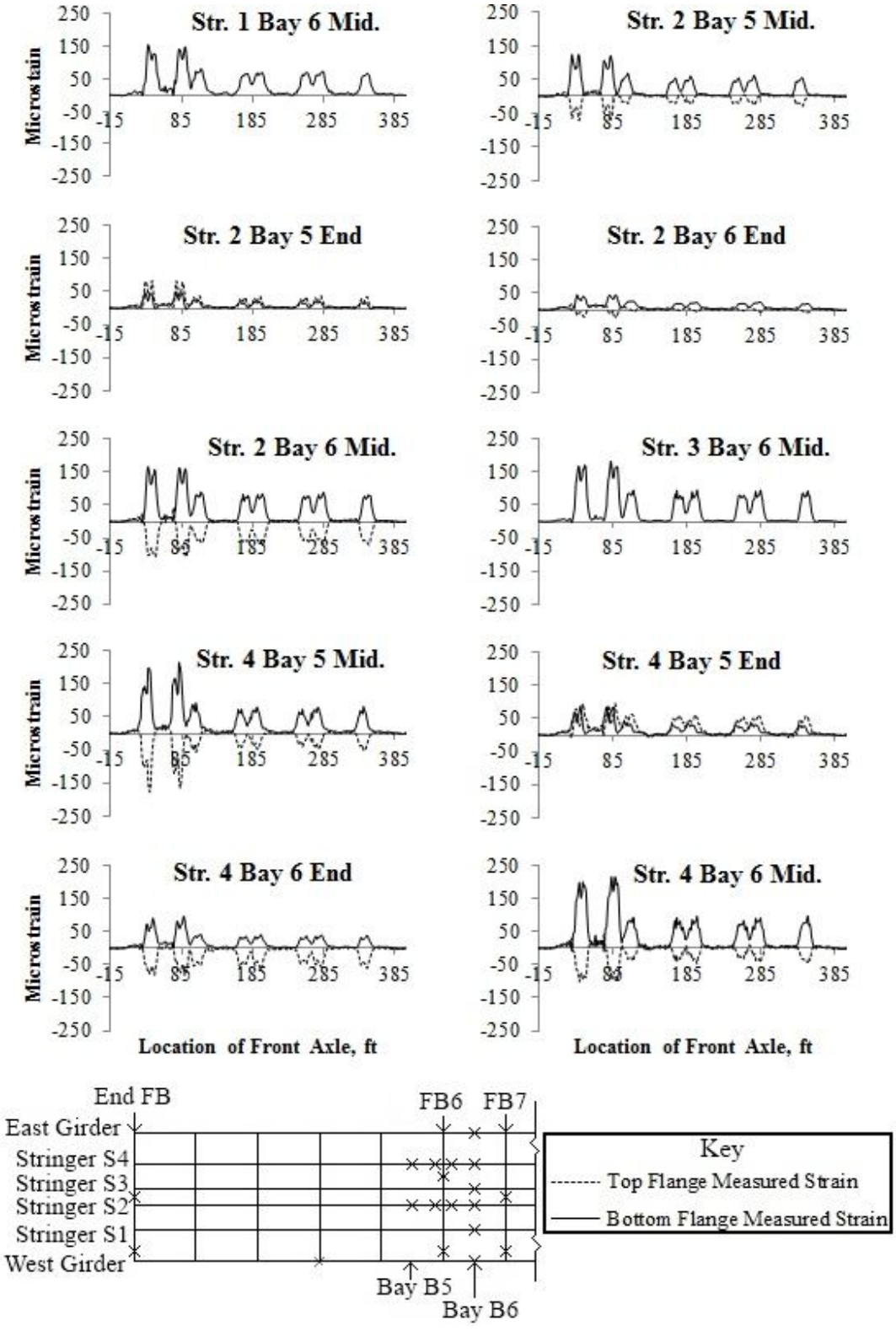

Figure 4.19: Measured strain data for Train 1 (cont.).

Overall, the strain data appeared reasonable. It was observed that the peak strains were greatest in the stringers (particularly in stringer S4), and similar in magnitude for the floorbeams and girders at midspan. The dynamic impact appeared to be minimal since the strain curves were generally smooth. This is expected since the ballast on the deck can dampen the dynamic effect of trains. The AREMA Specification (2007) accounts for this by reducing the vertical impact for design to 90% of the value calculated for non-ballasted decks.

There were some unexpected observations, most notably in Bay 5. Here the stringers appeared to experience a tensile axial force under live load. In this Bay, the top flanges of the instrumented stringers experienced less compression than expected at midspan and, at the ends of the stringers, the train load induced tension in both the top and bottom flanges (see Figure 4.19). Another observation was that the train load appeared to be entering the structure transversely off center. At B6 midspan, the level of strain increased from S1 to S4. Figure 4.20 shows the measured peak tensile strain data for stringer S1 plotted against the strain values for stringers S2, S3, and S4 for Train 1. Points that are above the 1:1 line indicate that the value for the stringer being compared is larger than the corresponding value for stringer S1. In this figure, the points that are closely grouped between 50 and 100 microstrain are the peaks in the data caused by the rail cars. The higher strains are caused by the locomotive. The points corresponding to the locomotive indicate a rise in strain from stringer S1 to stringer S4 at this location. Similar results were found for the data from Trains 2 through 6. A related observation is that this scatter is much greater for the locomotives than for the rail cars. This indicates that the asymmetric effect is greater for the locomotive.

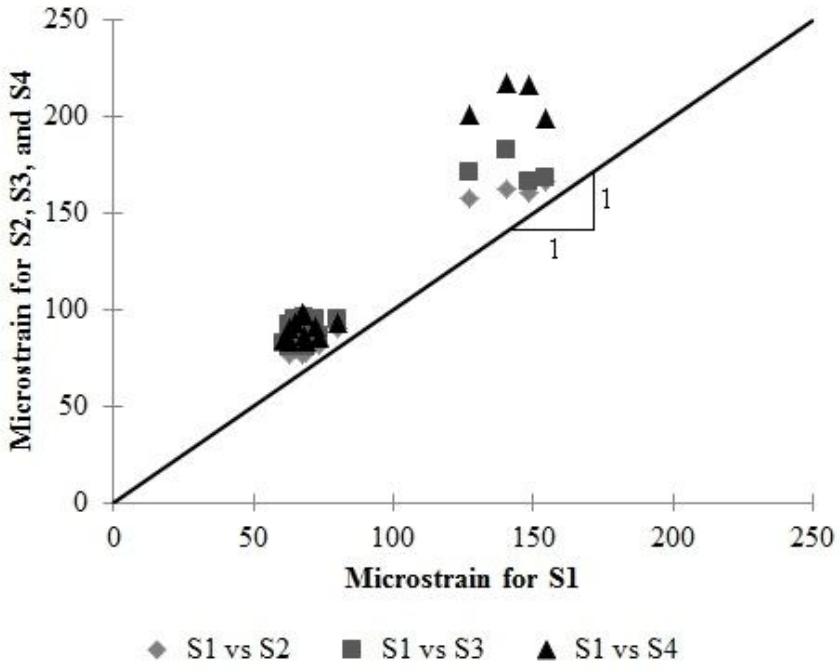

Figure 4.20: Comparison between peak measured strains at S1 vs. peak strains at other stringers for Train 1.

One possible explanation for this is that, when running at full speed, the locomotive's engine produces a torque, thus placing more weight on one side of the structure than the other. This would explain why the asymmetric loading was only apparent in the locomotive strain data. This effect should be studied in more detail so that it can be predicted and replicated in the structural model. Figure 4.21 demonstrates that the same effect is not present for the girders.

According to the measured strains, the riveted connections act essentially as pins. This is evident by the fact that there was no significant negative moment at any of the measured locations near the ends of the members (see Figure 4.13). Further evidence will be seen in Chapter 5 since the model that best fits the measured data used pinned connections between members.

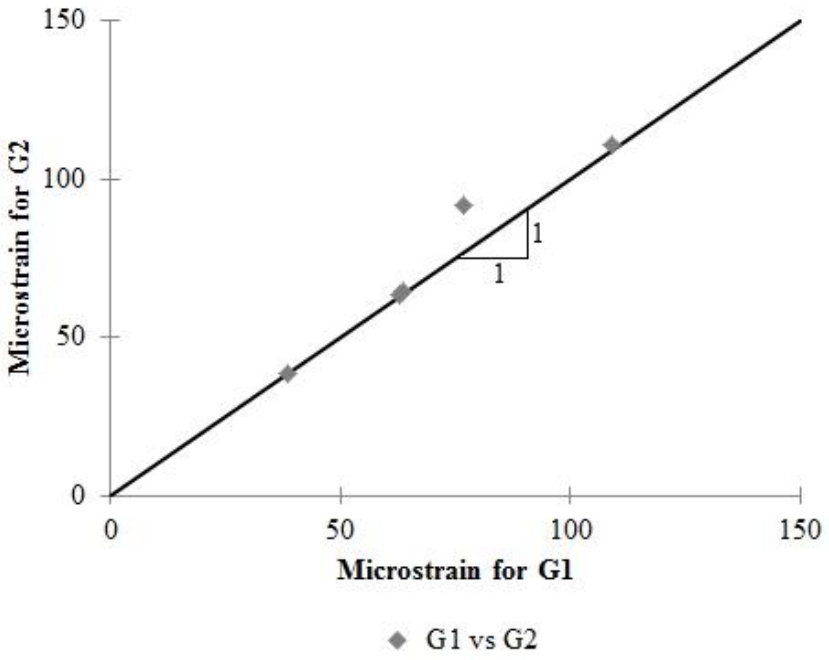

Figure 4.21: Comparison between peak measured strains at G1 vs. peak strains at other girders for Train 1 near midspan.

To further evaluate Bridge 880.37, the neutral axis locations were estimated from the measured strains. This neutral axis location was then compared to the theoretical values calculated from the as-built plans. The neutral axis is relatively simple to determine from the measured strains if a linear strain distribution is assumed. The neutral axis location, measured from the bottom of the member, at each point on the stringers and girders was calculated as:

$$\bar{x} = \frac{\varepsilon_b + \varepsilon_t}{h * \varepsilon_b} \qquad \text{EQ 4.2}$$

where $\bar{x}$ is the distance from the bottom of the member to the neutral axis; ε_b is the strain measured at the bottom of the member; ε_t is the strain measured at the gauge near the top of the member; and h is the distance between the two gauges. The distance between the two gauges is different for each member type. For the stringers, h is 11.43 in. (29.0 cm); for the floorbeams, it is 23.19 in. (58.9 cm); for the girder at the quarter point, it is 101.0 in. (256.5 cm); and for the

girders near midspan, it is 101.6 in. (258.1 cm). For the floorbeams, one gauge was placed on the top of the bottom flange, therefore EQ 4.2 must be slightly modified by adding the thickness of the bottom flange to $\bar{x}$. For all of the floorbeams, the thickness of the bottom flange is 13/16 in. (2.06 cm).

To reduce the level of error, the neutral axis was only calculated for relatively high values of strain (greater than or equal to 75% of the peak strain for the strain history) to minimize the effect of signal noise. Tables 4.4 and 4.5 show the neutral axis locations for all fully instrumented cross-sections away from the member ends. These neutral axis locations are compared with the values calculated from the as-built drawings in Table 4.6. In Table 4.6, the theoretical neutral axis locations compare well with the locations estimated from the measured strains for the floorbeams and girders, however there is a significant difference for the stringers. The difference in the neutral axis location may be the result of some combination of axial tension and partial composite action (i.e. the deck working with the stringers to resist the flexural stresses).

Table 4.4: Neutral axis locations for floorbeams and girders based on measured strains.

	Neutral Axis Locations (From Bottom)					
	FB1 Mid (in.)	FB6 (btw. S3 and S4) (in.)	FB7 Mid (in.)	G1 Qtr (in.)	G1B6 Mid (in.)	G2B6 Mid (in.)
Train 1	13.01	13.08	11.82	49.00	53.26	51.49
Train 2	12.75	13.24	11.83	47.94	54.91	50.84
Train 3	11.40	13.49	11.31	48.20	49.84	51.49
Train 4	12.07	13.16	11.72	48.74	52.87	51.88
Train 5	11.37	13.48	11.32	48.80	49.26	51.06
Train 6	12.33	13.15	11.79	48.81	48.25	52.00
Average	12.15	13.27	11.63	48.58	51.40	51.46

Table 4.5: Neutral axis locations for stringers based on measured strains.

	Neutral Axis Locations (From Bottom)			
	S2B6 Mid (in.)	S2B5 Mid (in.)	S4B6 Mid (in.)	S4B5 Mid (in.)
Train 1	7.04	7.59	7.90	6.44
Train 2	7.29	7.36	7.97	6.51
Train 3	7.03	7.74	7.88	6.74
Train 4	7.16	7.35	7.88	6.47
Train 5	7.06	7.78	7.81	6.66
Train 6	7.30	7.37	8.06	6.53
Average	7.15	7.53	7.92	6.56

Table 4.6: Comparison of neutral axis locations calculated from drawings and strain measurements.

	Neutral Axis Locations (From Bottom)		
	From Drawings in.	From Strain Data in.	% Difference %
Floorbeams	12.0	12.3	2.9%
Girder X5	51.8	48.5	-6.3%
Girder X6	52.5	51.4	-2.0%
Stringers	6.00	7.29	21.5%

If the interior stringers were fully composite, the neutral axis would be 9.47 in. (24.1 cm) from the bottom of the section for an interior stringer (assuming that the portion of the timber deck that acts compositely is the portion that extends half-way to the adjacent stringer on each side of the stringer), therefore it appears that the stringer acts neither fully composite nor independent of the timber deck. One significant evidence against partial composite action is that the composite action would increase the section modulus and therefore further reduce the predicted strains, which are already underestimated in some cases (see Chapter 6). Another possible explanation of the measured neutral axis location is that an axial tension is present in the stringers. One way to check for the presence of axial tension is to check the strains near the end. In Figure 4.19, a

varying degree of axial tension can be observed at Stringers 2 and 4 in Bays 5 and 6 as evidenced by higher tensile strains than compressive strains.

4.5 Summary

In this chapter, Bridge 880.37 was described along with the procedure for measuring strains under train traffic. Results from these load tests were presented and discussed. It was found that the data may indicate a low level of vertical dynamic impact due to limited observable vibrations in the measured data. It was also found that the train live load caused greater strains in the stringers on one side of the bridge than on the other, while the same effect was not noticeable for the girders. This asymmetric response may be the result of the rails not being centered on the structure, or uneven weight distribution of the rail equipment, particularly the locomotive. This may be attributed to differences in the amount of the train rocking on the stringers and girders. The fixity of the connections appear to be small since there was no evidence of negative moments observed near the ends. The neutral axis locations for all of the members were determined from the strain data. It was found that the neutral axis locations for the girders and floorbeams were close to the values calculated from the as-built drawings. For the stringers, however, the neutral axis locations were significantly different than the theoretical calculated locations. This may either indicate that the stringers act partially composite with the deck or that there is an axial tension. Since the deck is timber and not fastened to the stringers, it is more likely that a tensile force is acting on the stringers.

THIS PAGE INTENTIONALLY LEFT BLANK

CHAPTER 5

Finite Element Modeling and Analysis

5.1 Description of Finite Element Models

Four finite element models of Bridge 880.37 were created using SAP2000 (2010). Initial models included only the primary structural members (i.e., stringers, floorbeams, and girders). Each member was modeled with frame elements placed at the same horizontal plane for convenience in developing the models. One model was created assuming pinned connections between members (i.e. the riveted connections modeled with zero stiffness) and another one assuming rigid connections (i.e. the riveted connections modeled with infinite stiffness). These two models were then improved by adding springs to represent the ballast and frame elements to represent the rails and ties. These models will be referenced as shown in Table 5.1.

Table 5.1: Model designations

Designation	FB and Stringer End Condition	Track, Ties and Ballast Modeled?
Model 1	Pinned	No
Model 2	Fixed	No
Model 3	Pinned	Yes
Model 4	Fixed	Yes

Models 1 and 2 were used to determine the sensor locations and to estimate the level of strain expected during the load tests. After load testing, the finite-element model results were used to determine the actual speeds of the trains used in the load tests described in Chapter 4. All of the models were evaluated by comparing the simulated strains with the magnitudes of the measured strains. The model that most closely matched the measured behavior was determined. The

accuracy of the models is evaluated in Chapter 6. The best-fit model is used in Chapter 7 for the fatigue analysis of Bridge 880.37.

5.1.1 Basic Models

Models 1 and 2 included only the girders, floorbeams, and stringers (all on the same horizontal plane) with rigid members connecting the girder ends to the bearings, pin supported on one side and roller supported on the other (see Figure 5.1). The elevation of the horizontal plane was taken as the distance from the bottom of the girders at midspan to the girder centroid. Frame elements, which accommodate shear forces along the major and minor axes of the member, axial forces, bending moments about the major and minor axes, and torsional forces, were used to model all of the structural members.

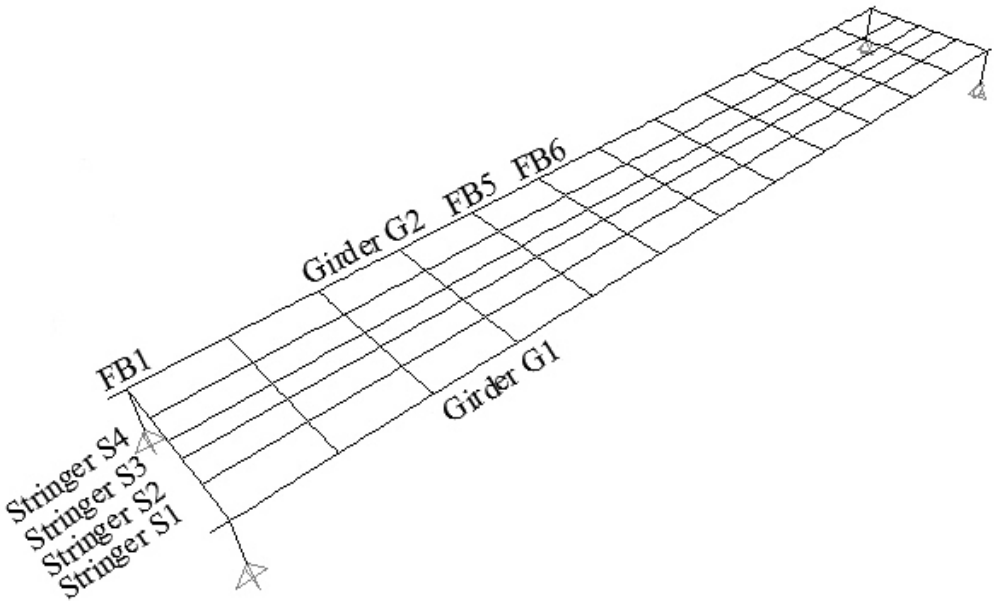

Figure 5.1: Isometric view of models 1 and 2 of Bridge 880.37.

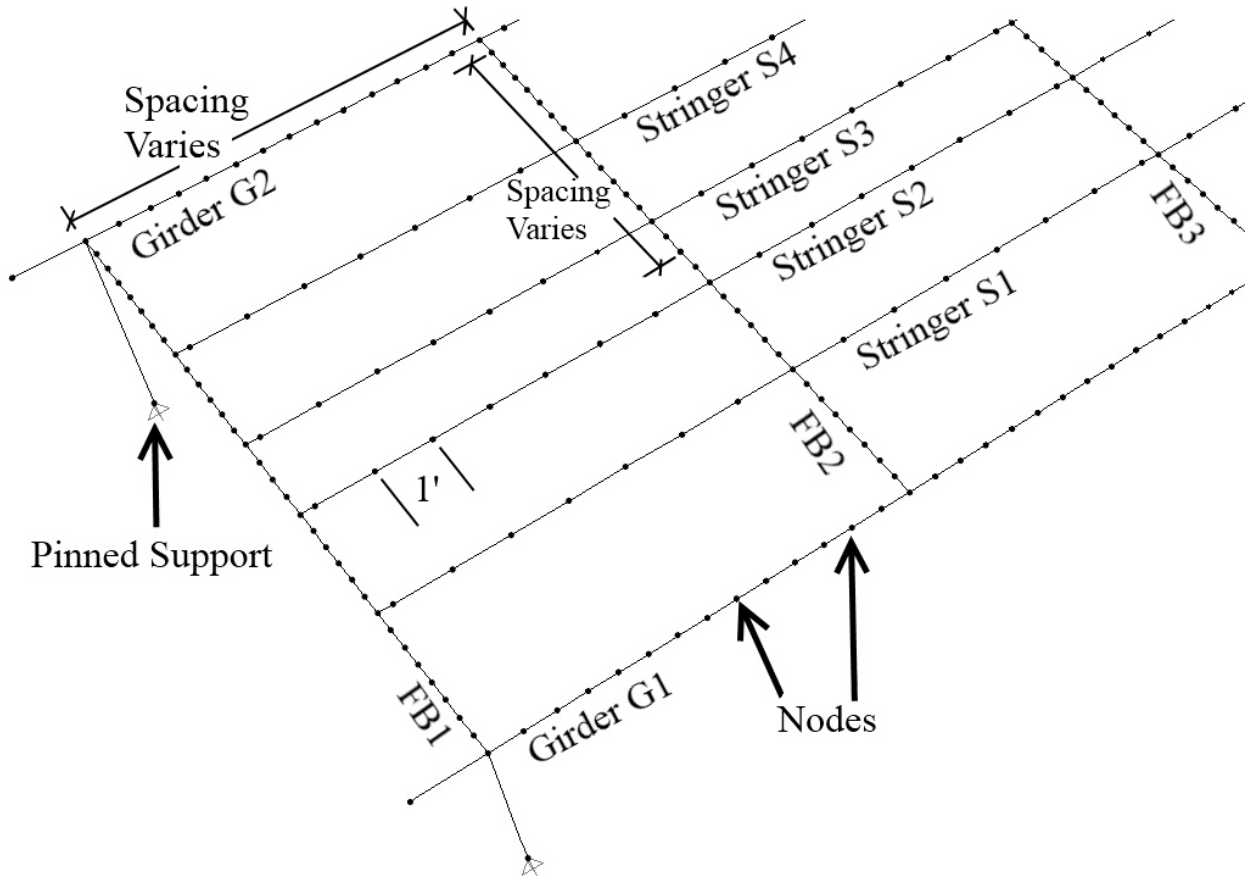

Figure 5.2: Detailed view for Models 1 and 2 near support.

For Bridge 880.37, there were a number of locations that required nodes for connectivity and to model changes in cross section along the length of the members. For the girders and floorbeams, these locations were first identified and then the lengths between these nodes were subdivided such that each segment was approximately 6 in. (15 cm) long. The stringers were divided with 12 in. (30.5 cm) nodal spacing to facilitate loading the structure and creating influence lines (discussed later in Section 5.2). Since the stringer length was not divisible by 12 in. (30.5 cm), shorter elements were used at both ends of the stringer. The stringer elements were placed symmetrically on the bridge; therefore, the first and last nodes were 0.25 ft. (7.62 cm) from the end floorbeams.

Section properties for the built-up girders and floorbeams were calculated with the aid of a spreadsheet. The properties calculated were the gross and net moments of inertia and section moduli; cross-sectional tension and shear areas; and the torsional constant. The riveted sections consisted of steel web plates, double-angle flanges, and cover plates (for the girders only). The stringer properties were found in the *Handbook of Steel Construction* (CISC 1967). The final section properties including the moment of inertia about the major (I_x) and minor (I_y) axes and the section modulus about the major (S_x) and minor (S_y) axes used in the finite-element models for the floor system components are shown in Table 5.2. In this table, the girder cross sections are designated X1 through X6 as illustrated in Figure 4.3.

The exact composition of the steel used in the construction of Bridge 880.37 is unknown since it was built over 100 years ago and no specifications were referenced in the available documentation. Based on information provided in the AREMA (2007) *Manual* and from information provided by an expert in the area of railroad bridge engineering (Steven Dick, email communication, May 23, 2011), it was assumed that steel properties included an elastic modulus of 29,000 ksi (200 GPa), a yield stress of 30 ksi (207 MPa), and an ultimate stress of 60 ksi (414 MPa).

Table 5.2: Section properties of the floor system members

	Area	Torsional Constant	I_x	I_y	Major Axis Shear Area	Minor Axis Shear Area	S_x	Sy
	in^2	in^4	in^4 (* 10^3)	in^4	in^2	in^2	in^3 (* 10^3)	in^3
Girder X1	76.08	4.714	121.5	540.7	37.41	27.00	234.2	67.59
Girder X2	79.62	5.735	129.3	711.4	37.41	31.00	239.5	88.93
Girder X3	86.80	7.037	149.3	711.4	37.41	41.00	297.9	88.93
Girder X4	104.5	25.26	195.1	1138	37.41	61.00	384.6	142.3
Girder X5	122.1	74.75	242.1	1565	37.41	81.00	471.3	195.6
Girder X6	139.8	171.1	290.2	1991	37.41	101.0	558.2	248.9
Floorbeam	45.68	3.562	4.093	142.4	13.43	19.50	0.3411	17.80
Stringer	10.20	0.5076	0.2270	10.00	5.104	5.096	0.03780	1.250

In Models 1 and 2, the train axle loads were applied directly to the stringers as point loads, thus ignoring the tracks, ties, and ballast. This modeling approach caused the simulated stresses in the stringers to be significantly higher than the actual measured values in most cases, since in reality the ballast distributes the load longitudinally. Also, the weight of the train is transferred to the structure primarily at the rail tie locations since the bearing area of the tie is much greater than that of the rail between the ties.

To obtain the influence line from the finite element model, a series of load cases was created. Influence lines are graphs that represent the response (i.e., shear, moment, or deflection) at a given point with respect to the location of a unit load moving across the structure. An influence line can then be used to determine the studied response under various loads by multiplying the influence line ordinate at the location of the load by the magnitude of the load. The first load case represented the 1 kip (4.4 kN) unit load reaching a position 0.25 ft. (7.6 cm) past the first floorbeam. This unit load was divided into four equal loads of 0.25 kip (1.1 kN) on each of the stringers. The remaining load cases consisted of the same loads moving across the bridge in 1.0 ft. (30.5 cm) increments. The influence lines for selected members and locations

are given in Figures 5.3 through 5.5 for both the pinned and fixed models (i.e. Models 1 and 2). In Chapter 4, it was shown that the measured strains at the ends of the stringers and floorbeams were minimal; therefore, only the influence lines for the midspan locations of floorbeams FB1 and FB7 (Figure 5.3) and stringers S2B5 and S2B6 (Figures 5.5) are shown. In Models 1 and 2, the four stringers behaved identically, therefore only one plot showing two locations on one stringer is sufficient. The influence lines near the quarter point and near the midspan of the girders are also shown.

The resulting influence lines from Models 1 and 2 were as expected. The results from the pinned model (Model 1) were all linear and closely agreed with manual calculations. The results for the fixed model correlated well with the pinned model (Model 2) but exhibited behavior that is typical of influence lines for indeterminate structures. That is, the curves are nonlinear and loading of adjacent stringer bays has an effect on the floorbeam or stringer moments at a given location. The influence lines for the girders are relatively simple and are not dependent on the fixity of the floor system connections. Because of the floor system, the girder influence line does not reach a sharp peak at B6 midspan. In Figure 5.3 through 5.5, the floorbeam locations are all specified by a tick mark on the x-axis.

The sharp peaks in the influence lines, particularly those for the stringers, indicate that the point load representation may be causing high strain estimates. To account for the load distribution through the ballast, and the fact that much of the load from the rails is transmitted through the ties, this model was improved by modeling the ballast, ties, and rails.

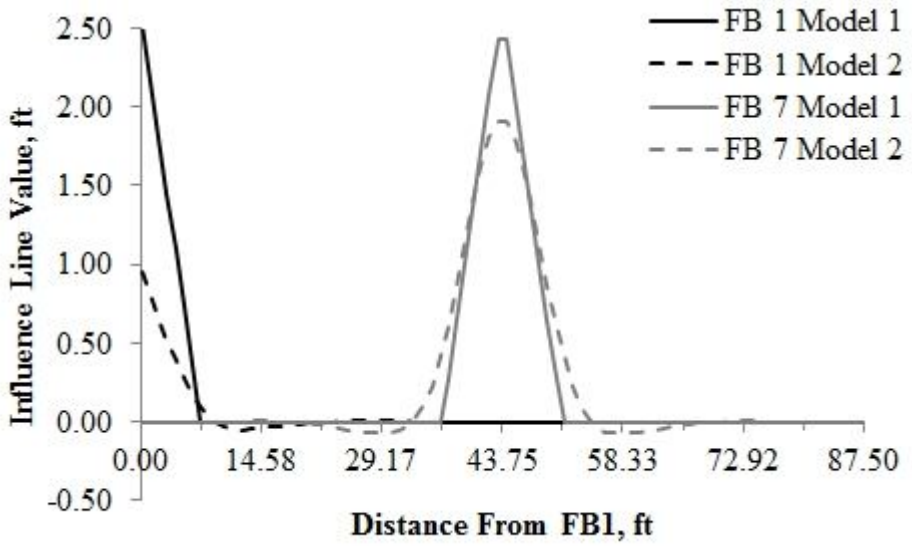

Figure 5.3: Influence lines for Models 1 and 2 at midspan locations of FB1 and FB7

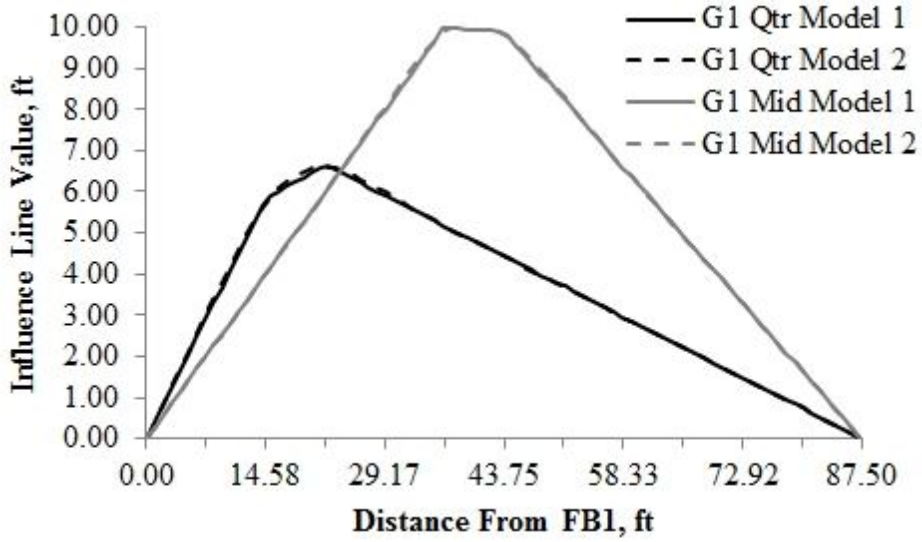

Figure 5.4: Influence lines for Models 1 and 2 at Bay 6 midspan and quarter point of girder G1

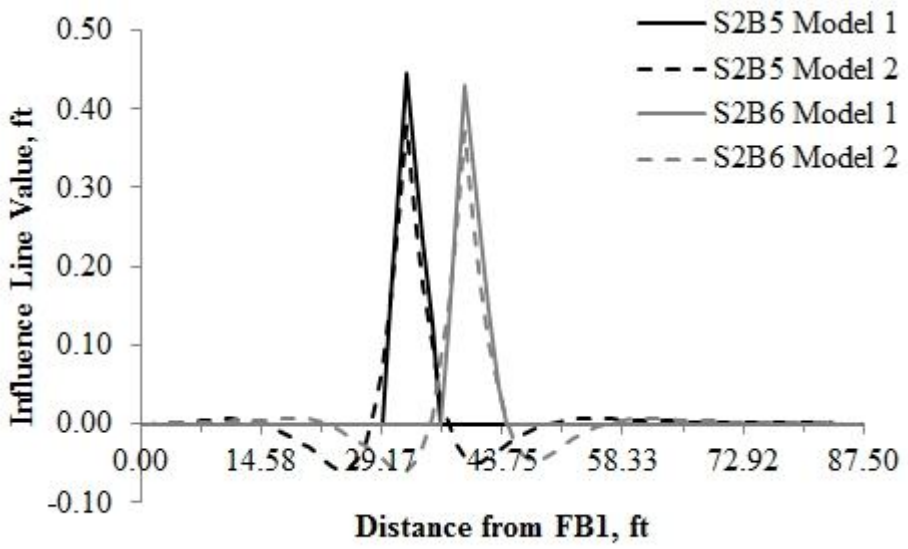

Figure 5.5: Influence lines for Models 1 and 2 at midspan locations of S2B6 and S2B5.

5.1.2 Refined Models

To improve the accuracy of the bridge model, elastic springs were used to represent the ballast, and frame elements were used to model the ties and rails (see Figure 5.6). This modification was made after initial review of the simulated strains from Models 1 and 2 which showed that the calculated strains were significantly conservative in some cases, particularly for the stringers. Spreading the load over a larger longitudinal distance reduced the simulated peak moment as demonstrated in the example given in Figure 5.7.

a)

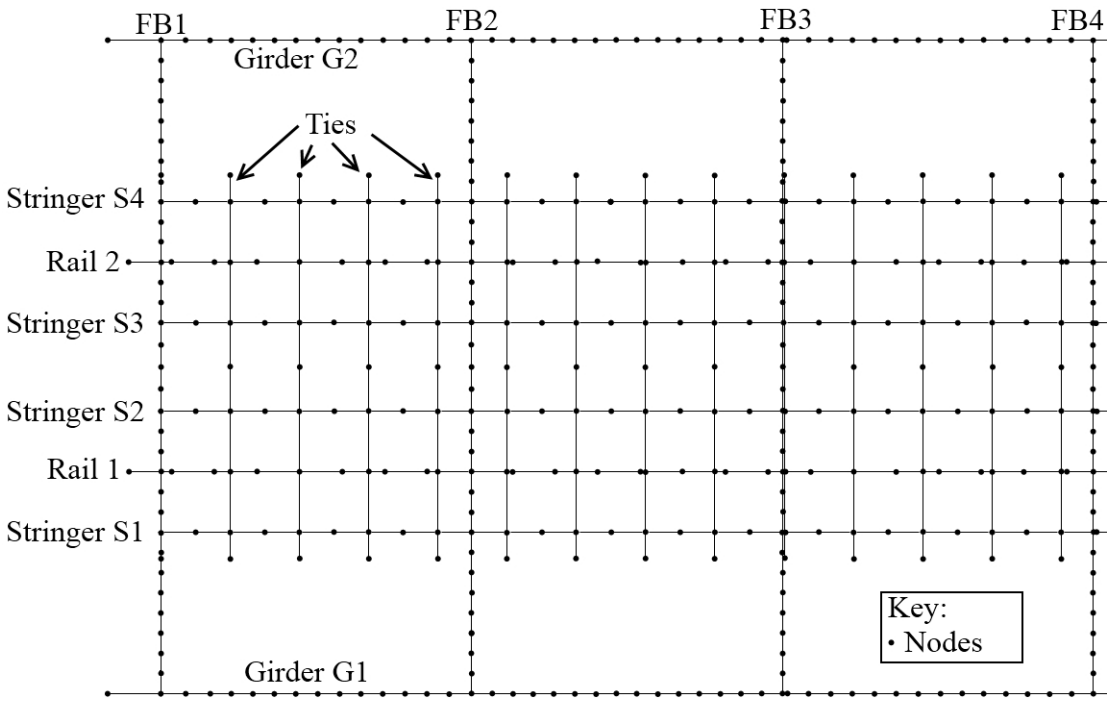

b)

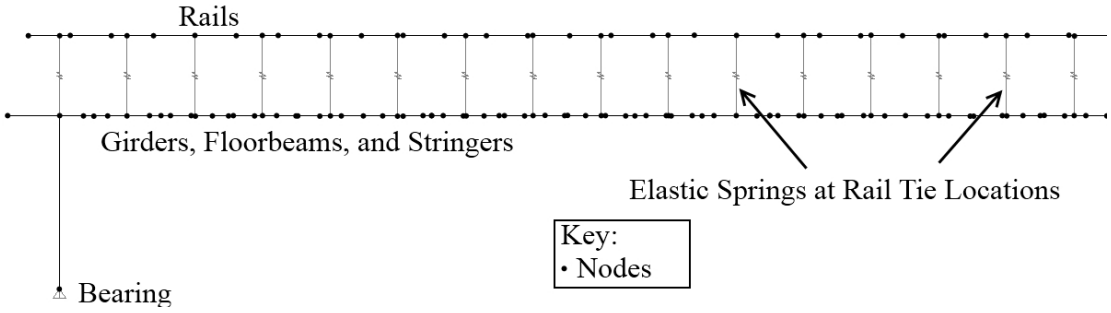

Figure 5.6: Models 3 and 4 of Bridge 880.37 near support a) plan view b) profile view.

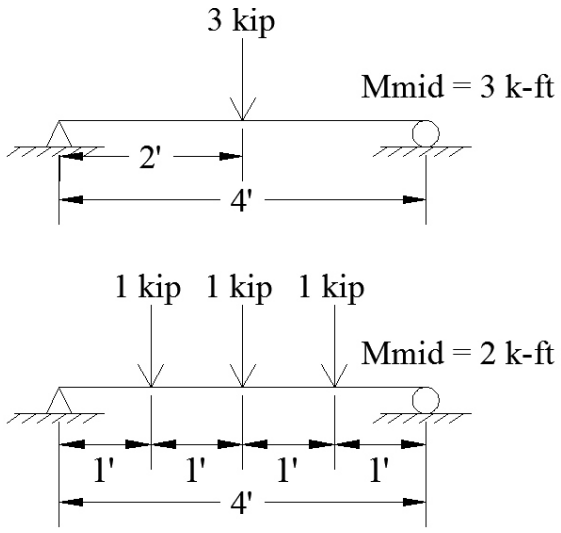

Figure 5.7: Example of beneficial effect of load spreading.

The elastic springs representing the ballast were placed vertically between the ties and the stringers at all rail tie locations. For Bridge 880.37, the ties were spaced at 19.5 in. (49.53 cm) on center and were 7 in. x 9 in. x 8 ft. nominal (17.78 cm x 22.86 cm x 2.44 m) timbers. The modulus of elasticity of the timber ties was taken as 1000 ksi (10.3 GPa) and a density of 60 lb./ft^3 (9.4kN/m^3) was used as per typical values from the National Design Specification (American Wood Council 2005). The cross-sectional dimensions of the rails are shown in Figure 4.2, and the properties are repeated in Table 5.3 along with those of the ties.

Table 5.3: Section properties of rails and ties.

	Area	Torsional Constant	I_x	I_y	Major Axis Shear Area	Minor Axis Shear Area	S_x	Sy
	in^2	in^4	in^4	in^4	in^2	in^2	in^3	in^3
Rail	13.33	6.240	94.20	14.44	3.638	4.819	28.20	4.813
Ties	55.25	408.1	194.5	332.7	55.25	55.25	59.85	78.27

The ballast consisted of crushed stone that was 10 in. (25.4 cm) deep measured from the top of the deck to the bottom of the ties. The modulus of elasticity was taken as 20 ksi (137.9 MPa), which is the average of 14.5 ksi (100 MPa) used by Yang, Powrie, and Priest (2009) and 24.7 ksi (170 MPa) used by Kuo and Huang (2009) for crushed stone railroad ballast. To obtain a spring constant for the elastic links, the entire track structure was assumed to be supported by the ballast located directly beneath the ties and the ballast contained in the area created by a 2:1 slope in each direction as shown in Figure 5.8.

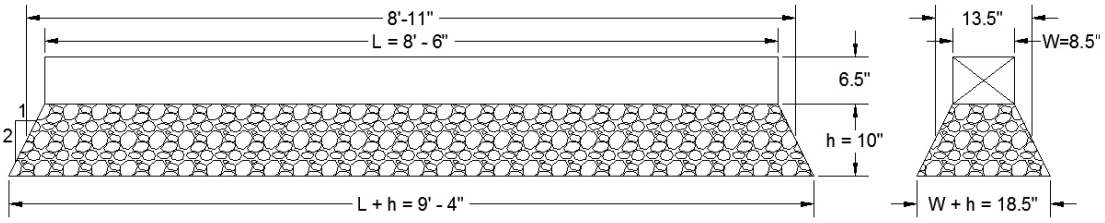

Figure 5.8: Illustration of ballast used in determining spring constant.

The spring constant was determined by assuming that the ballast is a perfectly elastic medium and by calculating the force required to cause a 1 in. (2.54 cm) deflection. Hooke's law states that:

$$\sigma = E * \varepsilon \qquad \text{EQ 5.1}$$

where σ is normal stress, ε is normal strain, and E is the modulus of elasticity. In this case, only axial loading was considered, therefore:

$$\sigma = \frac{P}{A} \qquad \text{EQ 5.2}$$

where P is the axial force and A is the cross sectional area taken at mid-height of the ballast (see Figure 5.8). The value of P that corresponds to a 1 in. (2.54 cm) deflection under the tie then

becomes the same as the spring constant, *K*, for the entire tie. The engineering strain of the ballast is:

$$\epsilon = \frac{\delta}{L} \qquad \text{EQ 5.3}$$

where δ is the deflection (equal to 1 in. (2.54 cm)) and L is the original length (equal to the ballast depth of 10 in. (25.4 cm)). Substituting the stress and strain terms and solving for $P/\delta = K$:

$$\frac{P}{\delta} = A * E * \frac{1}{L} = K \qquad \text{EQ 5.4}$$

Using the parameters defined earlier:

$$K = (8\,ft + 11\,in) * (13.5\,in) * 20\frac{kip}{in^2} * \frac{1}{10\,in} = 2{,}889\,kip/in\ (506\,MN/m) \qquad \text{EQ 5.5}$$

The spring constant for each of the links was assumed to be 25% of this value since the ballast can be modeled as four springs in parallel at each stringer location (assuming rigid body deformation of the ties), which amounts to 722.3 kip/in. or 8667 kip/ft. (126.5 MN/m).

For Models 3 and 4, the load was applied in a similar manner as Models 1 and 2, except that the loads were placed on the rails at 1.0 ft. intervals (0.305 m) instead of directly on the stringers. For the end floorbeams and girders, the results from Models 3 and 4 were very similar to the results from Models 1 and 2. For the stringers and interior floorbeams, however, the longitudinal distribution of load had a significant effect on the influence lines. The influence lines for Models 1 and 3 for S2B5, S2B6, S4B5, and S4B6, and midspan locations for FB1and FB7 are shown in Figures 5.9 through 5.11.

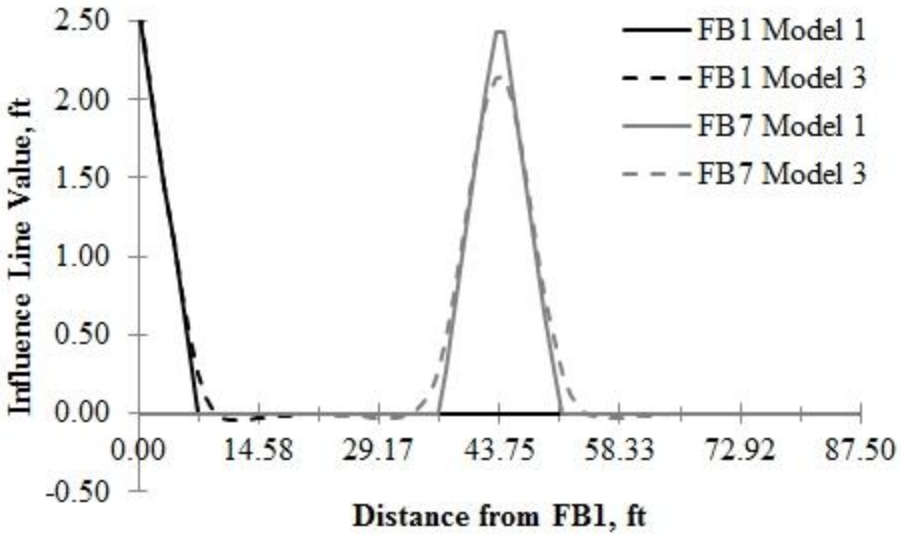

Figure 5.9: Influence lines for Models 1 and 3 at midspan locations of FB1 and FB7.

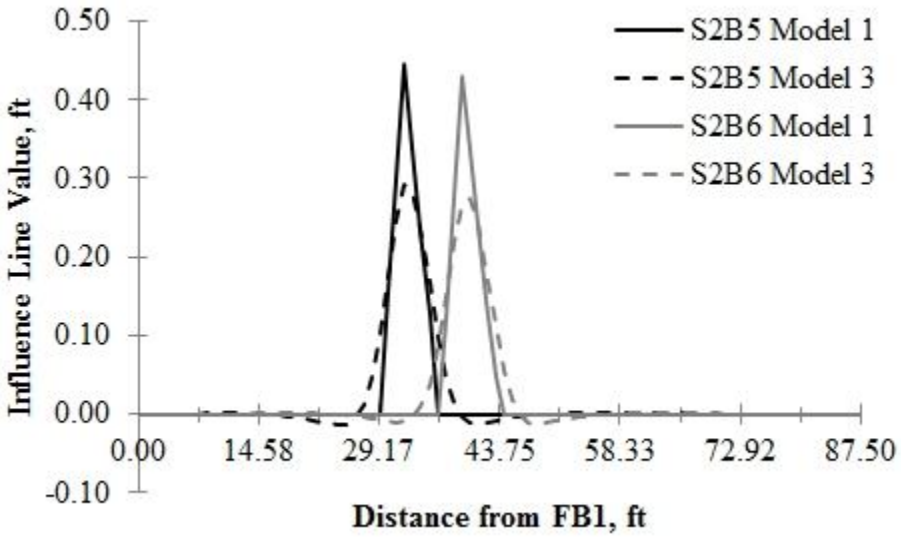

Figure 5.10: Influence lines for Models 1 and 3 at midspans of S2B5 and S2B6.

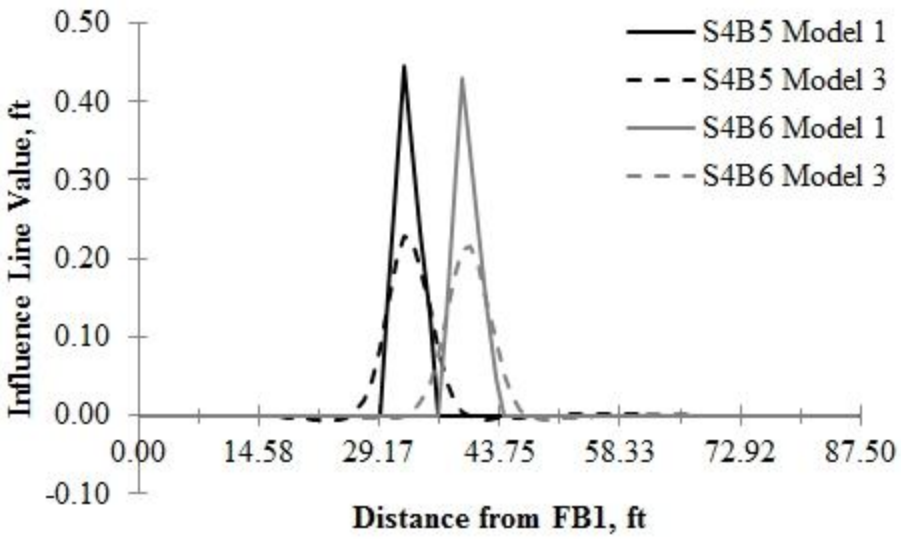

Figure 5.11: Influence lines for Models 1 and 3 at midspans of S4B5 and S4B6.

It was observed that the improved modeling of the load distribution through the ballast reduced the maximum moments in the stringers significantly. It was also found that when springs were used to represent the ballast, the influence line magnitudes were different for the interior and exterior stringers. At midspan of stringer bay 6, for example, the maximum influence line value decreased by approximately 36% for the interior stringers and 50% for the exterior stringers. This made the analytical results match the measured data much better for most of the stringer locations.

5.2 Generation of Influence Profiles

Instead of entering each train into the software program SAP2000, performing the analysis and cleaning up the data, the moments caused by the trains were determined using the influence lines previously discussed and matrix multiplication in MATLAB (Mathworks 2010) with a matrix that represents the train load. To obtain a moment history, which charts the

location of the train front axle versus the moment experienced at the location being considered, the following equation was used:

$$[M] = [IL][L] \quad \text{EQ 5.6}$$

where $[M]$ is a row vector with n columns that contains the moment magnitude at each loading step under the train load; n is the number of loading steps in 1 ft. (30.5 m) increments starting when the train enters the structure and ending when the train exits the structure; $[IL]$ is a row vector with m columns that contain the influence line magnitudes at 1 ft. (30.5 cm) intervals; m is the number of increments across the bridge; and $[L]$ is a m x n matrix that describes the moving train load as it traverses the structure. Each column of $[M]$ and $[L]$ are associated with the front axle locations starting at column 1 which corresponds to the front axle at 0.25 ft. (7.62 cm) past the first floorbeam and ending with column n, which corresponds to the last axle of the train 0.25 ft. (7.62 cm) from floorbeam 13. Each row of the $[L]$ matrix represents locations along the structure starting at 0.25 ft. (7.62 cm) past the first floorbeam to 0.25 ft. (7.62 cm) from the last floorbeam, in 1 ft. (0.305 m) increments. This method was used to obtain the moment history from simulated influence lines and known loads.

The method used to obtain the influence profiles can be illustrated by a simple example. Consider a simple-supported beam with a length of 10 ft. (3.05 m) loaded by a train load consisting of four 50 kip (222 kN) axles with axle spacing of 2 ft. (61.0 cm), 4 ft. (122 cm), and 2 ft. (61.0 cm) as shown in Figure 5.12.

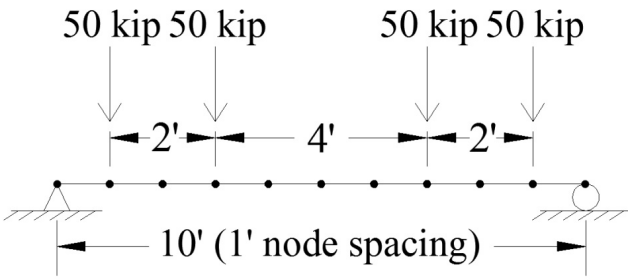

Figure 5.12: Example beam and loading to demonstrate calculation of moment history.

The first step is to obtain an influence line for the moment at midspan, which in this case is quite simple since the beam is determinate. The influence line increases linearly from each of the supports to a peak at midspan. The ordinate at the same location is the moment caused at midspan by a unit load placed at midspan, which is 2.5 ft. (76.2 cm) (see Figure 5.13).

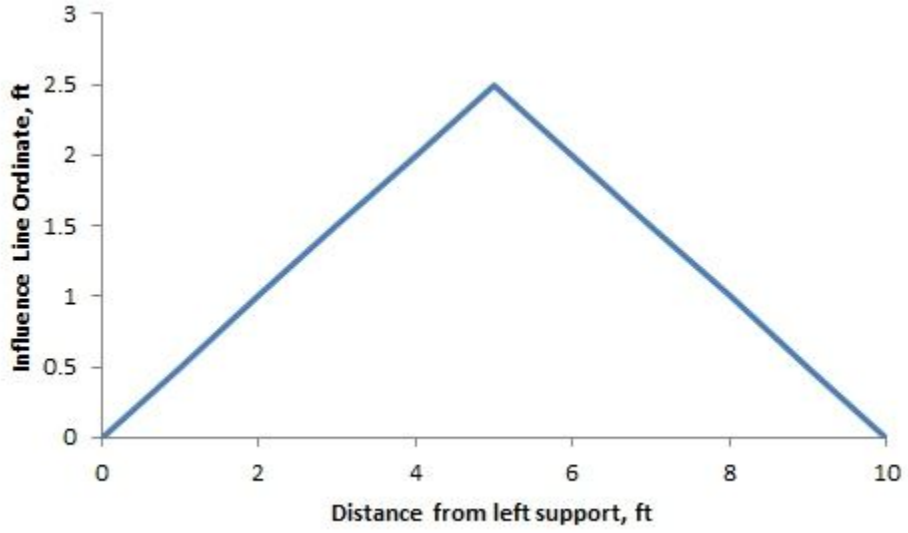

Figure 5.13: Midspan moment influence line for example.

The ordinates at each of the points along the bridge at 1 ft. (30.5 cm) intervals can be represented as a row vector as shown in Figure 5.14.

$$[IL] = (0 \quad 0.5 \quad 1.0 \quad 1.5 \quad 2.0 \quad 2.5 \quad 2.0 \quad 1.5 \quad 1.0 \quad 0.5 \quad 0)$$

Figure 5.14: Midspan moment influence line ordinates at 1 ft. (30.5 cm) intervals from beam example.

The next step is to produce the loading matrix for the train load defined in Figure 5.14. To do this, a row vector is first generated that represents the load itself, where the value in each cell represents the axle weights at each location, in 1 ft. (30.5 cm) intervals. Next, the number of rows in the [*L*] matrix (*m* in the discussion above) can be determined as the number of nodes when using 1 ft. (30.5 cm) increments across the bridge, which must equal the number of entries in [*IL*] (11 in this case). The number of columns in the [*L*] matrix (*n* in the discussion above) can be determined as the number of cells that completely describe the load (the length in ft.) plus *m* (i.e., in this case *n* = 8 to take into account the length of the load + 11 (*m* from above) = 19). The loading matrix is continued by entering zeros in column 1 (rows 2 through 11) and in row 1 (columns 10 through 19). The remaining cells are then filled in by setting them equal to the cell above and to the left. The final loading matrix is shown in Figure 5.15.

$$[L] = \begin{pmatrix}
50 & 0 & 50 & 0 & 0 & 0 & 50 & 0 & 50 & 0 & 0 & 0 & 0 & 0 & 0 & 0 & 0 & 0 & 0 \\
0 & 50 & 0 & 50 & 0 & 0 & 0 & 50 & 0 & 50 & 0 & 0 & 0 & 0 & 0 & 0 & 0 & 0 & 0 \\
0 & 0 & 50 & 0 & 50 & 0 & 0 & 0 & 50 & 0 & 50 & 0 & 0 & 0 & 0 & 0 & 0 & 0 & 0 \\
0 & 0 & 0 & 50 & 0 & 50 & 0 & 0 & 0 & 50 & 0 & 50 & 0 & 0 & 0 & 0 & 0 & 0 & 0 \\
0 & 0 & 0 & 0 & 50 & 0 & 50 & 0 & 0 & 0 & 50 & 0 & 50 & 0 & 0 & 0 & 0 & 0 & 0 \\
0 & 0 & 0 & 0 & 0 & 50 & 0 & 50 & 0 & 0 & 0 & 50 & 0 & 50 & 0 & 0 & 0 & 0 & 0 \\
0 & 0 & 0 & 0 & 0 & 0 & 50 & 0 & 50 & 0 & 0 & 0 & 50 & 0 & 50 & 0 & 0 & 0 & 0 \\
0 & 0 & 0 & 0 & 0 & 0 & 0 & 50 & 0 & 50 & 0 & 0 & 0 & 50 & 0 & 50 & 0 & 0 & 0 \\
0 & 0 & 0 & 0 & 0 & 0 & 0 & 0 & 50 & 0 & 50 & 0 & 0 & 0 & 50 & 0 & 50 & 0 & 0 \\
0 & 0 & 0 & 0 & 0 & 0 & 0 & 0 & 0 & 50 & 0 & 50 & 0 & 0 & 0 & 50 & 0 & 50 & 0 \\
0 & 0 & 0 & 0 & 0 & 0 & 0 & 0 & 0 & 0 & 50 & 0 & 50 & 0 & 0 & 0 & 50 & 0 & 50
\end{pmatrix}$$

Figure 5.15: Loading matrix for beam example (magnitudes are in kips).

Now that the influence line and loading matrices are compiled, the moment history can be calculated by simple matrix multiplication. The results of which are shown in Figure 5.16.

$$[M] = (0 \;\; 25 \;\; 50 \;\; 100 \;\; 150 \;\; 200 \;\; 200 \;\; 225 \;\; 200 \;\; 200 \;\; 200 \;\; 225 \;\; 200 \;\; 200 \;\; 150 \;\; 100 \;\; 50 \;\; 25 \;\; 0)$$

Figure 5.16: Moment history for illustrative example of a simply-supported beam (kip-ft.).

The moment history may also be displayed as a chart where the x-axis represents the front axle location and the y-axis represents the corresponding moment magnitude (see Figure 5.17). As can be seen by this simple example, the size of the matrices can become very large, and therefore the calculations are performed with the help of MATLAB (Mathworks 2010) for the actual moment histories presented in Section 6.1.

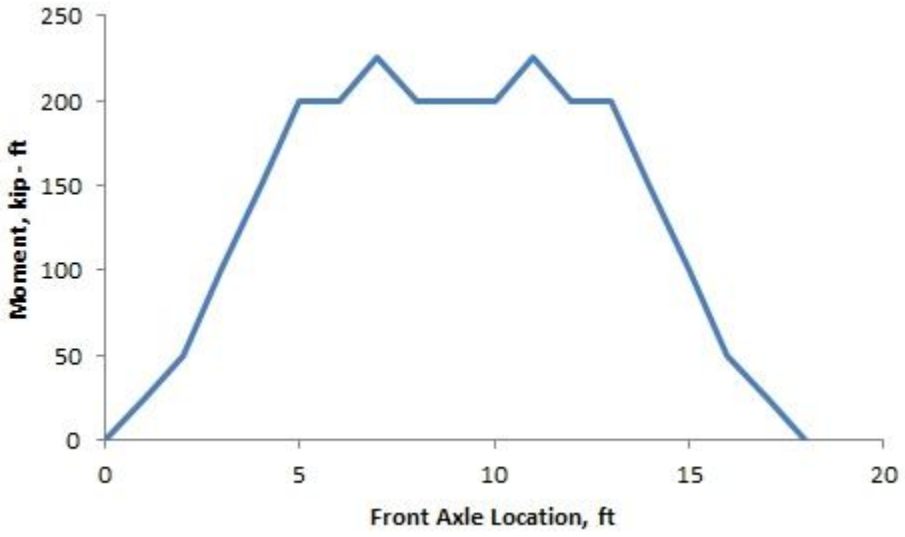

Figure 5.17: Moment history plot for illustrative example of a simply-supported beam.

The most difficult part of this method was to create the [L] matrix for each of the trains considered. To expedite this process, a spreadsheet was developed that only requires the configuration in terms of axle weight, axle spacing (AS), truck spacing (TC), number of axles (NA), gross weight (GW), and length over pulling force of couplers (LPFC), which is the overall

length of the rail car including the front and rear hitches, for each of the cars as defined in Figure 5.18.

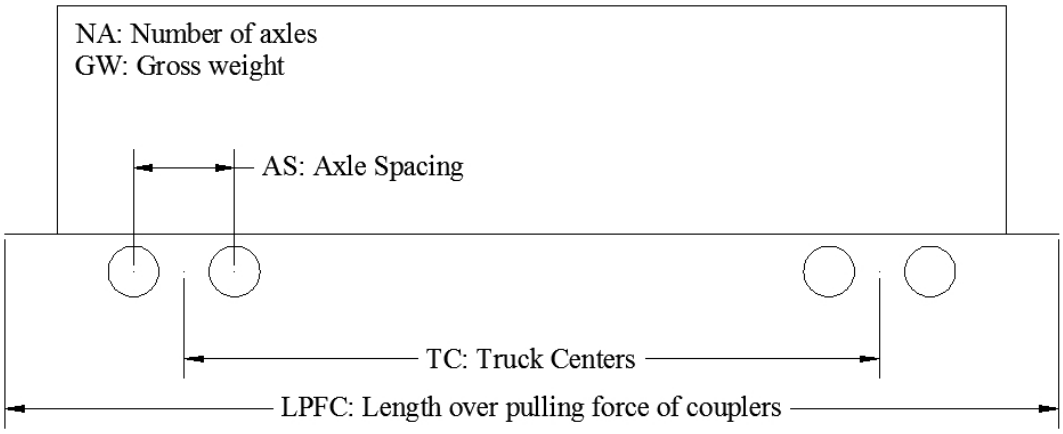

Figure 5.18: Identification of terms for describing train configurations.

Nested "if" functions were used to determine the axle weight at each location and to automatically create a vector that describes the configuration of the train. If an axle load occurs at a location between two nodes (e.g., at 20.5 ft. or 6.25 m), the load is divided between the adjacent nodes proportional to the distance between the other node and the axle.

For the [*IL*] and [*L*] matrices, it is extremely important to use the same length increment for the influence line as for the loading locations. This ensures that the matrix multiplication can be performed since the number of columns in the [*IL*] vector will be the same as the number of rows in the [*L*] matrix. Consistent length increments also makes it much simpler to create the [*L*] matrix since, in a spreadsheet, all of the cells except for the first column and first row are equal to the value of the cell above and to the left of that cell as shown in Figure 5.15.

Once the moment history is determined, the simulated strains can be computed and compared to the measured strains. To do this, the moment histories must be converted to strain histories by using the elastic equation for flexural stress:

$$[\varepsilon] = \frac{[M]}{S * E} \qquad \text{EQ 5.7}$$

where $[\varepsilon]$ is the simulated strain history vector; $[M]$ is the moment history vector; S is the section modulus at the location of interest; and E is the modulus of elasticity for the material. For riveted built-up sections, the section modulus is often different for the top and bottom of the members. For the compression flange, the gross section properties are used. For the tension flange, the net section properties are used since the rivets are not effective in resisting the tensile forces.

5.3 Summary

In this chapter, four finite element models of Bridge 880.37 were described and selected influence lines were presented. Comparisons were made between the models. It was found that Models 1 through 4 produced similar behavior for the end floorbeams and girders. However, significant differences were observed between the basic and refined models for the interior floorbeams and stringers. In general, the influence line magnitudes were significantly smaller for the refined models. Another difference was that the influence line ordinates for the refined models were significantly larger for the interior stringers than for the exterior stringers. The method for obtaining strain histories from the models was fully illustrated using a simplified beam example since the matrices for the actual structure were far too large to display. The method for computing the simulated strain histories for comparison with the measured strains was also introduced.

CHAPTER 6

Selection of Best Fit Model

6.1 Measured vs. Simulated Strains

To compare the simulated and measured strains, the first step was to ensure the two strain histories began at the same point. This was accomplished by matching the first data point in the simulated data, which corresponds to the train's front axle at a distance 0.25 ft (7.62 cm) beyond the first floorbeam, with the first peak in the measured data. Initially, the train speed was assumed to be 79 mph (127.1 kph) since that was the maximum speed permitted at this location (Ted Keener, personal communication, June 16, 2010). The actual speed can be more closely estimated by adjusting the speed used in setting the x-axis distance for the measured data such that the peaks in both data sets occur at the same time. It was found that the actual train speeds were all close to the maximum allowed and ranged from 75.5 to 78.5 mph (121.5 to 126.3 kph) (see Table 6.1).

Table 6.1: Train speeds determined through comparison with simulated data.

Train Number	Train Speed, mph (kph)
1	78.0 (125.5)
2	77.5 (124.7)
3	77.5 (124.7)
4	75.5 (121.5)
5	78.5 (126.3)
6	78.5 (126.3)

Once the data sets correlated well along the x-axis, meaningful comparisons (both qualitative and quantitative) could be made between the measured and simulated strain histories and the accuracy of the finite-element models could be evaluated. The measured and simulated

peak magnitudes were also directly compared. Charts were created where the measured peak strains were plotted along the horizontal axis and the simulated peak strains were plotted along the vertical axis. A line with a 1:1 slope was also plotted which represents perfect agreement between the simulated and measured responses. The vertical distance between a point on the graph and the 1:1 line represents the difference between the measured and simulated responses. In the charts for the bottom flange strains, points above the 1:1 line indicated that the simulated response was conservative (i.e. overestimated the strain level). In the charts for the top flange strains, a conservative model is indicated by points below the line since these strains are compressive (negative).

6.1.1 Main Girders

For the girders, the response from all four bridge models was nearly identical; therefore, only one model was required for making comparisons with the measured strains. The simulated strains matched the shape of the measured strain histories very well, particularly for the passenger cars, at both G1B3 midspan and G2B6 midspan locations, as can be seen in Figures 6.1 and 6.2, respectively. It is clear from these charts that the finite-element models overestimated the strain more for the locomotives than for the passenger cars. This is evidenced by the fact that the graphs for the simulated strains are greater than the measured strains for the first portion of the graph, particularly for the tension flange, which is the response under the locomotive. It is also clear that the simulated strains matched the top flange more closely than the bottom flange, which was also reflected in the difference between the measured neutral axis locations and the calculated values from the design plans (see Table 4.6).

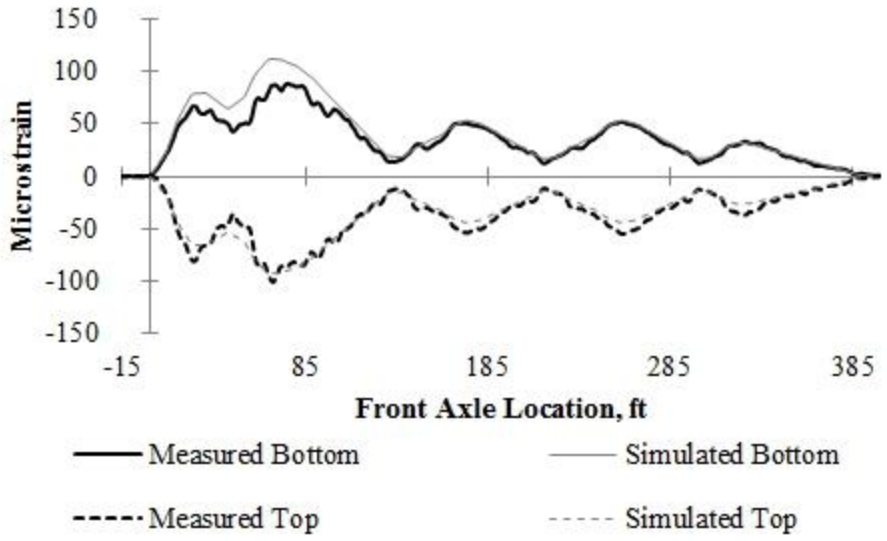

Figure 6.1: Measured vs. simulated strains for Train 1 at G1B3 midspan.

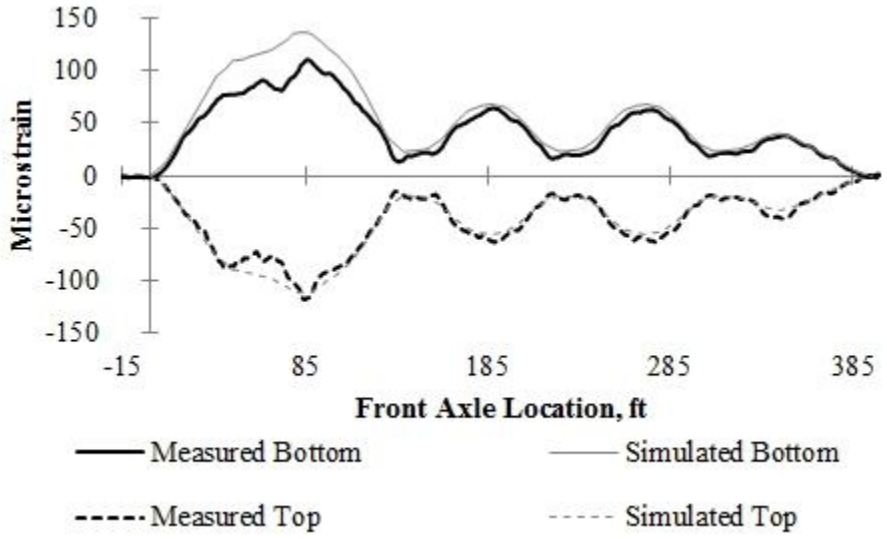

Figure 6.2: Measured vs. simulated strains for Train 1 at G2B6 midspan.

As discussed earlier, plots were developed that compare the peak values from the measured strain histories against the corresponding values for the simulated histories to further quantify how well the model and measured data match. Figures 6.3 and 6.4 show that the model matches better for all of the Rail Runner passenger cars (which are represented by the two groups of data points between 0 and 60 microstrain in Figure 6.3 a.) than for the locomotives (which are

represented by the two groups of points between 60 and 90 microstrain in Figure 6.3 a.), particularly for the bottom flange locations. This effect is smaller for the to flange, but still present, which can be attributed to the difference between the actual neutral axis location and the location calculated from the as-built plans. There is a notable difference in how well the data matches for the Rail Runner trains (Trains 1 and 3 through 6) compared to the Amtrak train (Train 2). This can be attributed to the accuracy of the estimated train weights. From the data, it would appear that the estimated weights for the Rail Runner passenger cars were most accurate and that the weight of the locomotive was overestimated. The accuracy of the estimated weight of the Amtrak equipment appears to be similar for all passenger cars and locomotives, but a little bit high. It is also noteworthy that the estimated weights for the passenger cars were more conservative for the Amtrak train than for the Rail Runner trains.

The weights of the railcars for the Rail Runner were similar from train to train, however a small variance can be observed by noting the horizontal scatter within groups of points. In the model, each rail car was assumed to have the same weight; therefore, each occurrence of the same car will appear at the same vertical location on these charts (i.e. with the same simulated strain). Variation in the measured response (scatter in the horizontal direction) indicates different actual weights, which is logical since the trains may carry a different number of people. This effect can be seen for both the top and bottom flange data.

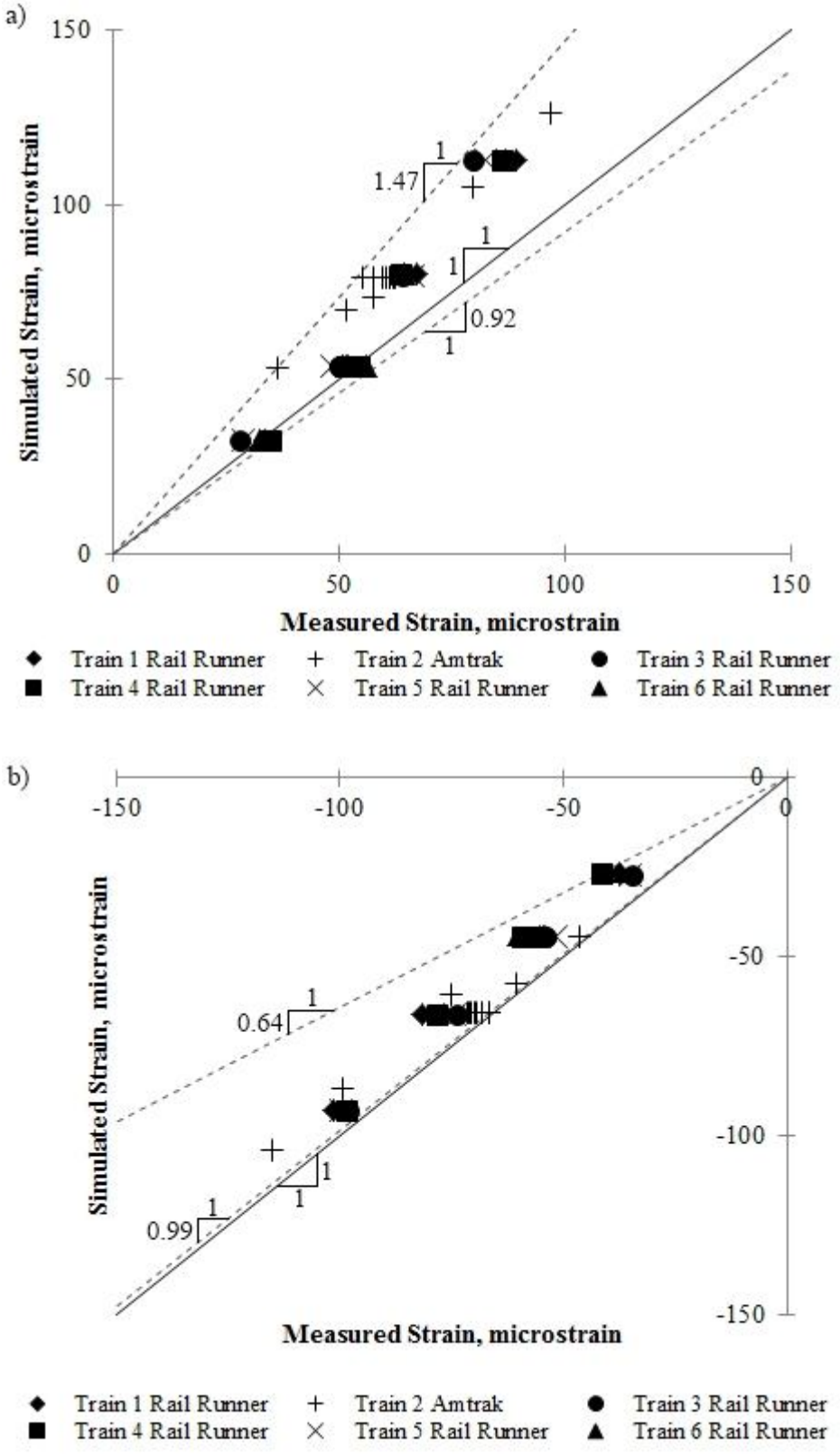

Figure 6.3: Peak measured vs. simulated strains for all trains at G1B3 midspan: a) bottom flange and b) top flange.

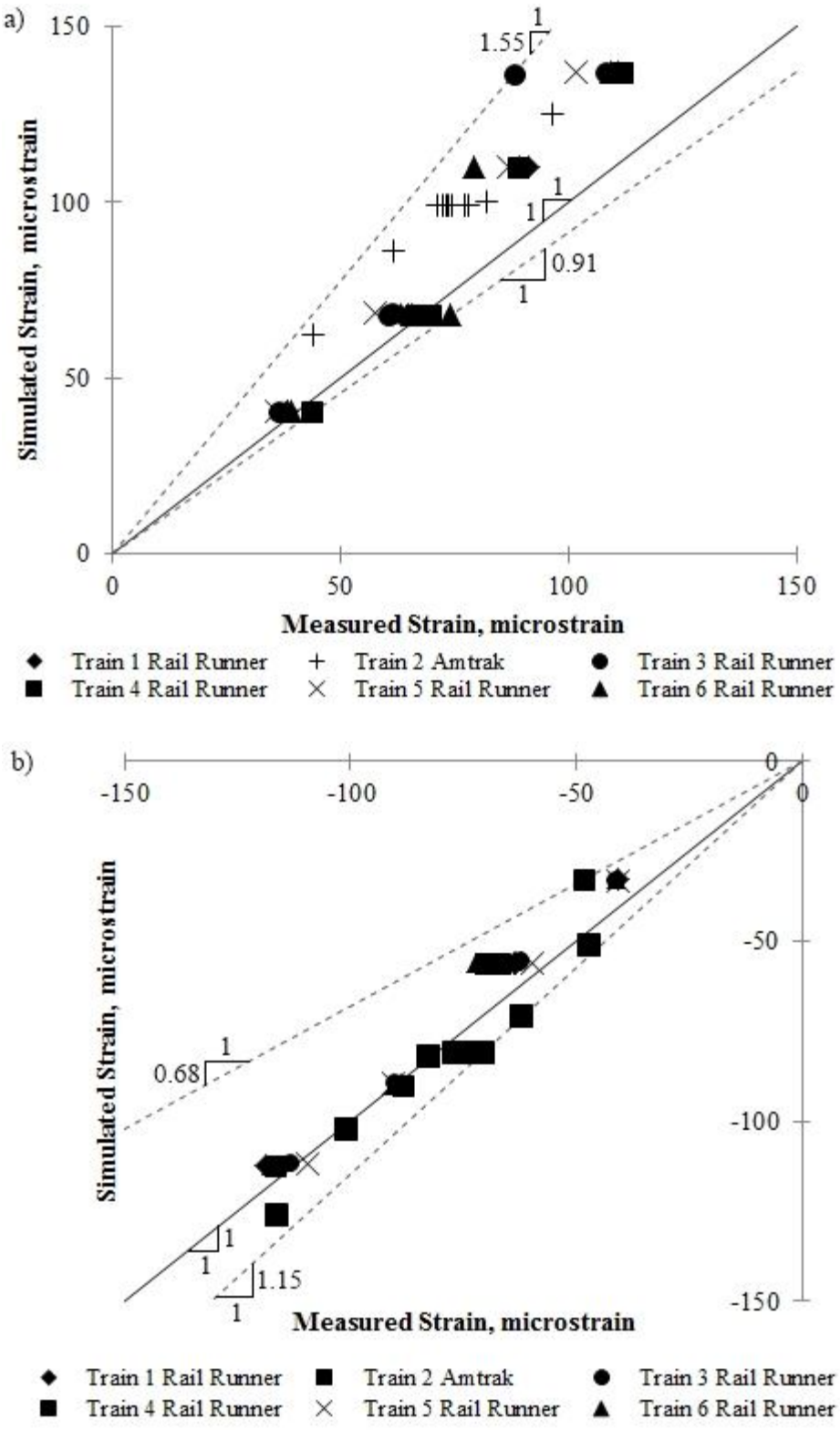

Figure 6.4: Peak measured vs. simulated strains for all trains at G2B6 midspan: a) bottom flange and b) top flange.

6.1.2 Floor Beams

Similar comparisons were made for the floorbeams as for the girders. Two floorbeam locations were chosen for discussion. The midspan locations of FB1 and FB7 were chosen since these are critical locations for fatigue on the floorbeams. Minimal moment was measured at the end connections of the floorbeams. The behavior of the models at the FB1 and FB7 midspan locations was significantly different (see Figures 6.5 and 6.6). Models 1 and 3 provided nearly identical results at both locations. One explanation for this behavior is that the load spreading through the ballast does not significantly influence the transverse members (i.e., floorbeams). More detailed modeling would be required to more accurately capture the behavior in this location. For FB1 midspan, the behavior was significantly affected by the fixity of the floorbeam ends, as seen in Figure 6.5, which compares Models 3 and 4. This can be explained by the insensitivity of the finite-element for the floorbeam model to the load spreading effect. For FB7 midspan, the end fixity has very little impact on the simulated strains (see Figure 6.6). This makes sense because the supports provide a torsional resistance that is not available away from the supports.

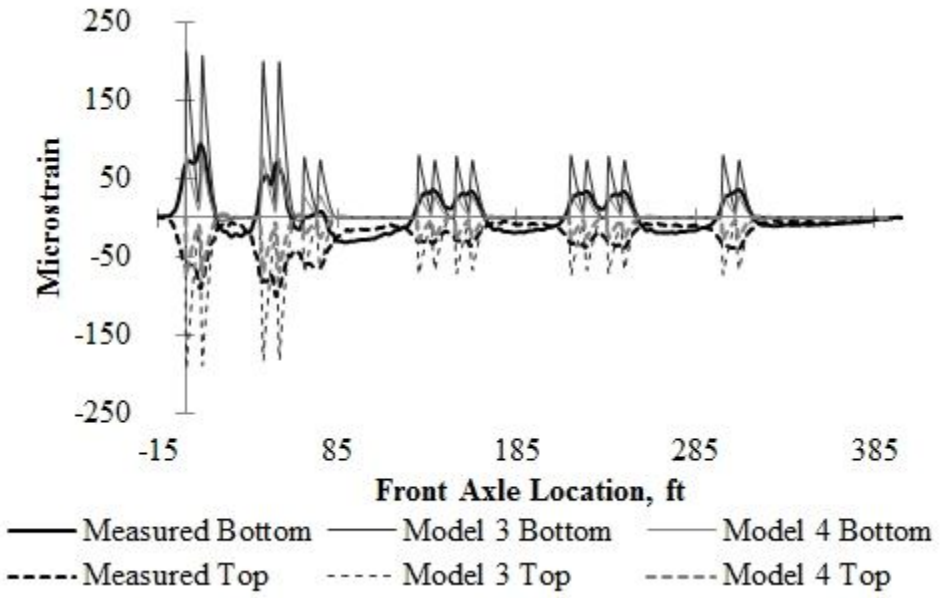

Figure 6.5: Measured vs. simulated strains for Train 1 at FB1 midpoint.

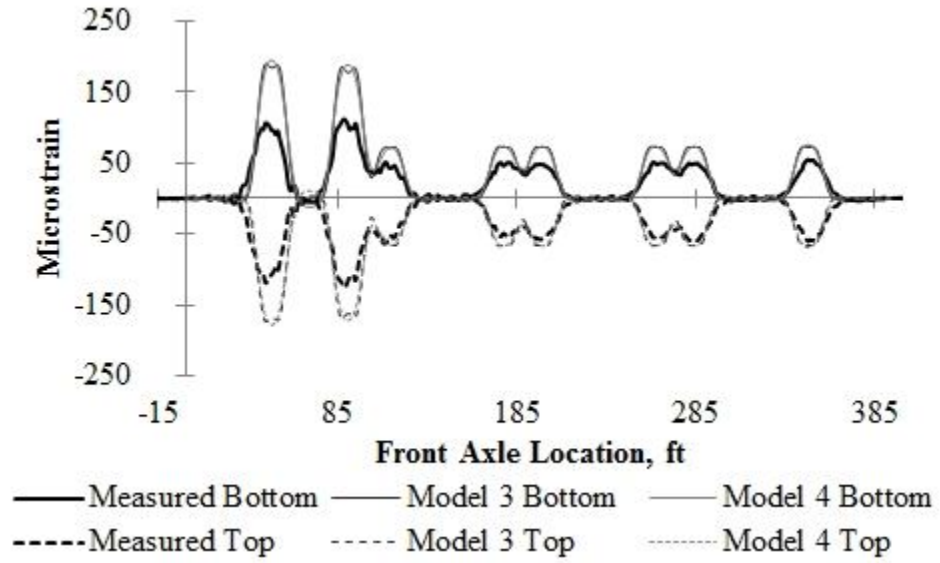

Figure 6.6: Measured vs. simulated strains for Train 1 at FB7 midpoint.

In general, the simulated strains did not match the measured strains as well for the floorbeams as for the girders, particularly for the locomotives. The lower measured strains may be attributed to overestimating the train equipment weight. The shape of the simulated strain history matched the measured data well for the FB7 midpoint location. For the interior

floorbeams, Model 3 tended to fit the shape of the measured curve slightly better than Model 1 (not shown) since it accounts for the small peaks under each axle instead of just simulating one peak under each pair of axles.

The peak strains were also compared for the same two floorbeam locations in Figures 6.7 and 6.8. Data is only shown for two models and two trains for clarity. It was observed from these figures that the simulated peak strains for Model 3 and 4 for FB7 and Model 3 for FB1 are conservative. Model 4 comes very close to the measured strains for FB1 midspan, particularly under the passenger cars. Similar to the girders, the simulated strains for the Rail Runner trains are significantly larger than the measured strains for the response under the locomotives than for the response under the passenger cars. For FB7, it is clear that Model 1 tends to overestimate the measured strains slightly more than for Model 3.

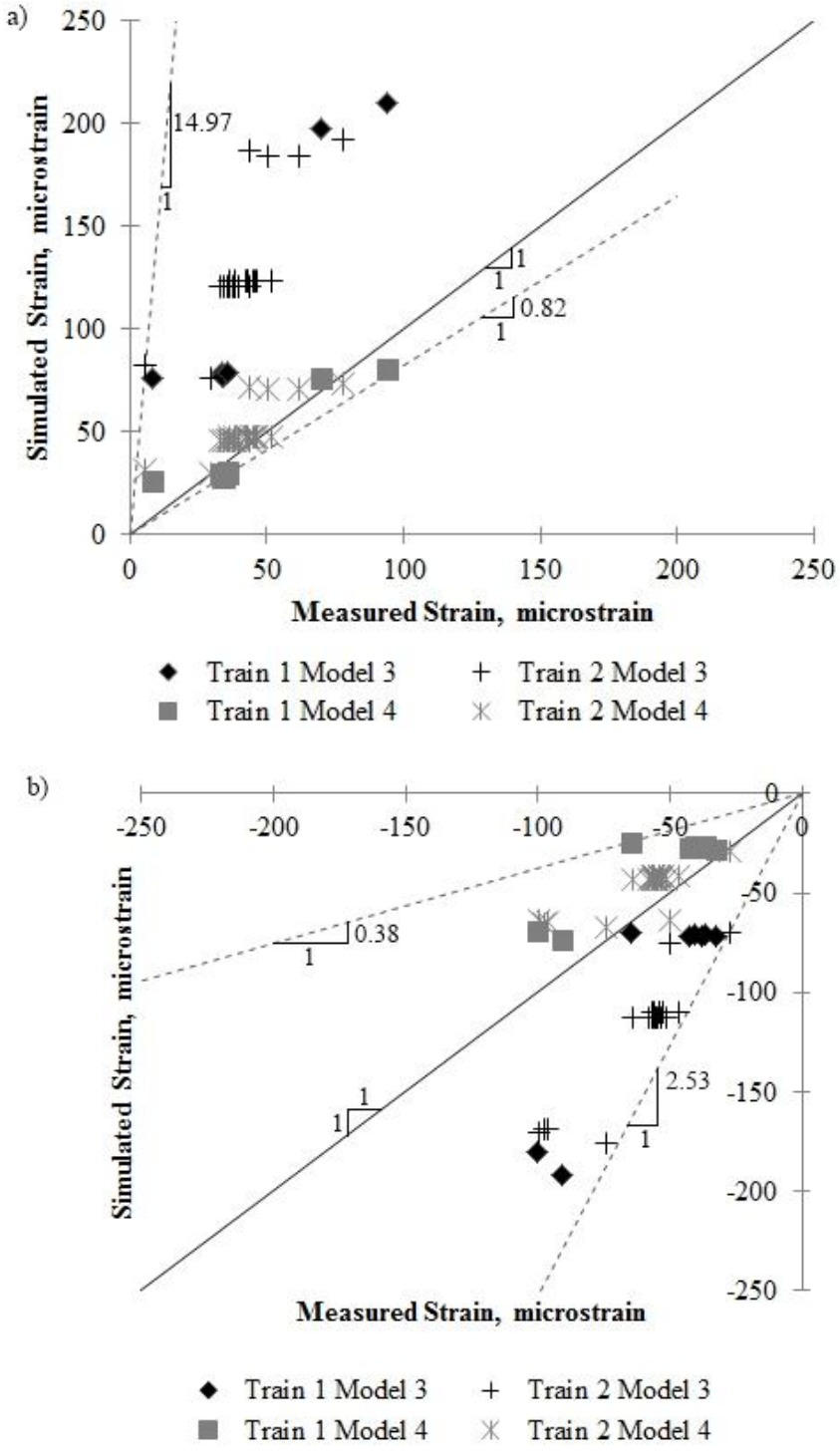

Figure 6.7: Peak measured vs. simulated strains for Trains 1 and 2 at FB1 midpoint a) bottom flange and b) top flange.

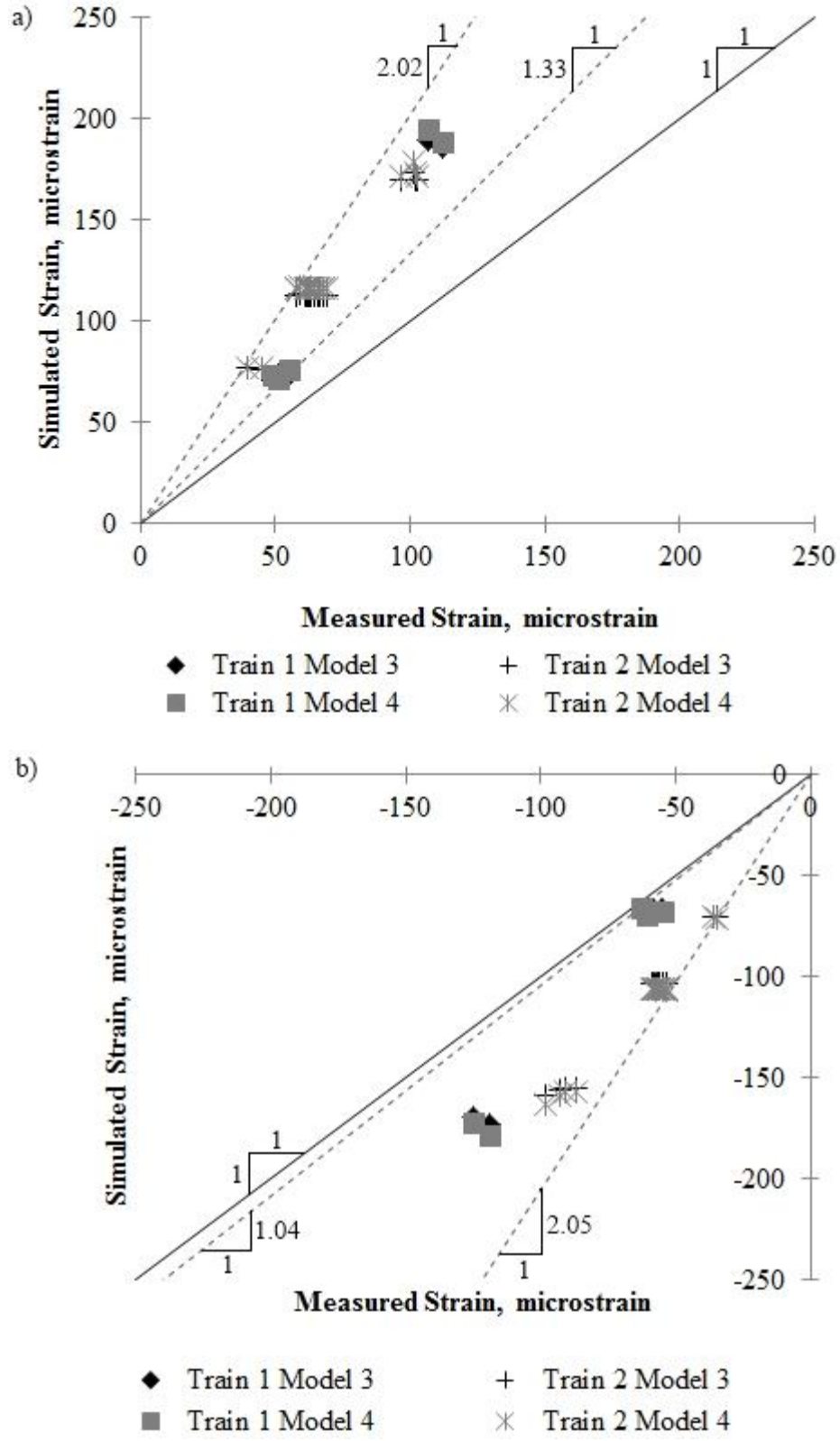

Figure 6.8: Peak measured vs. simulated strains for Trains 1 and 2 at FB7 midpoint a) bottom flange and b) top flange.

6.1.3 Stringers

Stringers S2 and S4 at Bay 6 midspans were chosen for comparison since these two stringers were instrumented on both the top and bottom flanges. Also, Model 3 gave different results for the interior (S2) and exterior (S4) stringers. As shown in Figures 6.9 and 6.10, there is a significant difference in the stringer response between Models 1 and 3. For S2, Model 3 simulates the measured strains very well, especially when compared to the results of Model 1, which overestimates the response under the locomotive at this location by over 100%. The difference is smaller for the passenger cars, but still significant. For stringer S4, Model 3 actually underestimates the measured strains for the tension flange, but there is good agreement for the compression flange.

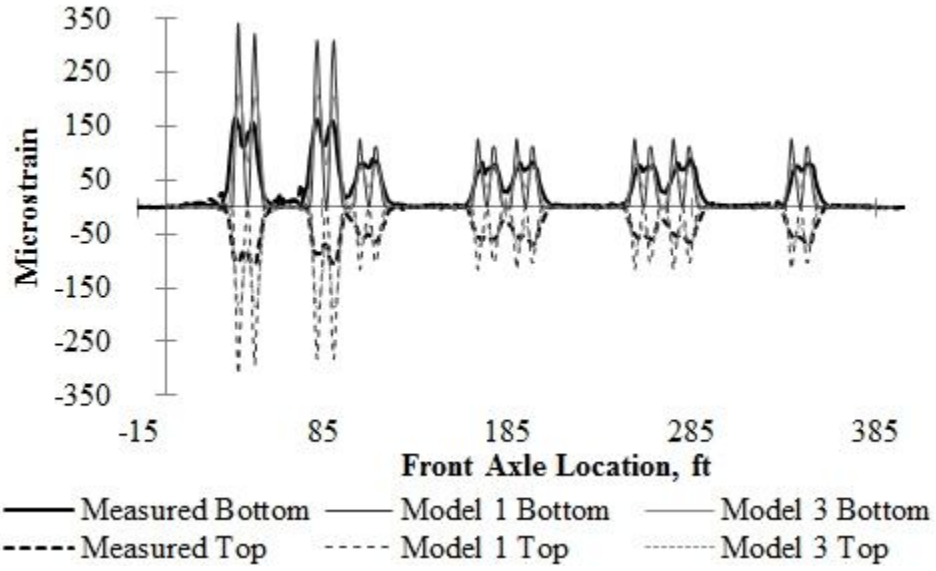

Figure 6.9: Measured vs. simulated strains for Train 1 at S2B6 midspan.

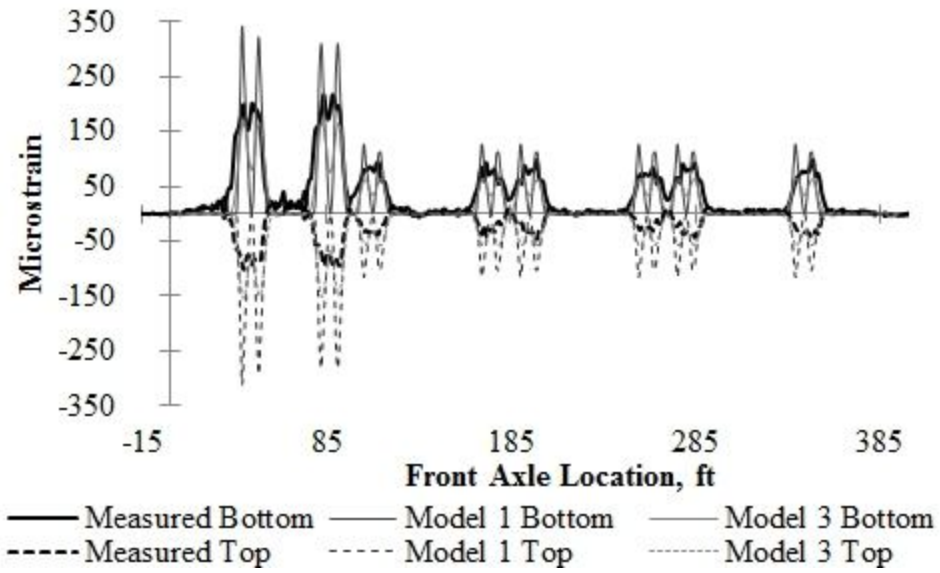

Figure 6.10: Measured vs. simulated strains for Train 1 at S4B6 midspan.

Another important comparison between the various models and the measured strain values is the shape of the curve. In Figures 6.9 and 6.10, the simulated strains for Model 1 rose abruptly from a value of zero to a peak (when the axle is directly at the stringer midspan) and back to zero when there were no axles on the stringer in that bay. For Model 3, there was still a significant dip in strain between the two axles of one pair of axles, but it did not reach a value of zero. This is a significant finding, particularly for a fatigue evaluation since the fatigue life of a structure is dependent on the range of the stress cycles, not just the peak magnitudes. Section 6.2 will compare the simulated and measured Miner's sums. The strain history from Model 4 (not shown) is similar to that of Model 3, but with lower magnitudes, thus further underestimating the strains in stringer S4.

The comparison of peak stringer strains (see Figures 6.11 through 6.12) shows that Model 3 is a much closer fit to the measured values than Model 1. One thing of note is that Model 3 underestimated the measured peak strains at the S4B6 midspan location, which could lead to an unconservative evaluation for strength or fatigue. To account for this, the maximum

simulated strain for all four of the stringers could be used along with a multiplier to account for the rocking effect. The comparison between the maximum simulated and measured response for S4 is shown in Figure 6.13. In this figure it is clear that this estimation is more appropriate for stringer S4, although it still slightly underestimates the actual strain. Another observation was that the locomotive weight appeared to have been overestimated when modeling the loads as found with the girders and floorbeams. The peak simulated strains for Model 3 were consistently smaller than those obtained using Model 1, which was expected from the load spreading effect of the ballast.

In general, the top flange behavior was similar to that of the bottom flange, but the simulated strains were far more conservative. For the Rail Runner trains, the simulated locomotive strains were further from the actual strains than for the passenger cars for both the top and bottom flanges. The locomotive and passenger car strains appeared to be estimated with similar accuracy for the Amtrak trains (Train 2).

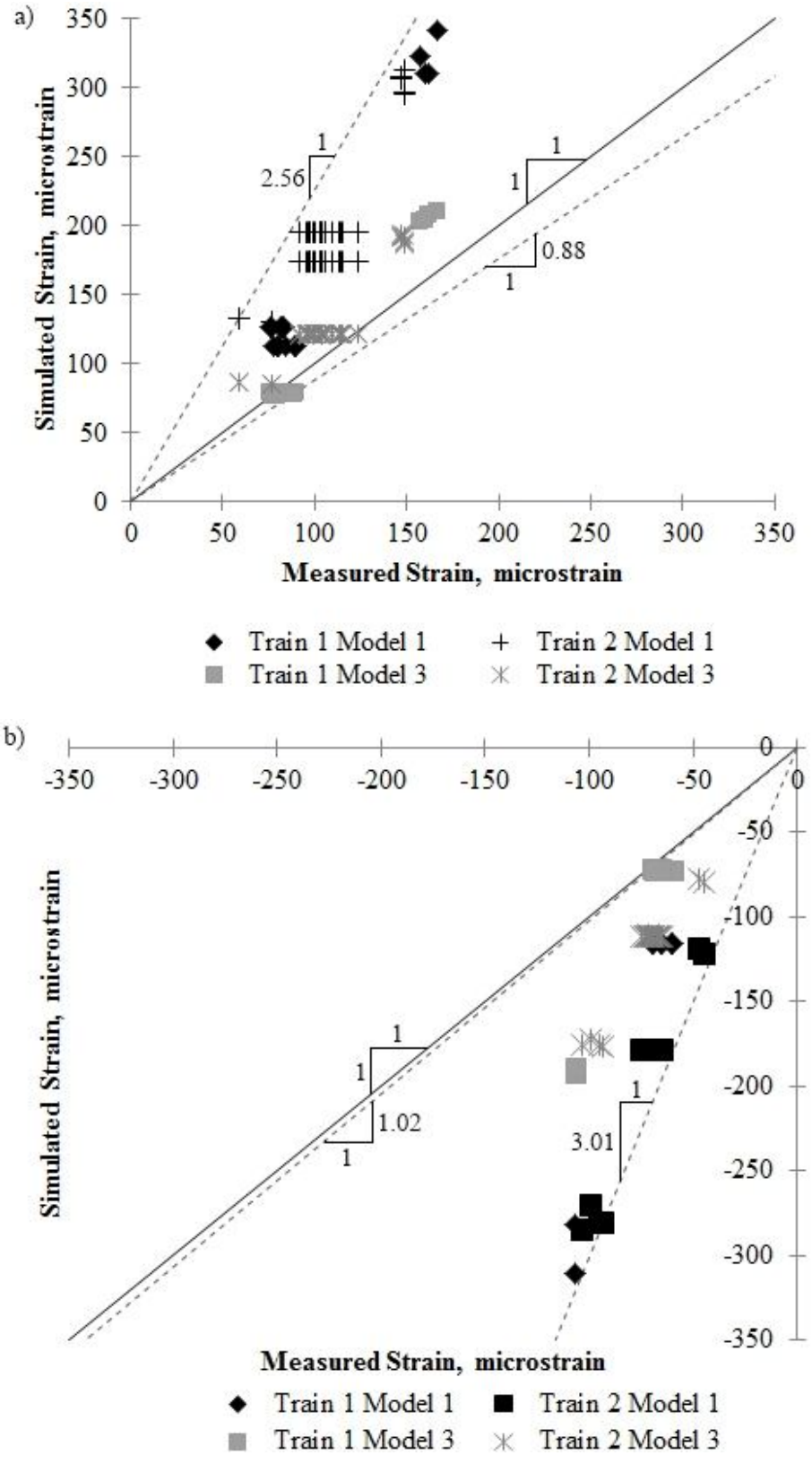

Figure 6.11: Peak measured vs. simulated strains for Trains 1 and 2 at S2B6 midspan a) bottom flange and b) top flange.

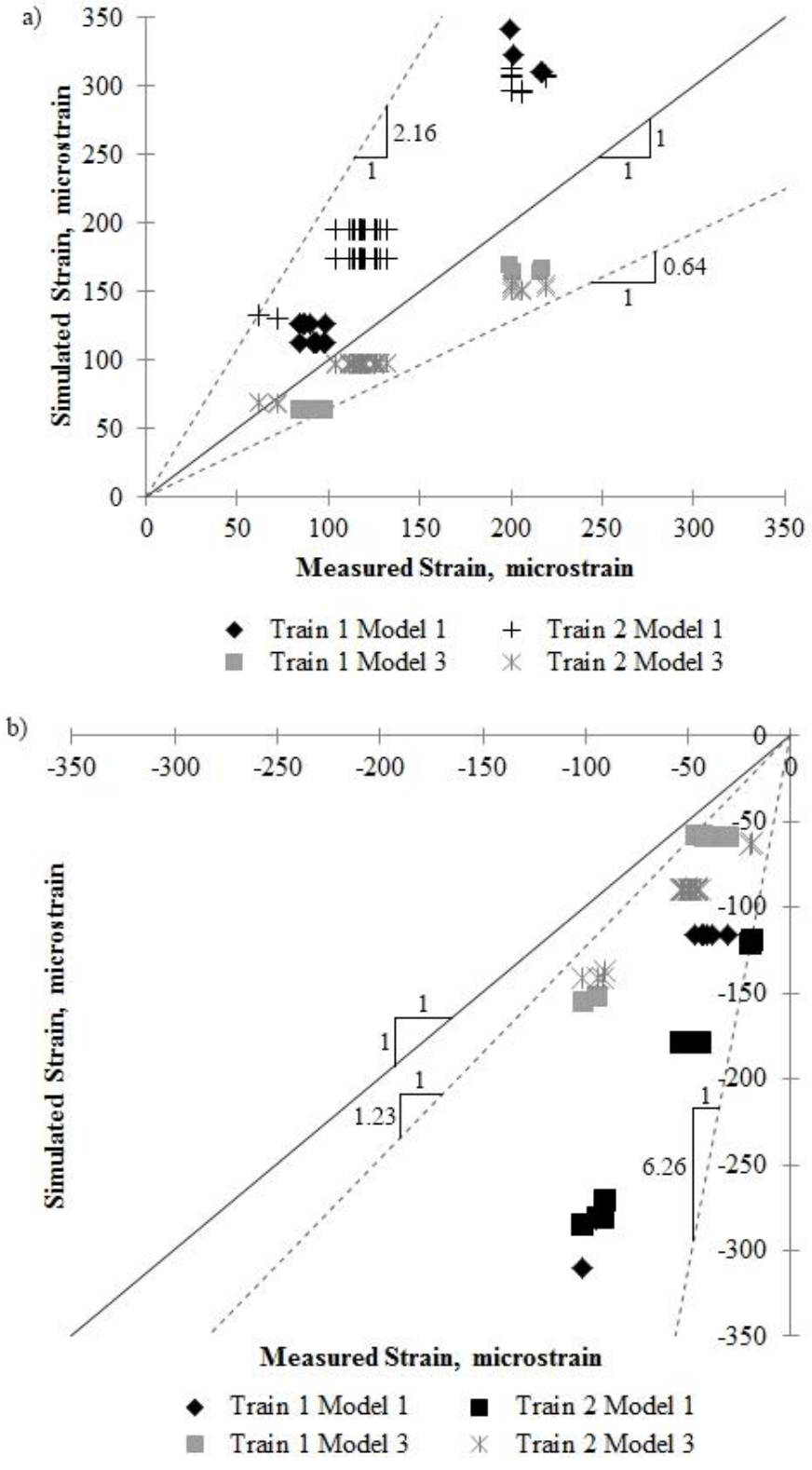

Figure 6.12: Peak measured vs. simulated strains for Trains 1 and 2 at S4B6 midspan a) bottom flange and b) top flange.

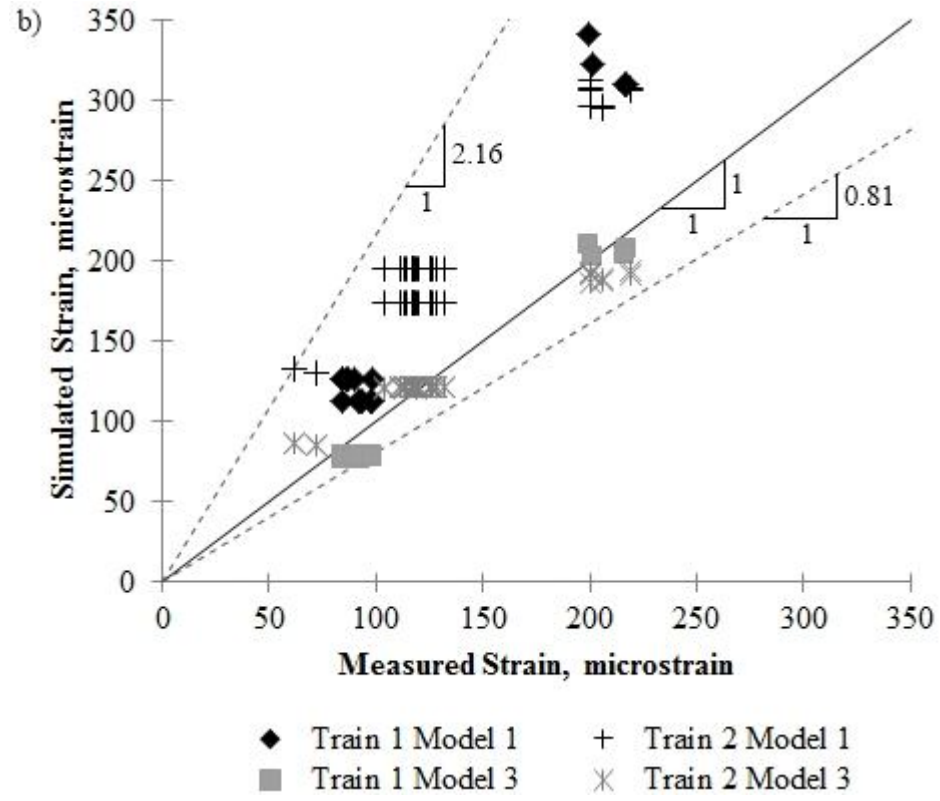

Figure 6.13: Bottom flange peak measured vs. simulated strains for Trains 1 and 2 at S4B6 midspan using maximum stringer strain for Model 3 (compare to Figure 6.12a).

6.1.4 Summary of Comparisons

It was found that the model that appears to best describe the behavior of this structure is Model 3, which accounts for the load distribution through the rails, ties, and ballast. The strain magnitudes were consistently smaller for stringers S1 through S3 and for the floorbeams and girders. For stringer S4, the peak magnitudes were underestimated by Model 3 since the actual structure showed the largest strains at stringer S4, while the model general produced smaller strains for the exterior stringers. If the simulated strains from the interior stringers were compared against the measured strains, the values agreed more closely. The simulated floorbeam and girder strains tend to be larger than the measured strains, even when using Model

3. It is interesting to note that the simulated strains for the girders were not affected by either the fixity of the floor system or the modeling of the ballast. The end floorbeam was affected by the end fixity, but not the ballast. The interior floorbeams were only slightly affected by the modeling of the ballast. The stringers were sensitive to both the end fixity of the floor system and the ballast modeling. Although Model 3 appears to be the best based on the observations made in this section, the most important quantity for a fatigue evaluation is the Miner's Sum, and therefore this was determined for all of the models for each train to ensure that the best model was chosen for evaluating fatigue.

6.2 Miner's Sum Comparison of Models

A model that yields accurate Miner's sums for critical details is very important when performing a fatigue evaluation. For this to occur, the model must accurately estimate both the shape and magnitude of the moment history curve. For this structure, Model 3 performed the best out of the four models as shown in the previous section. To validate this choice, the Miner's sum was determined using the measured strain histories from each of the load tests and the simulated histories from all four models. For the girders and floorbeams, the S-N curve corresponding to a category D detail will be used. Recall that the S-N curves describe the fatigue behavior of various types of details. The constant amplitude stress range, S, is plotted against the number of cycles that can be withstood. In the AREMA (2007) and AASHTO (2010) specifications, common details for bridges are grouped into categories of details that behave similarly under fatigue loading. These fatigue details range from details that have relatively high resistance to fatigue (i.e., category A) to those with relatively poor fatigue resistance (i.e., category E'). For the stringers, the S-N curve for category A should be used since the stringers are rolled sections without any holes or welds away from the ends.

To perform the Miner's sum calculations, all of the strain histories were first converted to stress histories and then evaluated using a rainflow counting algorithm. This was done using code provided on the MATLAB file exchange website by Adam Nieslony (2009). This code takes a stress history, reduces it to turning points (local maxima and minima), then determines the magnitude of each stress cycle. Each stress cycle is then classified as an entire cycle (tension and compression) or only a half-cycle (tension or compression). Once this data is compiled, it can be used to calculate a Miner's sum using the following equation:

$$D = \sum_{1}^{k} \frac{n_i}{N_i} = \sum_{1}^{k} \frac{n_i}{n_o} * \left(\frac{\Delta\sigma_i}{\Delta\sigma_o}\right)^3 \quad \text{EQ 6.1}$$

where D is the Miner's Sum, n_i is the number of stress cycles at the ith stress range magnitude, $\Delta\sigma_i$ is the ith stress range magnitude, n_o is the number of cycles at the knee point, $\Delta\sigma_o$ is the number of cycles at the knee point, and k is the number of stress cycles. For the riveted details, n_o is 6 million cycles and $\Delta\sigma_o$ is 7 ksi (48.2 MPa) (AREMA 2007). For the stringers away from the connections, n_o is 2 million cycles and $\Delta\sigma_o$ is 24 ksi (165 MPa) (AREMA 2007). To obtain the Miner's sum, first the strain histories were converted into stress histories. To do this, Hooke's law (EQ 5.2) was used. Each strain value was multiplied by the elastic modulus, which for steel is taken as 29,000 ksi (200 GPa). This process was repeated for each train for all four models and for the measured data at G1B3 midspan, G2B6 midspan, FB1 midspan, FB7 midspan, S2B6 midspan, and S4B6 midspan (see Table 6.2).

Table 6.2 shows that the difference between the Miner's sums based on the measured and simulated strains varies widely between models and between different locations for the same model. Although data is only shown for Trains 1 and 2, the trends and percent differences are consistent from train to train. In general, the pinned models are more conservative (higher

Miner's sum) than those with fixed connections, most notably for the stringers and end floorbeam locations. Models 3 and 4 tend to have lower Miner's sums than Models 1 and 2 for the stringers because of the load spreading and connection fixity effects, particularly for the stringers. Floorbeam FB1 appears to be the least accurately depicted by the models assuming pinned connections, particularly for Model 3. This can be explained by the fact that the load spreading cannot be fully considered at the end of the structure since the modeling of the track and ballast terminates at the end of the structure instead of continuing. Another source for this error is the fact that the end floorbeam may be able to develop some negative moment since there is more torsional rigidity at the girders at the supports than at the interior floorbeams.

Based on the Miner's Sums, it would appear that the end floorbeams may have end connections with some degree of partial fixity since the pinned model overestimates the strains and the fixed models underestimates the strains. In most cases, Model 3 gives the results that match the best with the measured data. At S4B6 midspan, Model 3 underestimates the measured strains significantly, however, if this model were used in an engineering analysis, the most critical stringer of the four would be used in the analysis. For Model 3, the critical stringer location is S2B6 midspan, where the simulated Miner's Sum is $334.2*10^{-9}$ for Train 1 and $1022*10^{-9}$ for Train 2, compared with the measured Miner's Sums from the critical S4B6 stringer which were $292.3*10^{-9}$ for Train 1 and $825.8*10^{-9}$ for Train 2. Thus, a conservative estimate for fatigue would still be achieved using this model. The Miner's Sums for the girders and interior floorbeam were very similar from model to model (with the exception of FB1). When there was a measureable difference between the Miner's Sums using the simulated data, Model 3 tends to be the closest to the measured values. For the critical (max Miner's Sum) girders, the models overestimated the Miner's Sum by 65% to 94%, and for the critical (max

Miner's Sum) floorbeams, the values are overestimated by 319% to 551%. Further modeling refinements would be required to create greater convergence between the models and reality.

Table 6.2: Comparison of Miner's Sums based on Measured and Simulated strains.

	Miner's Sums					% Difference from Measured			
Train 1	Measured (* 10-9)	Model 1 (* 10-9)	Model 2 (* 10-9)	Model 3 (* 10-9)	Model 4 (* 10-9)	Model 1	Model 2	Model 3	Model 4
G1B3 midspan	10.17	18.08	18.58	18.10	18.51	78%	83%	78%	82%
G2B6 midspan	19.86	32.77	33.55	32.87	33.45	65%	69%	66%	68%
FB1 midspan	33.14	429.4	21.80	407.9	23.67	1196%	-34%	1131%	-29%
FB7 midspan	43.03	209.4	193.0	180.4	208.7	387%	348%	319%	385%
S2B6 midspan	139.8	1823	915.0	334.2	213.3	1205%	555%	139%	53%
S4B6 midspan	292.3	1823	852.8	153.5	90.99	524%	192%	-47%	-69%
Train 2									
G1B3 midspan	19.73	36.94	36.65	36.14	36.37	87%	86%	83%	84%
G2B6 midspan	32.68	63.57	63.39	62.51	63.20	94%	94%	91%	93%
FB1 midspan	82.93	1218	64.96	1201	70.86	1369%	-22%	1349%	-15%
FB7 midspan	98.44	641.2	525.9	513.8	541.1	551%	434%	422%	450%
S2B6 midspan	416.1	5455	3218	1022	786.8	1211%	674%	146%	89%
S4B6 midspan	825.8	5455	2914	468.1	336.2	560%	253%	-43%	-59%

6.3 Summary

In this chapter, the four finite element models described in Chapter 5 were evaluated by comparing them with the measured data. Comparisons were made based on observations from full strain histories, comparisons of peak values, and comparisons of Miner's Sums. Overall, Model 3 appears to be the best model since it estimates the strains better than the other three at the critical locations, and therefore will be used in the fatigue evaluation in Chapter 7. For the stringers, the estimation is significantly unconservative for S4B6 midspan; however, this is in part because the model predicts higher loads in the interior stringers than in the exterior stringers. If the maximum simulated response for a stringer is compared against the maximum measured response, the comparison is more favorable. This is important to note since the engineering analysis uses the critical (max Miner's Sum) component to estimate fatigue life. For the

floorbeams and girders, the response is overestimated, which may be attributed to overestimating the train weights. Other factors may also contribute to the overestimated strains that further modeling may capture.

CHAPTER 7

Fatigue Analysis

As discussed in previous chapters, steel bridges have the potential to fail under fatigue loading. AREMA has set forth guidelines for determining the susceptibility of existing bridges to fatigue failure and for estimating the remaining fatigue life. In general, the structure is first reviewed to identify the critical details that are susceptible to fatigue failure. A relatively simple analysis is then performed using the design train load to determine if the structure has an infinite fatigue life. If not, the remaining life is determined based on the AREMA design train loading. Should the results from this basic analysis not be satisfactory, an advanced fatigue analysis may be performed using the estimated historical loading along with current and future loading. This chapter will discuss the train loads used in the fatigue evaluation of Bridge 880.37. Next the AREMA (2007) fatigue evaluation procedure will be discussed and applied for this structure. Finally, the remaining life of the structure will be estimated using the Miner's Sum.

7.1 Train Loads at Bridge 880.37

The train loading at Bridge 880.37 was estimated with the help of a senior bridge engineer in the railroad industry (Steven Dick, personal communication, October 19, 2010). Typical train configurations and frequencies were estimated for various time periods. From 1898 to 1990, freight trains regularly crossed this bridge. Passenger trains also made frequent trips (approximately 10 per day) through this area from 1898 through 1970. In 1970, Amtrak took over passenger rail operations and reduced the number of trains to 2 per day. Coal trains also crossed this structure from 1965 to 1990. From 1990 to 2008, the only regular traffic on this line was the Amtrak passenger trains. In late 2008, Rail Runner service commenced, thus increasing the use of this rail.

7.1.1 Historical Train Loads

For passenger trains, steam locomotives were primarily used before the construction of Bridge 880.37 in 1898 and until about 1945. Steam locomotives were used slightly longer for freight trains through 1950. Over time, the gross weight of the passenger trains has remained fairly consistent. Based on the modeled train configurations, the gross weight of passenger trains has changed no more than 13% from 1898 to present day. However, the weight of freight freight trains has increased consistently over time. From 1898 to 1920, the gross weight of the trains was estimated as 2789 tons (24.81 MN). During the last era in which Bridge 880.37 carried freight (1970 to 1990) the gross weight of these trains more than doubled to 6104 tons (54.3 MN). In addition to passenger and regular freight trains, coal trains crossed this bridge from 1965 to 1990 and had a gross weight of approximately 14,000 tons (124.55 MN). All of the assumed historical train configurations are described in the figures and tables that follow.

To clearly and succinctly illustrate the train configurations throughout the various eras, Table 7.1 summarizes all of the rail cars and diesel locomotives used in the analysis of Bridge 880.37. Figure 7.1 defines the variables used in the column headings of Table 7.1. All data in this table comes from the dissertation of Dick (2002) except for the Rail Runner locomotive (MP 36 PH-3C), which came directly from the manufacturers website (MotivePower, 2010). Figure 7.2 illustrates the properties of the steam locomotives that were used in this analysis and Table 7.2 lists the axle locations relative to the first axle. Finally, Table 7.3 describes the train configurations used in each of the eras.

Table 7.1: Rail Car and Diesel Locomotive Properties.

Designation	Unit type	LPFC[1] (ft)	TC[1] (ft)	NA[1]	AS[1] (ft)	GW[1] (kips)
	Diesel Locomotives[2]					
DL1	EMD F Series	50.00	30.00	4	9.00	248
DL2	EMD F40PH passenger	56.17	33.00	4	9.00	264
DL3	EMD SD7-SD35	60.71	35.00	6	6.79	384
DL4	EMD SD38-SD45	65.83	43.00	6	6.79	396
DL5	MP 36 PH-3C	68.00	42.83	4	9.00	290
	Freight Cars					
F1	General (yr 1900)	38.00	24.50	4	5.00	100
F2	General (yr 1918)	42.00	31.13	4	5.50	140
F3	General (yr 1939)	43.71	30.71	4	5.50	170
F4	General (yr 1979)	55.50	40.83	4	5.67	220
F5	Coal (1975)	53.08	40.50	4	5.83	263
	Heavyweight Passenger Cars					
HP1	RPO/Baggage/Express	64.10	44.75	4	8.00	100
HP2	RPO/Baggage/Express	74.81	54.75	6	5.50	120
HP3	Coach	82.48	57.38	6	5.50	160
HP4	Diner	84.33	59.50	6	5.50	190
HP5	Sleeper	82.38	57.38	6	5.50	160
HP6	Observation	82.31	55.75	6	5.50	160
	Lightweight Passenger Cars					
LP1	RPO	85.00	59.50	4	9.00	120
LP2	RPO/Baggage	85.00	59.50	4	9.00	120
LP3	Baggage/Express	85.00	59.50	4	9.00	120
LP4	Coach	85.00	59.50	4	9.00	140
LP5	Diner	85.00	59.50	4	9.00	150
LP6	Sleeper	85.00	59.50	4	9.00	150
LP7	Observation	85.00	59.50	4	9.00	140
LP8	Boxcar Express	64.33	44.75	4	5.83	170
	Amtrak					
A1	Coach	85.00	59.50	4	8.50	160
A2	Diner	85.00	59.50	4	8.50	170
A3	Sleeper	85.00	59.50	4	8.50	170
A4	Dome/Lounge	85.00	59.50	4	8.50	160
	Commuter					
RR1	Rail Runner	85.00	64.00	4	8.50	110

[1] Abbreviations are defined in Figure 7.1

[2] Steam Locomotives are included in Figure 7.2

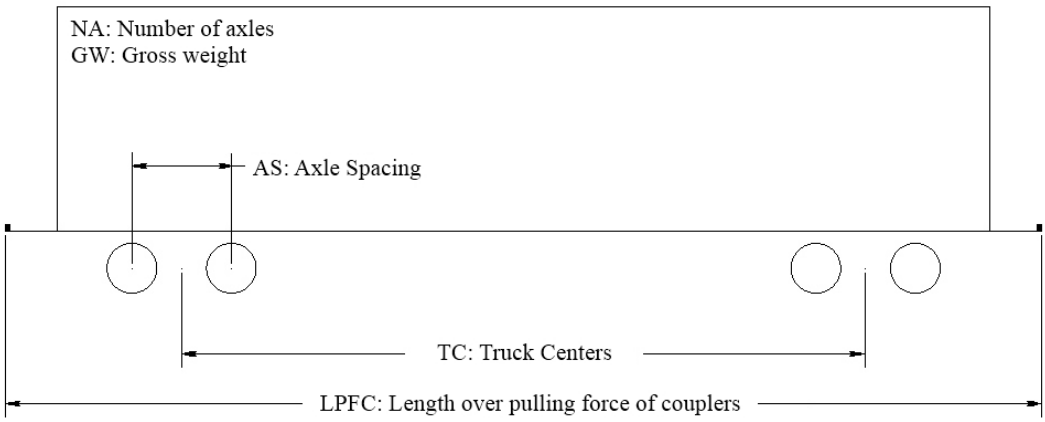

Figure 7.1: Definitions for abbreviations in column headings of Table 7.1.

Table 7.2: Steam engine axle locations.

	Distance from Front Axle (ft)				
Axle Number	SL1	SL2	SL3	SL4	SL5
1	0.00	0.00	0.00	0.00	0.00
2	6.67	6.83	7.03	9.08	9.08
3	11.42	11.50	13.05	14.08	14.58
4	18.25	17.50	21.00	18.96	20.08
5	25.08	23.50	27.08	23.83	25.58
6	35.08	29.50	34.07	28.83	31.08
7	46.38	39.50	43.04	35.83	41.08
8	50.55	51.86	48.07	45.25	54.28
9	54.71	56.03	63.03	49.42	59.03
10	62.98	60.20	69.05	53.58	63.78
11	67.15	72.64	75.07	61.85	83.28
12	71.32	76.80	85.06	66.02	88.03
13	-	80.97	91.08	70.19	92.78
14	-	-	98.02	-	-

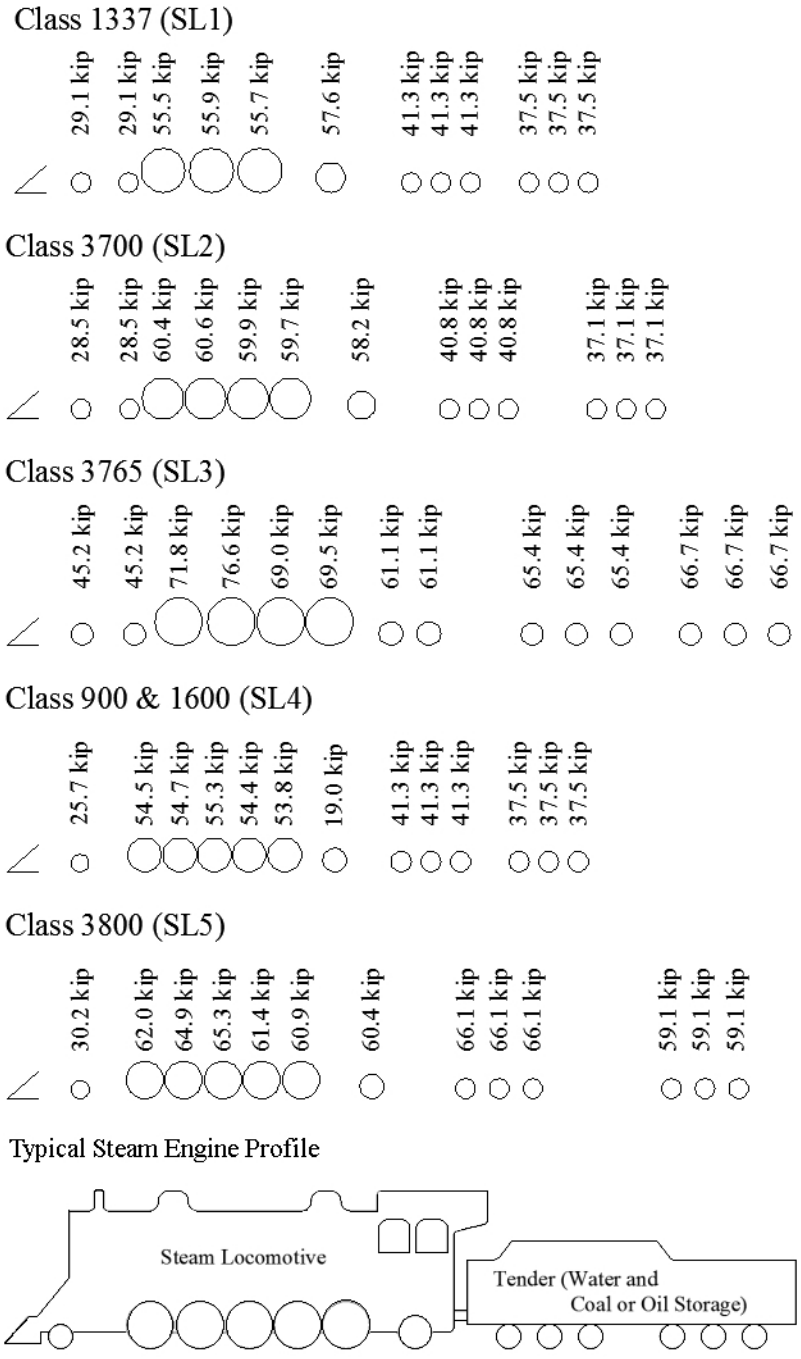

Figure 7.2: Axle weights for steam locomotives

Table 7.3: Train configurations.

Train Type	Trains per Week	Configuration of Each Train
Passenger Trains		
1898 to 1920	70	1 SL1, 1 HP1, 1 HP2, 4 HP3, 1 HP4, 3 HP5
1920 to 1935	70	1 SL2, 1 HP1, 1 HP2, 4 HP3, 1 HP4, 3 HP5
1935 to 1945	70	1 SL3, 1 HP1, 1 HP2, 4 HP3, 1 HP4, 3 HP5
1945 to 1970	70	4 DL1, 1 LP2, 1 LP3, 4 LP4, 1 LP5, 3 LP6
Amtrak (1970 - Present)	14	2 DL2, 1 LP3, 4 A2, 1 A3, 1 A5, 3 A4
Railrunner (2008 - Present)	92	1 DL5, 3 RR1
Freight Trains		
1898 to 1920	28	1 SL4, 50 F1
1920 to 1950	28	1 SL5, 50 F2
1950 to 1970	28	4 DL1, 50 F3
1970 to 1990	28	3 DL3, 50 F4
Coal Train		
1965 to 1990	3	5 DL4, 100 F5

7.1.2 Current Train Loads

Currently, only passenger rail crosses Bridge 880.37, two Amtrak and 16 Rail Runner trains per weekday. The train units in current use are described in Figure 4.10 and the train configurations observed during the load tests are described in Table 7.3. Based on the observed trains, it appears that a typical train configuration is no more than one engine and three passenger cars for the Rail Runner. The Amtrak train used in the load test appeared to have the configuration given in Table 7.2 for the passenger trains from 1970 to present. According to the Rail Runner schedule (New Mexico Rail Runner 2011), there are 16 trains (8 in each direction) that pass over this structure each day from Monday to Friday, 8 on Saturday, and 4 on Sunday. For the fatigue analyses, this schedule will be used starting in 2008 and for future estimates. By using this defined current and historic train loads, it was possible to perform the fatigue evaluation.

7.2 AREMA Fatigue Analysis

In the AREMA Specification (2007), provisions are given to determine if a fatigue analysis is necessary. If it is necessary, the analysis procedure begins simple and becomes increasingly detailed for structural elements that are potentially fatigue prone. AREMA (2007) states that if a structure has carried less than 5 million gross tons per year throughout its history, the structure does not need to be evaluated for fatigue, provided that there are no details worse than Category D. For Bridge 880.37, Table 7.4 gives the gross weight per year based on the trains given in Section 7.1 and using the eras as specified by Steven Dick (Steven Dick, personal communication, October 19, 2010). The data shows that for much of its history, Bridge 880.37 carried far more than 5 million tons of train traffic per year, and therefore is not exempt from a fatigue analysis.

Table 7.4: Gross weight of yearly train traffic by era

Era	Gross Tonnage (million tons per yr)
1898 to 1920	7.80
1920 to 1935	9.38
1935 to 1945	9.38
1945 to 1950	9.88
1950 to 1970	11.3
1970 to 1990	9.45
1990 to 2008	0.567
2008 to present	1.70

For riveted structures, if it can be verified that the connections are tight and have developed a normal level of clamping force, Fatigue Category C may be used, otherwise Fatigue Category D shall apply (AREMA 2007). In this case, no effort was made to evaluate the clamping force in the riveted connections; therefore, the connections and corresponding members were considered as Category D details.

At this point, the fatigue details of Bridge 880.37 were checked based on the infinite life criterion in AREMA (2007) Article 15.1.3.13. The first step in this check is to determine the number of cycles for analysis using AREMA (2007) Table 15-1-7. For this structure, the longitudinal flexural members (i.e., stringers and girders) are designed for more than 2,000,000 constant amplitude stress cycles since the lengths of the members are less than 100 ft (30.5 m). The floorbeams are also designed for more than 2,000,000 cycles since there is only one track on the structure (AREMA 2007).

The impact factor used for fatigue analysis varies over the life of this structure due to the changes in train usage. In all cases, the calculated dynamic impact is multiplied by 90% for ballast deck bridges since the ballast dampens the vertical impact (AREMA 2007). Steam engines require a larger dynamic impact on bridges because of periodic hammer blows. For these trains the vertical impact factor is calculated as follows (AREMA 2007):

$$For\ L\ less\ than\ 100\ ft\text{:}\ I_v = 60 - \frac{L^2}{500} \qquad \text{EQ 6.1 a}$$

$$For\ L\ equal\ to\ or\ greater\ than\ 100\ ft\text{:}\ I_v = 10 + \frac{1800}{L - 40} \qquad \text{EQ 6.1 b}$$

where I_v is the dynamic impact factor and L is the length of the member (in feet). For all rail cars and diesel locomotives, the vertical impact is smaller, and is calculated using the following equations (AREMA 2007):

$$For\ L\ less\ than\ 100\ ft\text{:}\ I_v = 40 - \frac{3L^2}{1600} \qquad \text{EQ 7.2 a}$$

$$For\ L\ equal\ to\ or\ greater\ than\ 100\ ft\text{:}\ I_v = 16 + \frac{600}{L - 30} \qquad \text{EQ 7.2 b}$$

A separate impact factor is also applied to account for the train rocking from side to side, which is simply added to the vertical impact factor. This factor is determined by applying 20%

of the wheel load on each rail, and calculating the effect on the supporting members. For the stringers, this is performed by modeling the deck as a continuous beam over the 4 stringers where each of the stringers is supported in the vertical direction. When considering two members supporting one set of rails symmetrically, the rocking effect is simply (5/S)*20% where S is the member spacing. For both the dynamic impact and rocking effect, the values for the floorbeams are equal to those calculated for the supporting members (e.g., the girders in this case) (AREMA 2007). This factor is 3.26% for the girders and floorbeams, 7.6% for interior stringers, and 4.3% for exterior stringers. For traffic that is not classified as light rail or commuter rail, the dynamic impact factor is reduced to 35% of the design value for fatigue analysis (AREMA 2007). Prior to 2008, when Rail Runner service began in northern New Mexico, this reduction in dynamic impact applies. From 2008 to present, the dynamic impact must be taken as 100% of the calculated values for the Rail Runner trains, since these trains provide commuter rail service. The resulting dynamic impact factors used in this fatigue analysis are as follows:

Table 7.5: Dynamic impact factors for Bridge 880.37

Member Type	Steam Locomotives	Diesel Locomotives and Freight and Passenger Cars	Commuter Trains
Girders & Floorbeams	16.8%	9.22%	26.3%
Interior Stringers	21.5%	15.2%	43.5%
Exterior Stringers	20.4%	14.1%	40.2%

These dynamic impact factors were applied to the live load stresses caused by the E80 train and alternative live load to check for infinite life.

It was shown in Chapter 4 that there is no evidence of significant flexure at the end of the stringers and floorbeams for Bridge 880.37; therefore, the fatigue analysis is limited to the bottom flanges at midspan of each member type (i.e., stringer, floorbeam, and girder). The

maximum live load stress ranges (algebraic difference between the maximum and minimum calculated stresses) was determined for each member type at midspan using the E80 and alternative loading. For the stringers, the maximum stress range is caused by the alternative live load and is 12.8 ksi (88.4 MPa). For the girders, it is 9.63 ksi (66.4 MPa) and controlled by the E80 loading. For the floorbeams the maximum stress range is caused by the alternative live load and is 13.5 ksi (93.4 MPa). All of the stress ranges above were determined using the appropriate dynamic impact factor (see Table 7.5) for non-commuter trains and Model 3 as described in Chapter 5. For a riveted detail, the maximum allowable stress range for infinite fatigue life under variable amplitude loading is 6.0 ksi (41.4 MPa), which is exceeded by the calculated stress ranges caused by the standard loading for the floorbeams and girders. Therefore, the remaining fatigue life must be determined for these details. The stringers do not need to be considered any further, however, since the constant amplitude fatigue limit (CAFL) for a category A detail is 24.0 ksi (165.5) and the maximum calculated stress is 12.8 ksi (88.4 MPa).

To determine the adequacy of the structure for fatigue, the effective stress range is determined as follows (AREMA 2007):

$$S_{R,eff} = \alpha \left(\sum \gamma_i * S_{Ri}^3 \right)^{1/3} = \alpha \left(\sum \frac{n_i}{N} * S_{Ri}^3 \right)^{1/3} \quad \text{EQ 7.3}$$

where $S_{R,eff}$ is the effective stress range; S_{Ri} is the i^{th} stress range magnitude; α is a constant which is taken as 1.0 (unless experimental fatigue test results indicate otherwise); γ_i is the ratio of the number of occurrences of S_{Ri} to the total number of stress cycles, (N); and n_i is the number of repetitions of S_{Ri} (AREMA 2007). To obtain the stress range magnitudes, the estimated historical train loads were applied to the structural model (i.e., Model 3) to generate stress histories. Rainflow counting was then utilized to obtain the number of cycles at each stress range level for each of the trains.

To obtain the effective stress ranges using the simulated data, MATLAB (Mathworks 2010) was used along with the code written by Adam Nieslony (2009). Recall the MATLAB code that was previously used in Chapter 6 to obtain the Miner's Sums and compare the four bridge models with the measured data. Stress histories for each of the trains described in Sections 7.1.1 and 7.1.2 were determined using the following equation:

$$Stress\ History = \frac{[IL] * [L]}{S} \quad \text{EQ 7.4}$$

where $[IL]$ is the influence line row vector and $[L]$ is the loading matrix as described in Chapter 5, and S is the section modulus at the location of interest. For both the girder and floorbeam, the bottom of the section is critical since for the girder, the cover plates are riveted, and for the floorbeam, rivets pass through the bottom flanges at midspans of half of the floorbeams to connect the cross bracing. In this analysis, FB7 is used even though there are no rivets passing through the bottom flange at this location. Use of this model is still valid, however, since the stresses are expected to be the same for all interior floorbeams. The stress histories were then analyzed using the rainflow algorithm, which reduced the stress histories to turning points (local maxima and minima) for the rainflow counting. The output of the rainflow counting algorithm is a 3 x n matrix, where n is the number of stress histories extracted. The first row of this matrix gives the stress amplitude (S_{Ri}), which must be doubled to obtain the stress ranges. The second row gives the mean stress of the stress range and the third row indicates n_i for each stress cycle, which is 0.5 for a half cycle (tension only or compression only) or 1.0 for a full cycle (tension and compression).

Once this matrix was obtained for each of the historical trains, a spreadsheet was setup to calculate the effective stress range for the simulated train traffic. In this spreadsheet, the stress ranges and corresponding n_i values were tabulated for each train. The number of occurrences for

each train was entered at the top of each n_i column. Thus, the number of cycles attributed to each train type was simply the product of the number of trains and the sum of the n_i column. The value of N was then determined as the sum of the number of cycles attributed to each train type. Another table is then created where the $(n_i/N)*S^3_{Ri}$ values were calculated for each stress cycle. These values were then summed for each train and the value for each train was multiplied by the number of occurrences of that train. Finally, the effective stress range was determined by taking the cube root of the sum of the $\sum\left(\frac{n_i}{N} * S^3_{Ri}\right)$ terms for all of the historical trains.

According to the AREMA Specification (2007), all stress ranges shall be removed that cause the calculated effective stress range to fall below the variable amplitude fatigue limit of 6.0 ksi (41.4 MPa). This was done by removing all stress ranges below a certain magnitude, checking the new effective stress range and repeating until the effective stress range is at least 6.0 ksi (41.4 MPa). For the girders, the stress ranges below 2.34 ksi (16.1 MPa) were removed and for the floorbeam, the stress ranges below 5.0 ksi (34.5 MPa) were removed in order to cause the effective stress to exceed the 6.0 ksi (41.4 MPa) threshold. The following tables show the calculations performed for the girder and a floorbeam at midspan. Table 7.6 show the calculations for determining N.

Table 7.6: Total number of trains crossing Bridge 880.37 and stress cycles (*N*).

Train	Trains per day	# of years in service	Number of Trains	Σn_i per train: Girders	Σn_i per train: Floorbeams	Σn_i for train type: Girders (*10^6)	Σn_i for train type: Floorbeams (*10^6)
Passenger							
1898-1920	10	22	80300	4	10	0.321	0.803
1920-1935	10	15	54750	5	10	0.274	0.548
1935-1945	10	10	36500	4	11	0.146	0.402
1945-1970	10	25	91250	1	5	0.091	0.456
Amtrak (1970-2012)	2	42	30660	1	3	0.031	0.092
Rail Runner (2008-2012)	13.14	4	19184	1	2	0.019	0.038
Freight							
1898-1920	4	22	32120	1	2	0.032	0.064
1920-1950	4	30	43800	1	3	0.438	0.131
1950-1970	4	20	29200	1	55	0.029	1.606
1970-1990	4	20	29200	1	56	0.029	1.635
Coal (1965-1990) (3/wk)	0.43	25	3924	4	106	0.016	0.416
					N =	1.03	6.19

Comparing these tables, there are about 6 times as many stress cycles for the floorbeams than for the girders after the data is adjusted to ensure that the effective stress range is greater than 6.0 ksi (41.4 MPa). This is logical since the stress ranges between axles are much larger for the floorbeams than for the girders. Tables 7.7 and 7.8 show the calculations for determining the $\sum \left(\frac{n_i}{N} * S_{R,i}^3\right)$ terms for the girder and floorbeam locations, respectively.

Table 7.7: Calculations for obtaining $\sum\left(\frac{n_i}{N} * S_{R,i}^3\right)$ terms to determine the effective stress range.

Train	Number of Trains	$\Sigma((n_i/N)*S^3_{R,i})$ per train		$\Sigma((n_i/N)*S^3_{R,i})$ for train type	
		Girder ($*10^{-6}$ ksi^3)	Floorbeam ($*10^{-6}$ ksi^3)	Girder (ksi^3)	Floorbeam (ksi^3)
Passenger					
1898-1920	80300	519.7	308.7	41.7	24.8
1920-1935	54750	621.5	327.8	34.0	17.9
1935-1945	36500	1058	419.9	38.6	15.3
1945-1970	91250	177.9	105.2	16.2	9.60
Amtrak (1970-2012)	30660	162.0	80.69	4.97	2.47
Rail Runner (2008-2012)	19184.4	122.8	109.4	2.36	2.10
Freight					
1898-1920	32120	593.9	129.9	19.1	4.17
1920-1950	43800	882.2	377.2	38.6	16.5
1950-1970	29200	177.9	1215	5.20	35.5
1970-1990	29200	1332	2414	38.9	70.5
Coal (1965-1990) (3/wk)	3923.75	1441	8921	5.65	35.0
			Sum =	245	234

The trains that have the highest stress ranges are the coal train and the freight train used between 1970 and 1990. The trains that had the smallest impact on the effective stress range are the Rail Runner and Amtrak, which are the lightest and shortest trains amongst those used in this analysis. From the values given in Table 7.7, the effective stress ranges at each location amount to the following:

$$S_{R,eff,Girder} = \sqrt[3]{\sum \frac{n_i}{N} * S_{R,i}^3} = \sqrt[3]{245.39 ksi^3} = 6.26 ksi \quad \text{EQ 7.5}$$

$$S_{R,eff,Floorbeam} = \sqrt[3]{\sum \frac{n_i}{N} * S_{R,i}^3} = \sqrt[3]{233.90 ksi^3} = 6.16 ksi \quad \text{EQ 7.6}$$

Once the effective stress ranges were known, the expended portion of the useable life of the structure was estimated using the Miner's Sum. Equation 6.1 can be used to calculate the Miner's Sum, where n_o and $\Delta\sigma_o$ are 6 million and 7 ksi, respectively. The Miner's Sums for the girder and floorbeam are calculated as follows:

$$D_{Girder} = \sum_{1}^{1} \frac{1{,}032{,}000}{6{,}000{,}000} * \left(\frac{6.26ksi}{7.0ksi}\right)^3 = 0.123 \quad \text{EQ 7.5}$$

$$D_{Floorbeam} = \sum_{1}^{1} \frac{6{,}190{,}000}{6{,}000{,}000} * \left(\frac{6.16ksi}{7.0ksi}\right)^3 = 0.704 \quad \text{EQ 7.6}$$

According to the Miner's Sum for the floorbeam, fatigue could become an issue in the relatively near future. If it were assumed that the damage continues to accumulate at the same average rate as it has over the past 114 years, the Miner's Sum would reach unity around the year 2060. In reality, only the Amtrak and Rail Runner service uses this structure, and therefore damage will accumulate much more slowly. The method used to obtain the effective stress range is not well suited for estimating the remaining life of the structure, since changes in the loading cannot easily be incorporated for forecasting. To evaluate the remaining life of the structure with future loading that is different than the historical loading using the effective stress method, the effective stress range and corresponding *N* would need to be determined at points in the future, and the Miner's Sum checked until a point is determined where the fatigue life has been exhausted. This is much simpler to evaluate using the Miner's Sum directly since the Miner's Sum for each train can be determined, and projections can be made using the known Miner's Sums. Another consideration is that the model used in this analysis significantly overestimates the stresses at the floorbeam and the impact and rocking effect are added as per the AREMA Specification, thus making this evaluation even more conservative. If fatigue were an imminent problem for this structure, more work could be done to ensure that the model more closely matches the measured strains and therefore reduce the estimated fatigue damage.

7.3 Remaining Fatigue Life using Miner's Rule

To estimate the remaining fatigue life for Bridge 880.37, the Miner's Sums determined in Section 7.2 may be used since the sums were computed by removing all stress ranges that cause

the effective stress range to drop below 6.0 ksi (41.4 MPa) as specified in AREMA (2007). Since the historical Miner's Sums are known, only the Miner's Sums for the current traffic is required. To obtain this, the stress histories for the girder and floorbeam were evaluated using the rainflow algorithm described in Section 6.2, then applying Equation 6.1. Once the Miner's Sums for each of the trains is determined, each is multiplied by the number of trains of each type per year. The remaining Miner's Sum to failure is then divided by the yearly Miner's Sum accumulating as a result of the Amtrak and Rail Runner trains. These calculations are illustrated in Table 7.8.

Table 7.8: Calculations to estimate the remaining fatigue life.

	Miner's Sums			Trains Per Year		Current Annual Miner's Sum	Remaining Life (yrs)
	As of 2012	Amtrak (per train)	Rail Runner (Per Train)	Amtrak	Rail Runner		
Girder	0.123	1.04E-07	6.60E-08	730	6205	4.86E-04	**1806**
Floorbeam	0.704	6.10E-07	3.63E-07	730	6205	2.70E-03	**110**

Table 7.9 shows that Bridge 880.37 has significant remaining life, assuming that train traffic remains relatively light. The critical member for fatigue is the floorbeam at midspan, with a remaining life of 110 years. The girder appears to be very unlikely to suffer a fatigue failure since using even a conservative bridge model, the estimated remaining life is over 1800 years.

7.4 Summary

In this chapter, the trains used in the fatigue analysis for Bridge 880.37 were presented. One train configuration was taken to be representative of all trains during the era to which it pertains. Passenger trains have crossed this structure throughout its history and freight trains traveled this line from 1898 to 1990. Rail Runner commuter service began in 2008 and is anticipated to continue indefinitely. The configuration of each of these trains, including axle locations and weight, are all provided in Section 7.1. The fatigue evaluation process in the AREMA Specification (2007) was followed in Section 7.2 and the effective stress range and

associated number of cycles was ultimately calculated. It was found that this structure should not be expected to demonstrate fatigue related problems in the near future. The remaining life of the structure was estimated in Section 7.3 using the Miner's Sums of the current traffic. This structure can be expected to continue service for over 100 years based on Model 3. The actual remaining life of this structure is likely much longer since Model 3 was shown to be significantly conservative in Section 6.2.

THIS PAGE INTENTIONALLY LEFT BLANK

Chapter 8

Conclusions and Recommendations

8.1 Conclusions

8.1.1 Literature Review

Articles concerning Structural Health Monitoring (SHM) and fatigue of steel railroad and highway bridges were reviewed. It was found that extensive research has been done in the area of SHM for bridges. The typical approach was the use of acceleration readings to perform structural identification. Structural identification is the process of determining the dynamic structural properties, such as the mode shapes and natural frequencies, from measured accelerations. Once a set of measured dynamic properties is determined, damage detection can be performed through comparison with a simulated baseline or previous measurements. Many methods have been studied for this purpose; however, outside of the laboratory, the performance of most of these methods is poor. Some reasons for the inability to reliably detect damage include the effect of temperature fluctuations and the variability of traffic loading on the dynamic properties, which are difficult to fully account for. Another reason is that, when a significant number of sensors are used throughout the structure, the systems are essentially taking global measurements which are not well suited for detecting local damage.

Many dynamic SHM systems are designed to continuously take measurements, which lead to large quantities of data. Since many of these systems were designed to transmit data remotely to a website for real-time management, the volume of data gathered is potentially problematic. Either the data must be processed on-site using a dedicated computer before transmittal, or a method of transmittal must be used that is capable of continuously transmitting at a rate greater than the rate at which the data is acquired.

There were only a few articles outlining SHM systems utilizing strain measurements. Three types of strain-based SHM systems were found. The first type continuously evaluated the neutral axis depth and the load distribution factor for each of the instrumented members. These member properties could then be compared to baseline values for purposes of SHM. The second type of system measured strain and pressure hourly at various locations. The data was then analyzed using a signal processing algorithm that was designed to detect changes that could be related to structural damage. The third type of strain-based SHM system was one that periodically estimated the remaining fatigue life of a steel structure. One major drawback to the first and third strain-based methods was that strain transducers have a tendency to experience random and temperature-induced drift, which must be either corrected in the data processing or eliminated by "zeroing" the readings before measurements are taken. The most promising of the strain-based SHM systems was the one that periodically updates a fatigue model. The price for this type of system can be relatively inexpensive since the same system can be installed only when measurements are needed and subsequently removed and installed on another structure. Another advantage of this method is that it gives an estimate of when the steel members of the structure may require repair or replacement, as opposed to attempting to detect damage after it happens as is the case with methods that utilize acceleration measurements and the other two strain-based methods.

Methods for evaluating fatigue were also researched. There are two common methods for fatigue evaluation; the first uses fracture mechanics and the second uses an S-N chart based on full-size fatigue test results. The fracture mechanics approach typically involves the equation developed by Paris (1961), which relates the rate of crack growth to the stress intensity factor range and two constants (see Equation 2.5). The stress intensity range is also needed, which

requires detailed knowledge about the detail being studied, including an assumed initial crack size. Once the two constants and the stress intensity factor range are determined, the number of constant amplitude cycles to failure can be determined. This information can then be used to determine the remaining life of a detail.

The S-N method tends to be simpler to apply. To use this method, the detail type is determined based on the S-N curve from AASHTO (2010) or AREMA (2007). Once the detail type is determined, the appropriate S-N curve can then be chosen. There are two ways in which the S-N curve can be used. The first is to check if the detail is near the end of its fatigue life using the effective stress range. To do this, a stress history is required which can be taken from measured values or simulated. The stress history is then evaluated using a rainflow counting algorithm, which extracts the number of cycles at each stress range magnitude. The root mean cube of these stress ranges, which is the effective stress range, with the associated number of cycles can then be determined. The effective stress range and number of cycles can then be plotted on the appropriate S-N curve. If the point is below the S-N curve, the detail still has remaining life. To determine the remaining life, Miner's sum can be utilized (see Equation 2.1) by assuming that the effective stress range is representative of future traffic, in which case the remaining life is simply equal to: (number of years in service to date) * (Miner's sum at failure) / (Miner's sum to date). Otherwise, the future traffic can be estimated, a Miner's sum per unit of time can be calculated and the remaining life can be estimated as: (Miner's sum at failure – the Miner's sum to date) / (current Miner's sum per unit of time). Alternatively, the historic Miner's Sum can be calculated directly from the measured or simulated stress histories and a rate of fatigue damage can be estimated based on projected traffic.

As a result of this literature review, the topic of this research was SHM based on strain measurements. Strain measurements were used to validate a finite-element model, which was used to simulate stresses under historical and projected future traffic. The stresses were then evaluated using an S-N curve method based on AREMA (2007).

8.1.2 Load Testing

For Bridge 880.37, load testing was performed under regularly scheduled passenger rail traffic at full speed consisting of five Rail Runner trains and one Amtrak train. The test set-up included 36 strain transducers distributed on the stringers, floorbeams, and girders throughout the northern half of the bridge. Most of the gauges were placed in locations of high strain (at or near the midspan locations of the instrumented members) to reduce the effect of signal noise and to capture the maximum response of the members. Some gauges were placed at the ends of selected floorbeams and stringers to detect any negative flexure developing near the connections that would indicate end-fixity.

Once the load tests were completed, the measured strains were analyzed. It was found that the gauges near the member ends did not indicate significant end-fixity. It was also observed that the end floorbeam had lower strain measurements than the interior floorbeams, which was expected since the influence area of the end floorbeam is smaller than that of the interior floorbeams. The stringer strains demonstrated an asymmetric response (with respect to the longitudinal center line) under the locomotives as evidenced by increasing strains from stringer S1 to stringer S4 under the locomotives. This may be explained by a low spot in the ballast on the side of stringer S4, the effect of the engine's torque on the locomotive, or an asymmetric transverse load distribution of the locomotive itself. It was also observed that the stringers develop axial tension under live load. This effect is most significant in Bay 5, where

both flanges of the stringers were in tension near the end under live load and the neutral axis location was relatively high at the midspan locations. In Bay 6, this effect was smaller, but still present. The interior floorbeam strains appeared to behave as expected. The girder strains were also as expected, except the asymmetric response that was observed in the stringers was not observed in the girders.

Overall it appeared that the data from the load tests were reasonable and could be used to determine the finite-element model that best simulates the response of the structure under live loads. Some unexpected results were observed, such as axial tension in the stringers, and asymmetric behavior of the stringers but this behavior can be explained.

8.1.3 Model Creation

To evaluate a structure based on a simulated response, an accurate model is required. For Bridge 880.37, four finite-element models were created in an attempt to accurately simulate the strains in the members of the floor system. All four of the models consisted of frame elements representing the girders, floorbeams, and stringers, all placed on the same plane. Models 1 and 2 were different in relation to the end restraint of the floor system members (pinned vs. fixed, respectively). It was found that both these models tended to overestimate the strains in the structure and the shapes of the simulated strain histories did not agree well with the measured strain histories for the stringers and floorbeams, so two more models were created (i.e., Models 3 and 4). These models incorporated elastic springs to represent the crushed stone ballast, and frame elements to represent the rails and ties of the track. These models caused the load to be distributed longitudinally, which significantly decreased the simulated strains in the stringers. This modification had only a small effect on the floorbeam response, improving the shapes of the strain histories slightly, and almost no effect on the girders. The shape of the strain histories was

closer to the measured strains using Models 3 and 4 than with Models 1 and 2. Between Models 3 and 4, Model 3 tended to more closely simulate the strain magnitudes without underestimating the strain. For the stringers, Models 3 and 4 resulted in higher strains for the interior stringers than for the exterior ones, and since the stringer with the highest strain was actually stringer S4 (an exterior stringer), the simulated values were significantly un-conservative. When using the maximum simulated stringer response, which would be the case in a typical engineering analysis, the model is much closer to the measured values. For the interior floorbeams, the strains are significantly overestimated by all four models. For the end floorbeam, the strains are significantly overestimated by Models 1 and 3, and underestimated by Models 2 and 4. This was because of the fixity of the bearings in the model. For the girders, the strains under the locomotive are overestimated while the strains under the passenger cars matched well. Based on comparisons of the strain histories and peak strains, Model 3 is the best of the four models. These observations were confirmed when the Miner's sums under each of the load test trains for the measured strains were compared to those for all four models. Therefore, Model 3 was used for the fatigue evaluation of Bridge 880.37.

8.1.4 Fatigue Evaluation

Once the model was chosen, the fatigue evaluation was completed. To perform the fatigue evaluation, the procedure in AREMA (2007) was followed. This procedure begins with a check to determine if a fatigue evaluation is required. Over the service life, if the bridge carried more than 5 million gross tons of rail traffic per year, then a fatigue evaluation is recommended. Next, the maximum stress range in each of the potentially critical fatigue details under the AREMA (2007) design loading is determined and compared to the variable amplitude fatigue limit (for riveted details) or the constant amplitude fatigue limit (for non-riveted details). For

Bridge 880.37, the girders and floorbeams at midspan require further analysis; however, the stringers do not based on this check. The next step was to determine the effective stress range at the midspan locations of a floorbeam and girder under historical traffic. To do this, the stress histories were simulated under the assumed historical traffic for each train model. These stress histories were then evaluated using a rainflow counting algorithm developed in MATLAB (Mathworks 2010) to obtain the stress ranges and type of cycle for each (i.e. half cycle or full cycle). At this point, the total number of stress cycles was determined based on the cycles per train and the number of trains crossing the structure which, in turn, is used to calculate the effective stress range. For riveted details, AREMA (2007) specifies that all stress ranges should be removed that cause the effective stress range to drop below the variable amplitude fatigue limit, which is 6 ksi (41.4 MPa). This is achieved by removing all stress ranges below a certain magnitude, checking the new effective stress range, and repeating until the effective stress range is greater than or equal to 6 ksi (41.4 MPa). For Bridge 880.37, it was found that for the floorbeam, the effective stress range was 6.16 ksi (42.5 MPa) with N equal to 6.19 million and for the girder, the effective stress range was 6.26 ksi (43.2) with N equal to 1.03 million after removing all stress cycles with a magnitude less than 5.0 ksi (34.5 MPa) and 2.34 ksi (16.1 MPa), respectively. Using these values, the Miner's sum to date was determined to be 0.704 for the floorbeams, and 0.123 for the girders. Based on the Miner's sums, these details still have a significant amount of life considering it took over 110 years to exhaust 70.4% of the fatigue life of the critical fatigue detail. Another factor that indicates that this structure has significant remaining life is that the simulated floorbeam strains were larger than the actual measured strains, thus making the fatigue analysis conservative.

8.2 Recommendations

The work described in this report has applications in developing a SHM system to guide bridge inspectors to critical fatigue details and to determine inspection intervals for complex structures like bridges. Structural health monitoring may be achieved by periodically updating a fatigue evaluation based on strains measured under actual traffic. This method may be used to estimate the remaining life of a structure rather than attempt to detect damage. Another potential SHM design could occasionally back-calculate the influence line for various components based on load tests with known train weights and compare the values based on measurements to the baseline curves. Fatigue evaluations may also be helpful in guiding bridge inspectors to critical locations. If the inspectors are guided to the most critical details, the likelihood of finding fatigue cracks increases, and thus the probability of a fatigue failure is reduced.

8.2.1 Applications to Structural Health Monitoring

For aging steel structures, fatigue-based SHM is a valuable tool. This method gives the owner of the structure an estimate of the remaining time before repairs are needed, and therefore the ability to budget funds more appropriately.

To apply a fatigue-based SHM system, the history of the structure must be known well enough to develop representative trains for use in the fatigue evaluation. Once the historical traffic has been applied, either by determining the effective stress range or the Miner's sum directly, an estimation of the remaining life may be performed based on projections for future traffic. The use of measured strains allows for the most accurate estimate of strains in the structure, and therefore the most accurate analysis. This method also makes it possible to detect changes in train traffic and in the distribution of loads through the structure under live load, which further assists in making accurate estimations of remaining life.

One major advantage of using fatigue life estimates in a SHM system is the reduction in required equipment. If a system were purchased that could be installed and removed as needed, a single system could service multiple structures, thus dividing the cost of the system and greatly reducing the per-structure cost of monitoring. This method is also relatively simple to implement since it does not require the sophisticated data processing used by acceleration-based SHM systems.

Another SHM application of this research comes from the way in which the stress histories were determined. In this report, the moment histories were determined using matrix multiplication as follows:

$$[M] = [IL][L] \qquad \text{EQ 8.1}$$

where *[M]* is the moment history, *[IL]* is the influence line ordinates for a particular location, and *[L]* is the loading matrix. This equation can be solved for *[IL]* where the *[L]* matrix is created using the known axle weights and locations and *[M]* can be created from measured strains using the following relationship:

$$[M] = [\varepsilon] * E * S \qquad \text{EQ 8.2}$$

where $[\varepsilon]$ is a vector containing the measured strains, E is the elastic modulus, and S is the section modulus. Substituting Equation 8.2 into Equation 8.1 yields:

$$[\varepsilon] = \frac{[IL][L]}{E * S} \qquad \text{EQ 8.3}$$

Rearranging Equation 8.1 and substituting in Equation 8.3 to solve for *[IL]* yields:

$$[\varepsilon] * E * S * [L]^{-1} = [IL] \qquad \text{EQ 8.4}$$

where $[L]^{-1}$ is the inverse of the loading matrix.

When performing this calculation, the loading matrix must be accurate, and therefore should be based on measured weights rather than approximate handbook values. It is also important to recognize the need to form the matrices correctly. Matrix multiplication is used and therefore it is essential that the number of entries in the [ε] matrix is equal to the number of rows in the *[L]* matrix. Also, the *[L]* matrix must be square so that the inverse can be taken. It is also important to recognize that peaks in the influence line based on measured values may not include the absolute peaks since the peaks of the strain matrix may not be included. This can be remedied by using curve fitting to approximate the magnitudes of the peaks.

The influence lines based on measured values can be used in a SHM system to track the behavior of the structure. Over time, the resulting influence line can be compared to a baseline, and any changes may be indicative of damage. This method can also be useful in estimating the remaining fatigue life. If the stress level in critical members changes, the fatigue evaluation can be adjusted accordingly.

8.2.2 Applications to Bridge Inspection

This method may also be applied to inform bridge inspectors which details require greater scrutiny based on the susceptibility to fatigue damage. In current practice, the bridge inspector receives little guidance as to what details pose the greatest danger of failure. Inspectors know which details in general are vulnerable to fatigue failure; however, they are often given no indication which specific details are near the end of their theoretical fatigue life on a particular structure. For structures that have been evaluated using the methods outlined in this report, the inspectors could be given a list of details that have attained some threshold value of the Miner's sum for each structure, thus increasing the focus on areas that may be more likely to fail. Another way in which this research can be applied to assist bridge inspectors is to alert the

inspector of unexpected changes in load distribution. If changes are detected when comparing influence lines (or when periodic load test data is analyzed), the inspector could be notified to look for potential causes of the redistribution of load.

Overall, the strain-based SHM method detailed in this report was successfully demonstrated to produce an assessment of the remaining fatigue life of a complex railroad bridge. The primary advantages of this SHM system are the ability to estimate the remaining life of a member, which can be used to prioritize bridge replacement and repair, and the fact that a SHM system used in this manner can be used on multiple structures, thus reducing the per-structure hardware cost. In addition to estimating the remaining life of the bridge, influence lines can be developed from the periodic measurements taken from a structure, and tracked over time to identify changes in live-load distribution which may indicate structural damage.

Works Cited

AASHTO (2010). *LRFD Bridge Design Specifications*, 5th Ed., American Association of State Highway and Transportation Officials, Washington, D.C.

AASHTOWare (2010). "Virtis version 6.3 (computer software)." American Association of State Highway and Transportation Officials, Washington, D.C.

Agerskov, H. (2000). "Fatigue in steel structures under random loading." *J. of Constructional Steel Research*, 53, 283-305.

Al-Emrani, M. and Kliger, R. (2003) "FE analysis of Stringer-to-floor-beam connections in riveted railway bridges" *J. of Constructional Steel Research*, 59(7), 803-818.

American Wood Council (2005). *National Design Specification for Wood Construction*, American Forest and Paper Association, Washington, D.C.

AREMA (2007). *Manual for Railway Engineering*. American Railway Engineering and Maintenance-of-Way Association, Lanham, MD.

BDI (2005). *Structural Testing System II Operation Manual*. Bridge Diagnostics, Inc., Boulder, CO.

Boresi, P., Schmidt, J. (2003). *Advanced Mechanics of Materials*, 6th ed., Wiley, New York, NY, USA.

Brownjohn, J.M.W. (2007). "Structural health monitoring of civil infrastructure." *Philosophical transactions of the Royal Society A- Mathematical Physical and Eng. Sciences*, 365(1851), 589-622.

Brownjohn, J.M.W., Moyo, P., Omenzetter, P., et al. (2005). "Lessons from monitoring the performance of highway bridges." *Struct. Control & Health Monitoring*, 12(3-4), 227-244.

Caglayan, B.O., Ozakgul, K., and Tezer, O. (2009) "Fatigue Life Evaluation of a Through-Girder Steel Railway Bridge" *Engineering Failure Analysis*, 16, 765-774.

Caicedo, J.M and Dyke, S.J. (2005). "Experimental validation of structural health monitoring for flexible bridge structures." *Struct. Control & Health Monitoring*, 12(3-4), 425-443.

Caicedo, JM, Dyke, SJ, Johnson, EA (2004). "Natural Excitation Technique and Eigensystem Realization Algorithm for Phase I of the IASC-ASCE Benchmark Problem: Simulated Data." *J. of Engineering Mech. – ASCE*, 130(1), 49-60.

Cardini, A.J. and DeWolf, J.T. (2009). "Long-term Structural Health Monitoring of a Multi-girder Steel Composite Bridge Using Strain Data." *Str. Health Monitoring- An Int. J*., 8(1), 47-58.

Castro Guillen, Thelma A. (2008). "A collaborative approach for load rating of state owned bridges." M.S. Thesis, New Mexico St. Univ., Las Cruces, NM.

Catbas, F.N., Susoy, M., Frangopol, D.M. (2008). "Structural health monitoring and reliability estimation: Long span truss Bridge application with environmental monitoring data." *Eng. Struct*., 30(9), 2347-2359.

Cheung, M.S. and Li, W.C. (2003). "Probabilistic fatigue and fracture analysis of steel bridges." *J. of Structural Safety*, 23, 245-262.

CISC (1967). *Handbook of Steel Construction*. Canadian Institute of Steel Construction, Markham, ON, Canada.

Code of Federal Regulations (CFR). (2007). "National Bridge Inspection Standards." 23CFR650, Federal Highway Administration, Washington, DC.

Connor, R. J. and Fisher, J. W. (2006) "Consistent Approach to Calculating Stresses for Fatigue Design of Welded Rib-to-Web Connections in Steel Orthotropic Bridge Decks" *J. of Bridge Eng*., 11(5), 517-525.

Cousins, T. E., Stallings, J. M., Lower, D. A., and Stafford, T. E. (1998) "Field Evaluation of Fatigue Cracking in Diaphragm-Girder Connections." *J. of Performance of Constructed Facilities*, 12(1), 25-32.

De Corte, W and Van Bogaert, P. (2006) "The use of continuous high-frequency strain gauge measurements for the assessment of the role of ballast in stress reduction on steel railway bridge decks." *Insight*, 48(6), 352-356.

Dexter, R. J., Wright, W. J, and Fisher, J. W. (2004). "Fatigue and Fracture of Steel Girders." *J. of Bridge Eng*., 9(3), 278-286.

Ebrahimpour, A., Maragakis, E. A., and Ismail, S. (1992) "Fatigue reliability model for railway bridges" *Probabilistic mechanics and structural and geotechnical reliability: proceedings of the sixth specialty conference*, 320-323.

Farhey, D.N. (2005). "Bridge instrumentation and monitoring for structural diagnostics." *Struct. Health Monitoring-An International J*., 4(4), 301-318.

Farhey, D.N. (2006). "Instrumentation system performance for long-term bridge health monitoring." *Struct. Health Monitoring-An International J.*, 5(2), 143-153.

Farhey, D.N. (2007). "Quantitative assessment and forecast for structurally deficient bridge diagnostics." *Struct. Health Monitoring-An International J.*, 6(1), 39-48.

Federal Register (2010). "Bridge Safety Standards." Volume 75(135), July 15, 2010.

Fei, Q.G., Xu, Y.L., Ng, C.L. (2007). "Structural health monitoring oriented finite element model of Tsing Ma bridge tower." *International J. of Struct. Stability and Dynamics*, 7(4), 647-668.

Fisher, J.W., et al. (1973). "Fatigue Strength of Steel Beams with Transverse Stiffeners and Attachments." *NCHRP Research Results Digest*, 44.

Fuhr, P.L., Huston, D.R., Nelson, M., et al. (1999). "Fiber optic sensing of a bridge in Waterbury, Vermont." *J. of Intelligent Material Systems and Struct.*, 10(4), 293-303.

Guan, H., Karbhari, V.M. and Sikorsky, C.S. (2006). "Web-based structural health monitoring of and FRP composite bridge." *Computer-Aided Civil and Infrastructure Eng.*, 21(1), 39-56.

Guan, H., Karbhari, V.M., Sikorsky, C.S. (2007). "Long-term structural health monitoring system for a FRP composite highway bridge structure." *J. of Intelligent Material Systems and Struct.*, 18(8), 809-823.

Guo, T., Li, A.Q., Li, J.H. (2008). "Fatigue Life Prediction of Welded Joints in Orthotropic Steel Decks Considering Temperature Effect and Increasing Traffic Flow." *Struct. Health Monitoring-An International J.*, 7(3), 189-202.

He, X.H., Chen, Z.Q., Yu, Z.W., et al. (2006). "Fatigue damage reliability analysis for Nanjing Yangtze River Bridge using structural health monitoring data." *J. of Central South University of Technology*, 13(2), 200-203.

Heild, Colleen (2010). "State Ends Up With 200 Miles of Track It Can't Use." *Albuquerque Journal*, December 5, 2010.

Heild, Colleen (2011). "Track Deal Derailed." *Albuquerque Journal*, April 29, 2011.

Howell, D.A. and Shenton, H.W. (2006). "System for in-service strain monitoring of ordinary bridges." *J. of Bridge Eng.*, 11(6), 673-680.

Hsieh, K.H., Halling, M.W., and Barr P.J. (2006). "Overview of vibrational structural health monitoring with representative case studies." *J. of Bridge Eng.*, 11(6), 707-715.

Imam, B.M., Righiniotis, T.D., Chryssanthopoulos, M.K., and Bell, B. (2008) "Probabilistic Fatigue Life Estimates for Riveted Railway Bridges" *Proceedings of the 3rd Int. Conf. on Bridge Maint., Safety, and Management*, 499-500.

Irvine, Tom (2000). “An Introduction to Frequency Response Functions.” *Inside Structural Dynamics*, <http://www.cs.wright.edu/~jslater/SDTCOutreachWebsite/intro_freq_resp_functions.pdf> (Aug 20, 2010).

Jerez, C.A.R. (2007). “Structural health monitoring methodology for simply supported bridges: numerical implementation.” *Revista Facultad De Igneria-Universidad De Antioquia*, 37, 42-55.

Kim, S.-H., Lee, S.-W., and Mha, H.-S. (2001) “Fatigue reliability assessment of existing steel railroad bridges” *Engineering Structures*, 23, 1203-1211.

Kister, G., Winter, D., Badcock, R.A., et al. (2007). “Structural health monitoring of a composite bridge by using Bragg grating sensors. Part 1: Evaluation of adhesives and protective systems for the optical sensors.” *Eng. Struct.*, 29(3), 440-448.

Kuo, Chen-Ming and Huang, Cheng-Hao (2009). "Two Approaches of Finite-Element Modeling of Ballasted Railway Track." *J. of Geotechnical and Geoenvironmental Eng.*, 135(3), 455-458.

Laman, J. A. and Nowak, A. S. (1996). “Fatigue-Load Models for Girder Bridges.” *J. Struct. Eng.*, 122(7), 726-733.

Lee, J.J., Fukuda, Y., Shinozuka, M., et al. (2007). “Development and application of a vision-based displacement measurement system for structural health monitoring of civil structures.” *Smart Struct. And Systems*, 3(3), 373-384.

Lee, M.L. and Chiu, W.K. (2005). “Comparative study on impact force prediction on a railway track-like structure.” *Struct. Health Monitoring-An International J.*, 4(4), 355-376.

Li, H., Ou, J.P., Zhao, X.F., et al. (2006). “Structural health monitoring system for the Shandong Binzhou Yellow River Highway Bridge.” *Computer-Aided Civil and Infrastructure Eng.*, 21(4), 306-317.

Li, Z.X. and Chan T.H.T. (2006). “Fatigue criteria for integrity assessment of long-span steel bridge with health monitoring.” *Theoretical and Applied Fracture Mechanics*, 46(2), 114-127.

Li, Z.X., Chan T.H.T, and Zheng, R. (2003). “Statistical analysis of online strain response and its application in fatigue assessment of a long-span steel bridge.” *Eng. Struct.*, 25(14), 1731-1741.

Liu, C.Y., Olund J.H., Cardini A., et al. (2008). “Structural Health Monitoring of bridges in the State of Connecticut.” *Earthquake Eng. And Eng. Vibration.*, 7(4), 427-437.

Lynch, J.P., Law, K.H., Kiremidjian, A.S., et al. (2004). "Design and performance validation of a wireless sensing unit for structural monitoring applications." *Struct. Eng. And Mechanics*, 17(3-4), 393-408.

MacDougall, C., Green, M. F., and Shillinglaw, S. (2006) "Fatigue Damage of Steel Bridges Due to Dynamic Vehicle Loads." *J. of Bridge Eng.*, 11(3), 320-328.

Makkonen, M. (2009). "Predicting the total fatigue life in metals." *International J. of Fatigue*, 31(7), 1163-1175.

Mathworks (2010). "Matlab version 7.11.0584 (computer software)." Mathworks, Natick, MA.

Mencik, J, Beran, L., and Culek, B. (2007) "Improved Safe-Life prediction of existing bridge structures" *Bridge design, construction and maintenance*, 438-447.

Miner, MA (1945). "Cumulative damage in fatigue." *ASME J. of Appl. Mech.*, 12(3), A159-A1964.

MotivePower (2010). "MPX Commuter Locomotive" *Locomotives*, < http://www.motivepower-wabtec.com/locomotives/commuter/mpxpress.php> (Jun 5, 2010).

Moyo, P., Brownjohn, J.M.W, and Omenzetter, P. (2004). "Highway bridge live loading assessment and load carrying capacity estimation using a health monitoring system." *Struct. Eng. And Mechanics*, 18(5), 609-626.

Muro-Villanuava, Fabricio (2010). "Load Rating Approach for State Owned Railroad Bridges." M.S. Thesis, New Mexico St. Univ., Las Cruces, NM.

New Mexico Rail Runner (2011) "Train Schedule." <www.nmrailrunner.com/schedule.asp> (July 17, 2010).

Ni, Y.Q., Xia, H.W., Ko, J.M. (2008). "Structural performance evaluation of Tsing Ma Bridge deck using long-term monitoring data." *Modern Physics Letters B*, 22(11), 875-880.

NIESŁONY A. (2009) "Determination of fragments of multiaxial service loading strongly influencing the fatigue of machine components." *Mechanical Systems and Signal Processing*, 23(8), 2712-2721.

Omenzetter, P., Brownjohn, J.M.W., and Moyo, P. (2004). "Identification of unusual events in multi-channel bridge monitoring data." *Mechanical systems and signal processing*, 18(2), 409-430.

Owen, J.S. (2003). "Monitoring the degradation of reinforced concrete beams under cyclic loading." *Damage Assessment of Structures, Proceedings: Key Eng. Materials*, 245-2, 307-314.

Owen, J.S. and Haritos, N. (2003). "Damage detection in large-scale laboratory bridge models." *Damage Assessment of Structures, Proceedings: Key Eng. Materials*, 245-2, 35-42.

Patjawit, A. and Kanok-Nukulchai, W. (2005). "Health monitoring of highway bridges based on Global Flexibility Index." *Eng. Struct*., 27(9), 1385-1391.

Paris, P.C., Gomez, M. P., and Anderson, M. E. (1961). "A rational analytical theory of Fatigue." *Trends Eng.*, 13, 9-14.

Philbrick, T. W. Jr., Zodo, G. W., and Schiff, S. D. (1995). "Fatigue Assessment of Through Plate Girder Railway Bridges." *J. Struct. Eng*., 121(11), 1613-1619.

Post, G. Jeff, Frank, Karl H., and Tahmassebi, Bahran (1988). "Estimating Residual Fatigue Life of Bridges." Report FHWA/TX/464-1F, Texas Dept. of Transportation.

Reynders, E., De Roeck, G., Bakir, P.G., et al. (2007). "Damage identification on the Tilff bridge by vibration monitoring using optical fiber strain sensors." *J. of Eng. Mechanics-ASCE*, 133(2), 185-193.

Righiniotis, T.D. (2004). "Simplified calculations involving the maximum load on bridge fatigue details under inspection. Part II: Fatigue." *J. of Constructional Steel Research*, 60, 825-839.

Roach, D. and Rackow, K. (2007). *Development and Validation of Bonded Composite Doubler Repairs for Comercial Aircraft.* Report SAND2007-4088, Sandia National Laboratories, Albuquerque, NM.

Roach, D., Rackow, K. (2006) "Health Monitoring of Aircraft Structures Using Distributed Sensor Systems," DoD/NASA/FAA Aging Aircraft Conference.

Roach, D. (2009) "Real Time Crack Detection Using Mountable Comparative Vacuum Monitoring Sensors," *Journal of Smart Structures and Sensors*, Vol. 5, No. 4.

Roach, D. and Pinsonnault, J. (2009) "Use of Embedded Sensors to Address Periodic Inspections for Cracks on Regional Aircraft," Structural Health Monitoring, DEStech Publisher, Lancaster, PA, Int'l Workshop on Structural Health Monitoring.

Roddis, W. M. K. and Zhao, Y. (2003) "Finite-Element Analysis of Steel Bridge Distortion-Induced Fatigue." *J. of Bridge Eng*., 8(5), 259-266.

SAP2000 Version 14.2.2. (2010) Computers and Structures, Inc. Berkely, CA.

Sharma, V. and Choros, J. (1996) "Program for estimating the remaining fatigue life of steel railway bridges" *Building an International Community of Structural Engineers ; Proceedings of Str. Congress XIV*, Chicago, Ill, Apr 15-18, 223-229.

Stone, Marissa (2006). “Phase One of Commuter Rail Between Belen and Bernalillo Finalized.” *¿Que Pasa?; A Monthly Newsletter of the New Mexico Department of Transportation*, March issue, 1.

Tennyson, R.C., Mufti, A.A., Rizkalla, S., et al. (2001). “Structural Health monitoring of innovative bridges in Canada with fiber optic sensors.” *Smart Materials & Struct.*, 10(3), 560-573.

Tobias, D. H. and Foutch, D. A. (1995) “Overview of a Research Program Investigating Riveted Railway Bridges” *Structural Eng. Review*, 7(3), 231-243.

URS Corporation (2005). *Albuquerque-Santa Fe Transportation Corridor Alternatives Analysis Final Report*. Albuqurque, NM.

Wang, M.L., Heo, G., and Satpthi, D. (1998). “A health monitoring system for large structural systems.” *Smart Materials & Struct.*, 7(5), 606-616.

Wang, M.L., Xu, F.L., and Lloyd, G.M. (2000). “Results and implications of the damage index method applied to a multi-span continuous segmental prestressed concrete bridge.” *Struct. Eng. And Mechanics*, 10(1), 37-51.

Wirsching, PH. (1995). “Probabilistic Fatigue Analysis.” *Probabilistic Structural Mechanics Handbook*, C. Sundararajan, Ed., Chapman and Hall, New York, NY, USA.

Yang, L.A, Powrie, W., Priest, J.A (2009). “Dynamic Stress Analysis of a Ballasted Railway Track Bed during Train Passage.” *J. of Geotechnical and Geoenvironmental Eng.*, 135(5), 680-689.

Zhang, Q.W and Zhou, Y. (2007). “Investigation of the applicability of current bridge health monitoring technology.” *Struct. And Infrastructure Eng.*, 3(2), 159-168.

Zhou, E. Y. (2006) “Assessment of Bridge Remaining Fatigue Life through Field Strain Measurements.” *J. of Bridge Eng.*, 11(6), 737-744.

APPENDIX A

New Mexico Department of Transportation

RAILROAD BRIDGE INSPECTION REPORT

Structure No.	**AB0880.37**	Subdivision	Albuquerque	**(90) Insp. Date**	**3/26/2011**
Plans Available?	Yes	County	Sandoval	Town/Siding	Algodones
(16) Latitude	35° 22' 16.00" N	No. of Tracks	1	(34) Skew Angle	0°
(17) Longitude	106° 29' 42.00" W	Other features on bridge	None		
Subdivision Milepost		Access to Structure	Hwy 313 runs parallel to track.		
(112) Length Over 10 feet?	Yes	(41) Status Center Height	NA NA	(49) Str. Length	90'-0"
(6) Features Intersected	Angostura Arroyo		(9) Location (nearest siding/station) or additional info. South of Algodones; 1.62 miles south of Hwy 315 and Hwy 313 junction.		
(43) Description	1 Simple span at 87'-6" span length. Ballast timber deck planks with thru-plate girders on concrete abutments. Main Load Carrying Members: Two 8' -4 1/2" depth Girders.				
Walks & Handrails? (Y,N)	N	Utilities on bridge? (Y,N)	N	If yes, which?	NA
(27) Year Built	1898	Year Rebuilt	NA	Project Number	
(21) Maintenance Responsibility	State	(91) Inspection Frequency	12 Months	Last Inspection Date	3/11/2010
(92) Fracture Critical? Yes or No	Yes	Underwater Inspection? Yes or No	No	(113) Scour Critical? Yes or No Unknown	No
Other Special Inspections Reqd? Yes or No	No	If Yes, complete the following: Type of Inspection and special Personnel or Equipment Reqd:	Regularly scheduled annual inspection.		
		Next Special Inspection Date and Interval	None		
Special Equipment Used During Inspection	None				
Work Done Since Last Inspection	None				
Inspection Performed By: (list present personnel)	T. Castro J. DiGiacomo	Weather conditions at time of inspection	Hi 63°; Lo 40° Sunny and Calm		
List additional attachments included with this report	Sketch of bridge, Photos, and Survey of Channel and Cross Sections from initial inspection on 3/19/2009. Additional photos taken on this inspection.				

This M-211RR Report shall include all applicable attachments. Additional attachments should be listed and may include Vertical Clearance Sheets, Channel Plan & Profiles, Photographs, Sketches, Bridge Location Sheets, Load Rating Calculations and/or other documents included as part of this report.

General Comments			
Team Leader	Thelma A. Castro, M.S., E.I.	Reviewer	Andrew M. Leifheit, P.E., S.E.
Signature	Thelma A. Castro	Signature	
Title	Bridge Engineer	Title	Senior Bridge Engineer
Date:	4/28/11	Date:	4/25/11

Figure A1: Page 1 of inspection report for Bridge 880.37 on March 26, 2011.

CONDITION REPORT

Structure No.	AB0880.37	(90) Insp. Date	3/26/2011		
Route Under	NA	Route Under	NA	Route Under	NA
Milepost	NA	Milepost	NA	Milepost	NA
(19) Detour Length	NA	(19) Detour Length	NA	(19) Detour Length	NA
No. of lanes or Railroad Tracks	1	No. of lanes or Railroad Tracks	NA	No. of lanes or Railroad Tracks	NA
Miscellaneous	NA				

(62) Box Culvert Condition

Top Slab	None	Rating	NA
Bottom Slab	None	Rating	NA
Barrel Walls	None	Rating	NA
Wingwalls	None	Rating	NA
Parapets	None	Rating	NA
		(62) Overall Box Culvert Rating	**NA**

(62) Pipe Culvert Condition

Pipes	None	Rating	NA
Headwalls	None	Rating	NA
Wingwalls	None	Rating	NA
		(62) Overall Pipe Culvert Rating	**NA**

Figure A2: Page 2 of inspection report for Bridge 880.37 on March 26, 2011.

CONDITION REPORT

Structure No.	AB0880.37	(90) Insp. Date	3/26/2011

(58) Deck Condition

Deck (Open or Ballast?) (List material type)	Ballast timber deck planks. The ties are sitting high on the ballast. In satisfactory condition.	Rating	6
Ballast Depth	10.0" of ballast. Depth from bottom of tie to top of deck. There is slightly too much ballast. In satisfactory condition.	Rating	6
Deck Curbs (Include number and condition)	Timber curbs which are 11 1/2" high. In satisfactory condition.	Rating	6
Walks and Handrails	None	Rating	NA
Drains	None	Rating	NA
		(58) Deck Rating	**6**

(59) Superstructure Condition

For steel or concrete spans, include girder spacing, girder size and number of girders per span
For timber or concrete trestles, include beam or stringer size

Girders/ Trusses	Thru-plate girders; riveted construction. The paint on web is missing at panels 5 - 8 at web stiffeners on both girders. Some stiffeners placed on the inside of the girders have full continuous welds, while others have only intermittent welds. The first 4 interior stiffners from the abutments for both girders have intermittent welds. Girders top flanges at the TTEast end have small gouges. Some pack rust between top cover PL's on Girder #2 (@ inside face of gider & at TTWest end of topmost PL). Bottom chords have debris and mud on them. Approx. 12' min. clearance @ top of rail (btwn. knee bracings). In satisfactory condition.	Rating	6
Diaphragms/ Floor System	Floor beams-riveted built up section. Four stringers per panel. Total of 12 panels; 7' -3 1/2" panel length. Girders #1 & #2 pack rust on gusset plates at Bent #1. Some corrosion on the gusset plates. Also, some gusset plates have been cut. Girder #2 pack rust on gusset plate at Bent #2. In satisfactory condition.	Rating	6
Bearings	Bent #1 has expansion bearings and Bent #2 has fixed bearings. Need to clean the abutment seats from debris. There is one missing nut and the other is loose on the fixed bearing (i.e., Bent #2) for Girder #1. In satisfactory condition.	Rating	6
Coating Sys.	The girders are painted. In satisfactory condition.	Rating	6
		(59) Superstructure Rating	**6**

(60) Substructure Condition

For steel or concrete spans, include material type for abutments and piers
For timber or concrete trestles, list pile types, cap types, and number of piles, types, and sizes

Abutments/ End Bents	Abutments are cast-in-place concrete; painted. There are small amount of spalling and some cracking at the abutments and backwall. The backwall is spalled and with efflorescence at Bent #2. In fair condition.	Rating	5
Piers/ Interior Bents	None	Rating	NA
Foundation Settlement?	No foundation settlement or none visible.	Rating	6
Slope Protec.	None	Rating	NA
Coating Sys.	Painted or coated substructure. Paint is cracking.	Rating	5
		(60) Substructure Rating	**5**

Figure A3: Page 3 of inspection report for Bridge 880.37 on March 26, 2011.

CONDITION REPORT

Structure No.	AB0880.37	(90) Insp. Date	3/26/2011	

(61) Channel and Channel Protection

Channel Description and Alignment	Angostura Arroyo; good alignment with the bridge. A major high water flow. In satisfactory condition.	Rating	6
Scour, Erosion, Silt and/or Obstructions	No scour, erosion, or obstruction observed.	Rating	6
Channel Protection	There is large riprap upstream, on TTSouth side of bridge. In satisfactory condition.	Rating	6
High Water Marks Detector Present?	There are signs that water has reached the bottom flanges. No water detector on the bridge. In fair condition.	Rating	5
		(61) Channel and Channel Protection Rating	**6**

Approach Condition

Embankment	Embankment in satisfactory condition.	Rating	6
Track and Ballast	136 lb rail on timber ties. The ties are sitting high on the ballast. The timber ties are weathered and some are split. In satisfactory condition.	Rating	5
Shoulders	Shoulders in satisfactory condition.	Rating	6
Signage (No specifics)	None	Rating	NA
		Approach Condition	**6**

Traffic Safety Features

For railroad over roadway only

Rating Table (0,1, or N)

1-Adequate

0-Inadequate

N-Not needed

Bridge Railings	None	Rating	NA
Transitions	None	Rating	NA
Approach Guardrail	None	Rating	NA
Approach Rail Ends	None	Rating	NA
		Traffic Safety Features	**NA**

Figure A4: Page 4 of inspection report for Bridge 880.37 on March 26, 2011.

APPRAISAL

Structure No. AB0880.37 **Inspection Date:** 3/26/2011

(69) Under Clearances

Route or Feature	Direction(s)	Vertical Measurements	Signed Clearance	Horizontal Clearance	Measured from ( ) to ( )	Lateral Left	Lateral Right
NA							

(70) Bridge Rating

Rating [ ]

If Load Capacity is Revised Attach Computations

Normal Rating E56.8 Maximum Rating E84.0

(71) Waterway Adequacy

Rating 5

Angostura arroyo.

Recommendations

Immediate	
Short Term	1. Clean the bearings from debris built-up (specifically rocker bearings at Bent #1). 2. Check shear stress in girder web. 3. Seal cracks at the concrete bents.
Long Term	1. Continue to monitor the condition of the bridge.

Figure A5: Page 5 of inspection report for Bridge 880.37 on March 26, 2011.

PONTIS Data Collection

Structure No. AB0880.37 **Subdivision:** Albuquerque **Inspection Date:** 3/26/2011

ELEMENT	DESCRIPTION	ENV	TOTAL QUANTITY	CONDITION 1	CONDITION 2	CONDITION 3	CONDITION 4
054	Timber Slab (SF)	2	1260		1260		
107	Painted Steel Open Girder/Beam (LF)	2	180		180		
113	Painted Steel Stringers (LF)	2	350		350		
215	Reinforced Concrete Abutment (LF)	2	48		48		
311	Moveable Bearing (EA)	2	2		2		
313	Fixed Bearing (EA)	2	2		2		
152	Painted Steel Floor Beam	2	199.33		199.33		
357	Pack Rust				1		

Figure A6: Page 6 of inspection report for Bridge 880.37 on March 26, 2011.

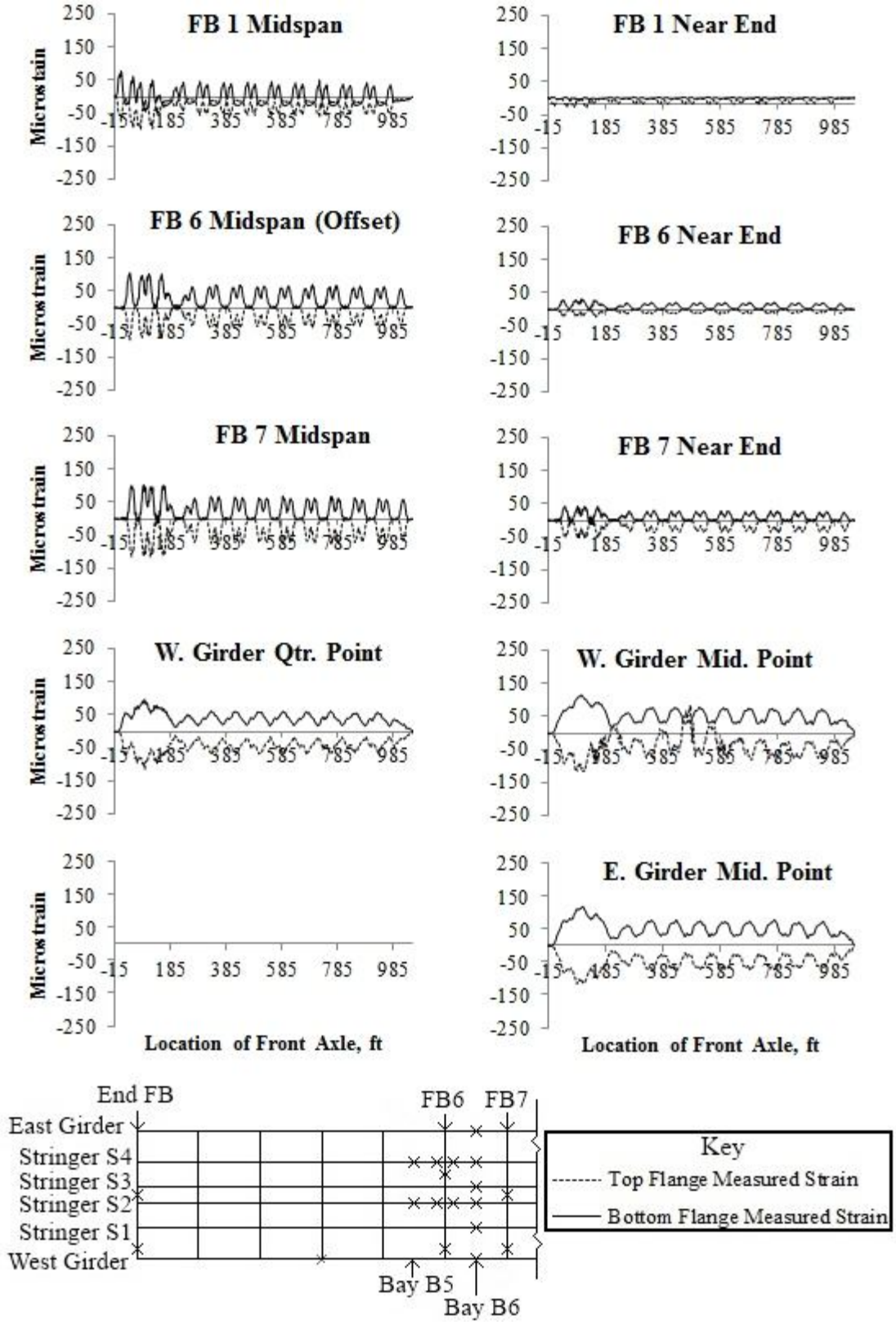

Figure A7: Measured strain data for Train 2.

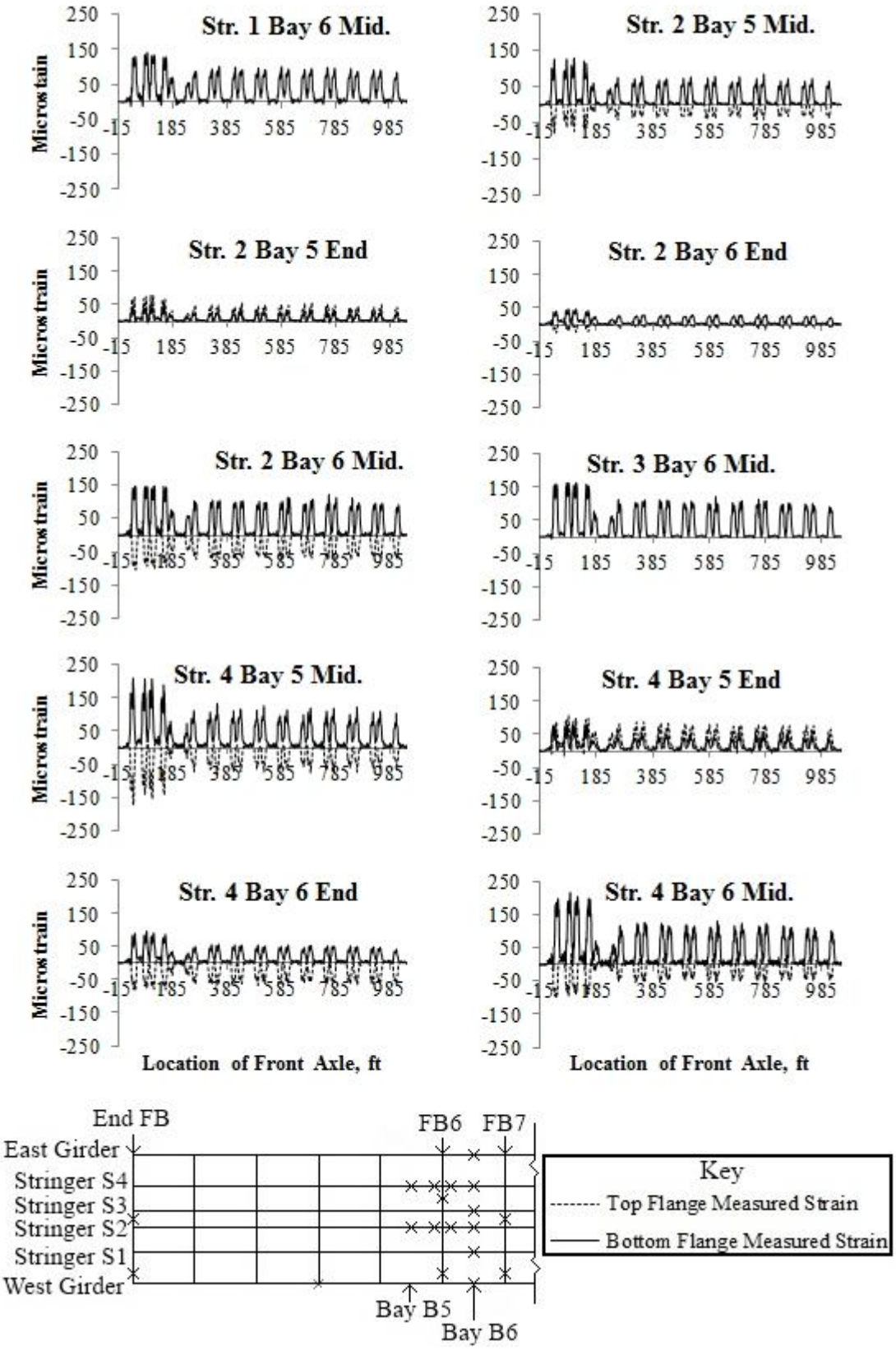

Figure A8: Measured strain data for Train 2 (cont.).

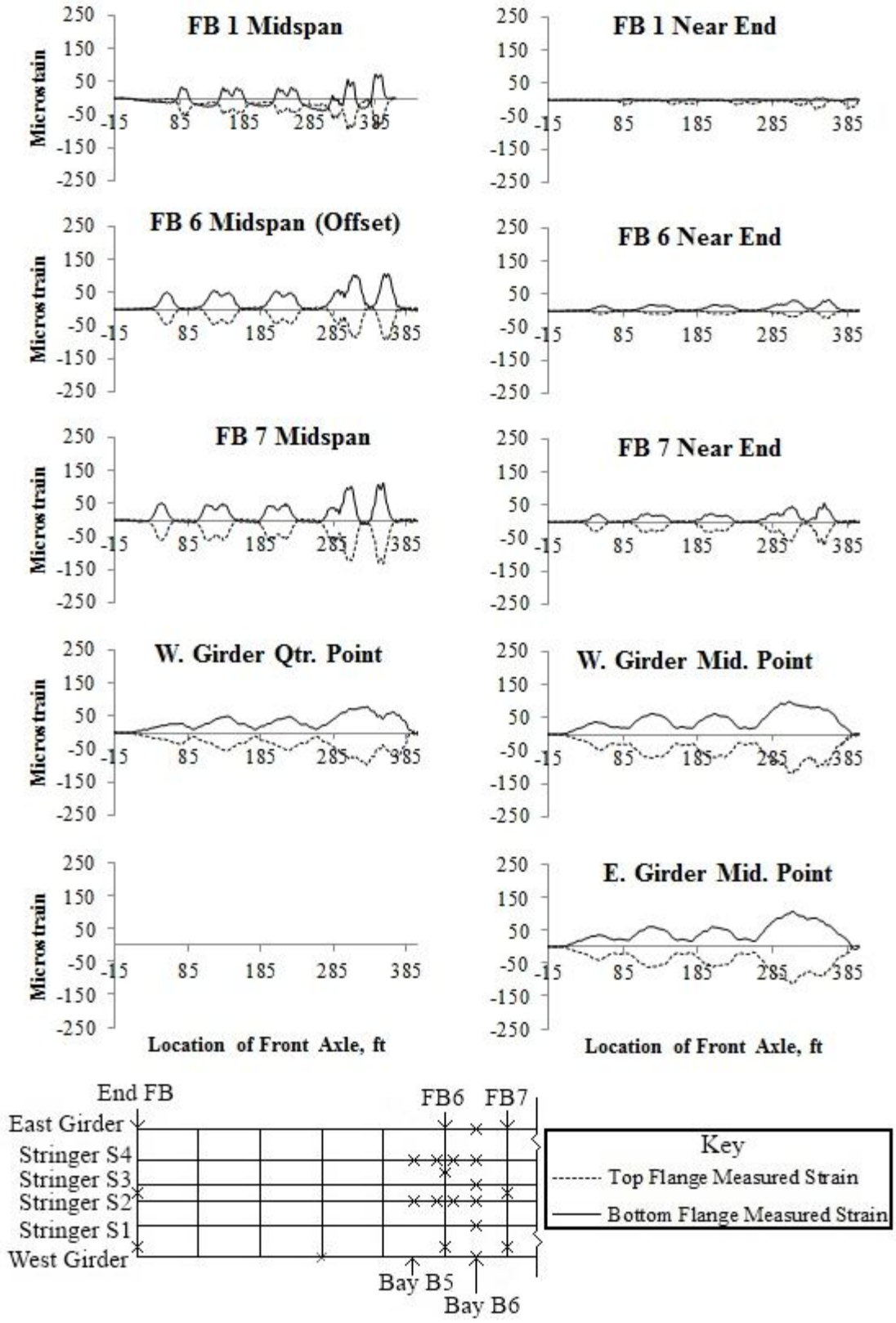

Figure A9: Measured strain data for Train 3.

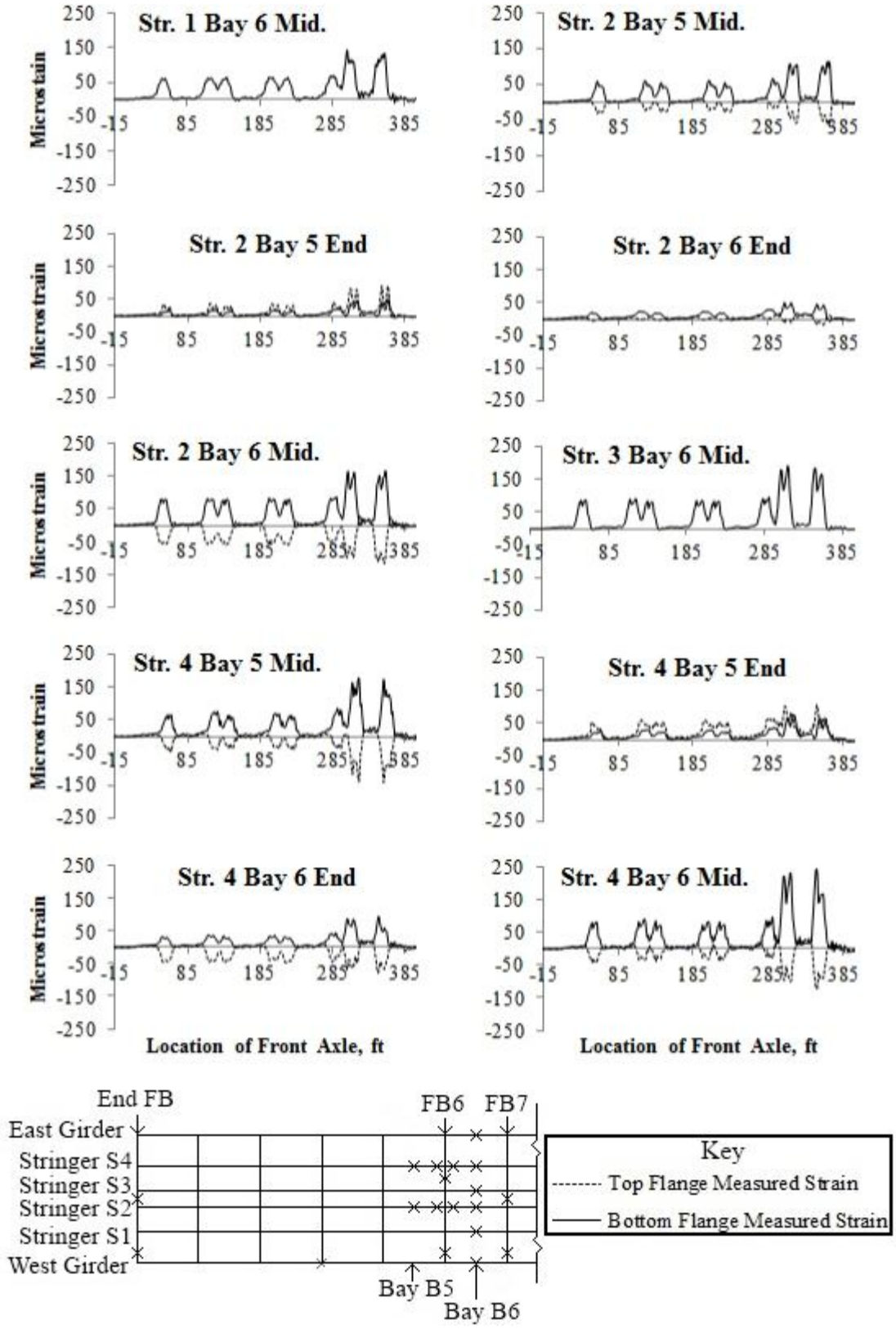

Figure A10: Measured strain data for Train 3 (cont.).

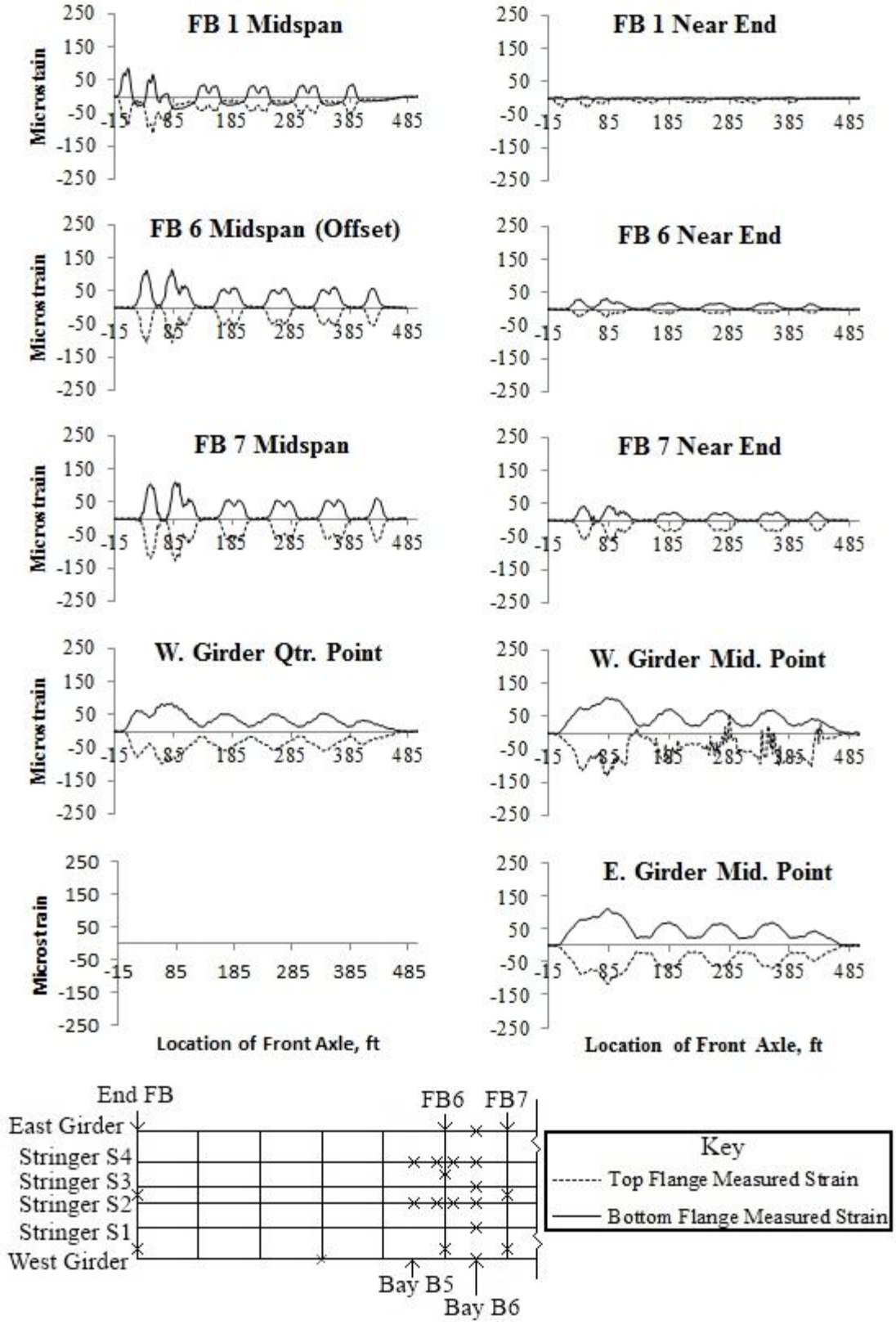

Figure A11: Measured strain data for Train 4.

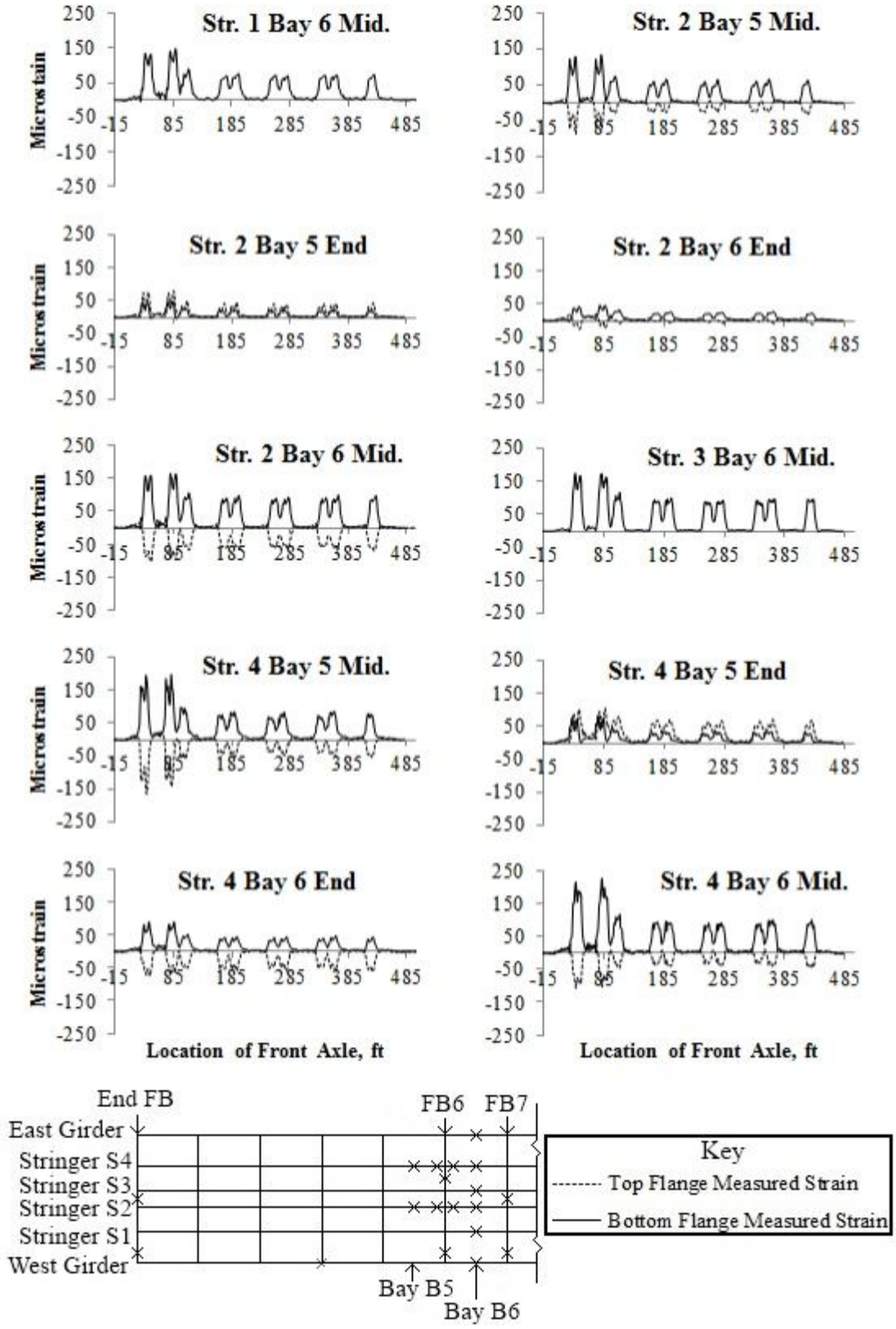

Figure A12: Measured strain data for Train 4 (cont.).

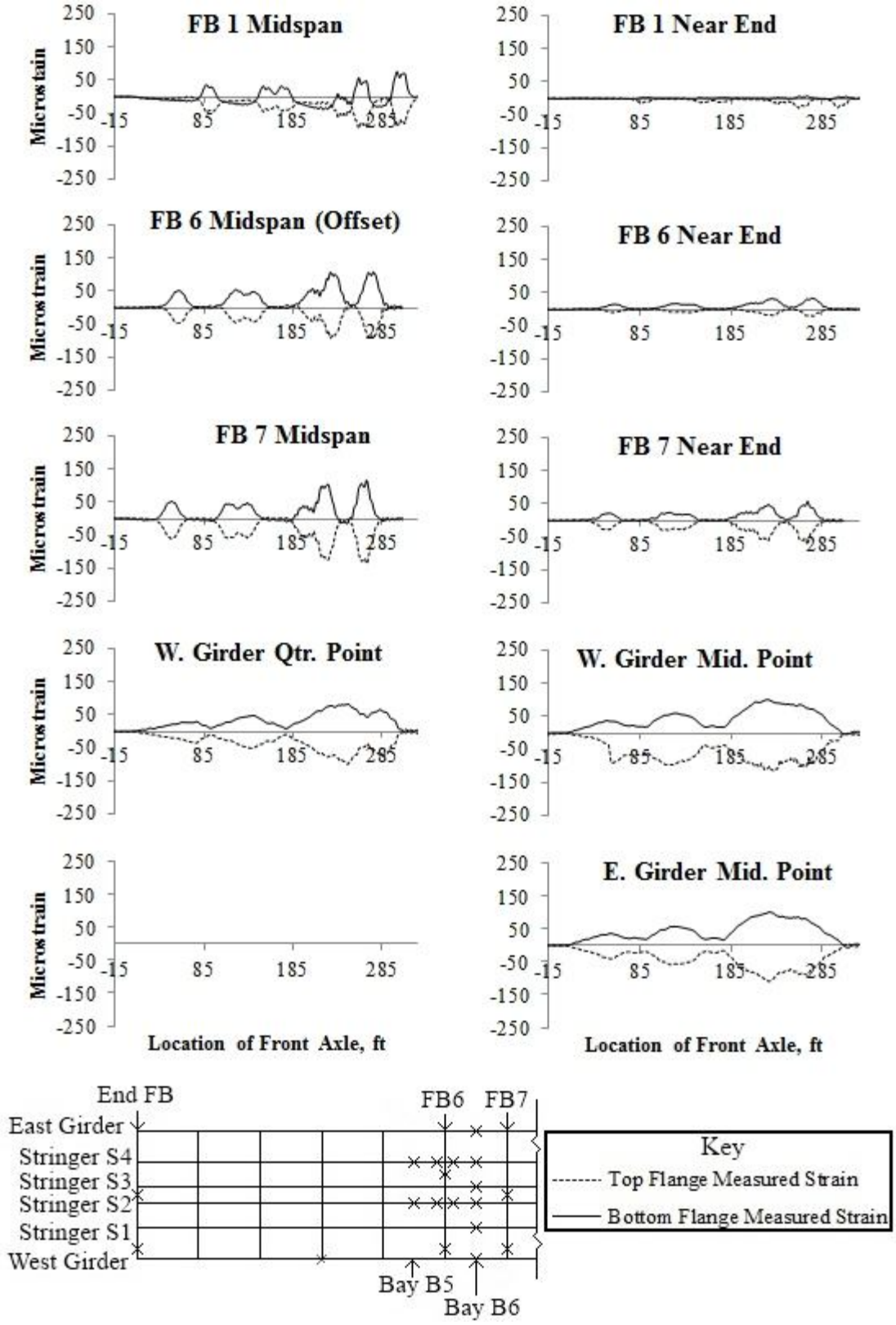

Figure A13: Measured strain data for Train 5.

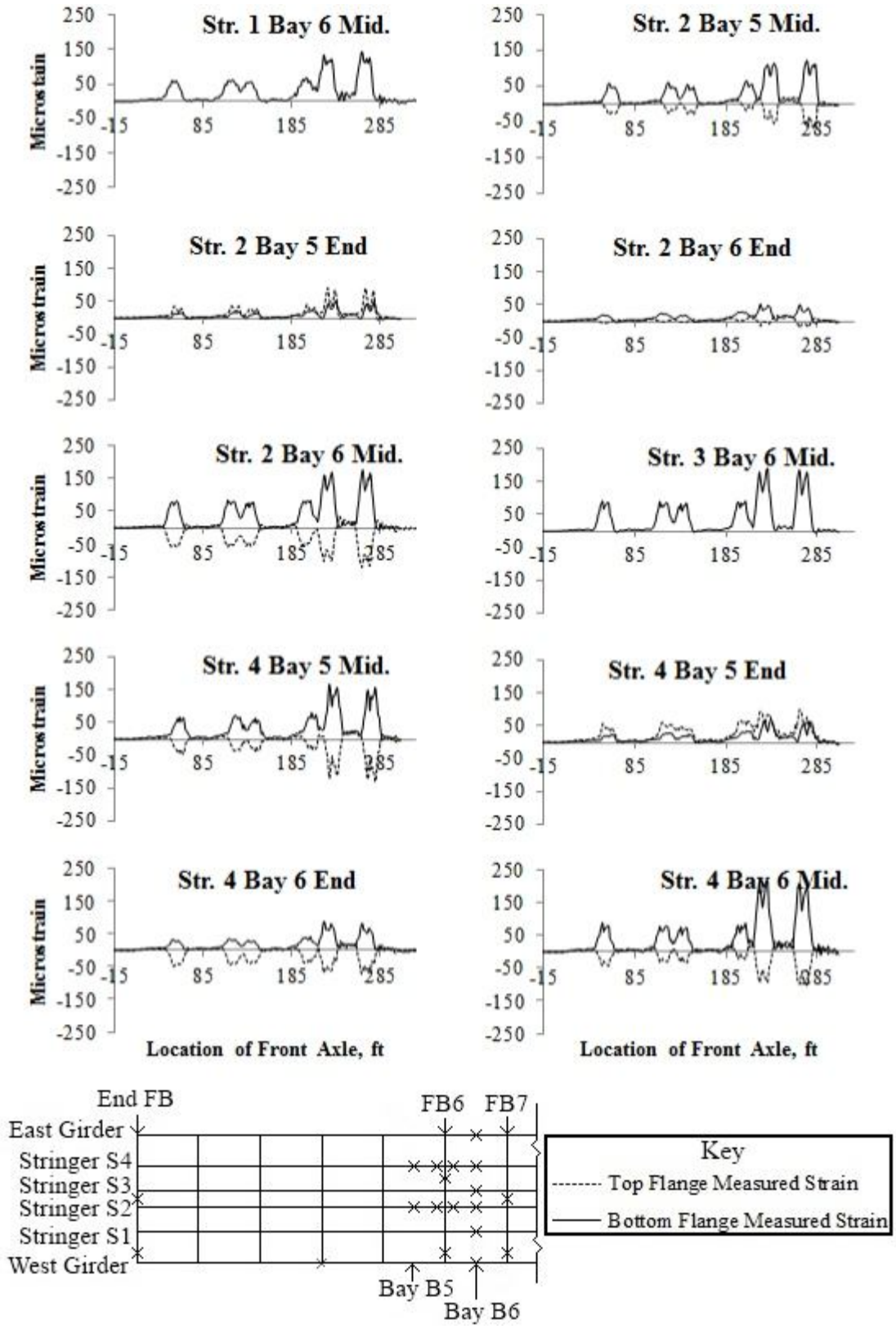

Figure A14: Measured strain data for Train 5 (cont.).

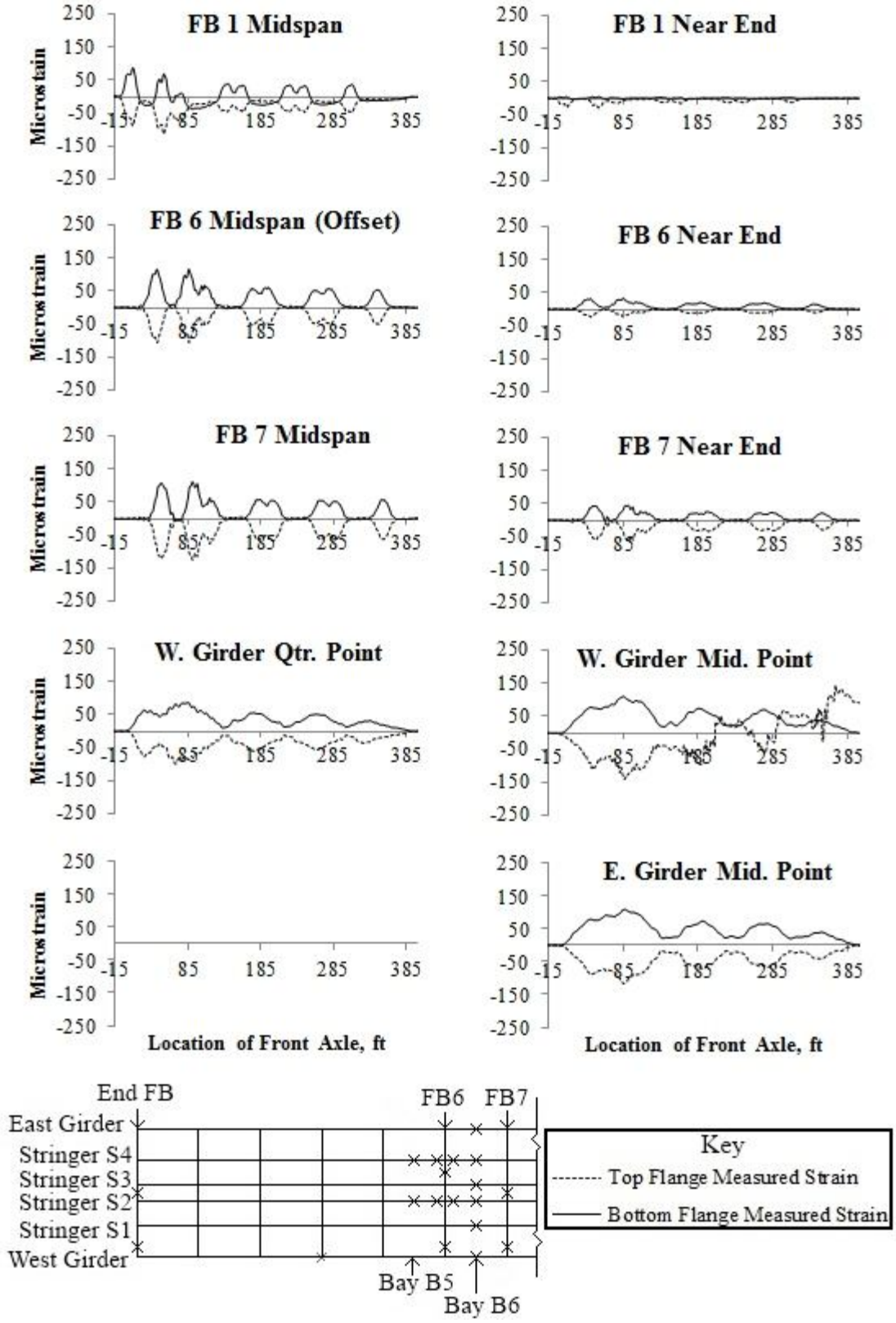

Figure A15: Measured strain data for Train 6.

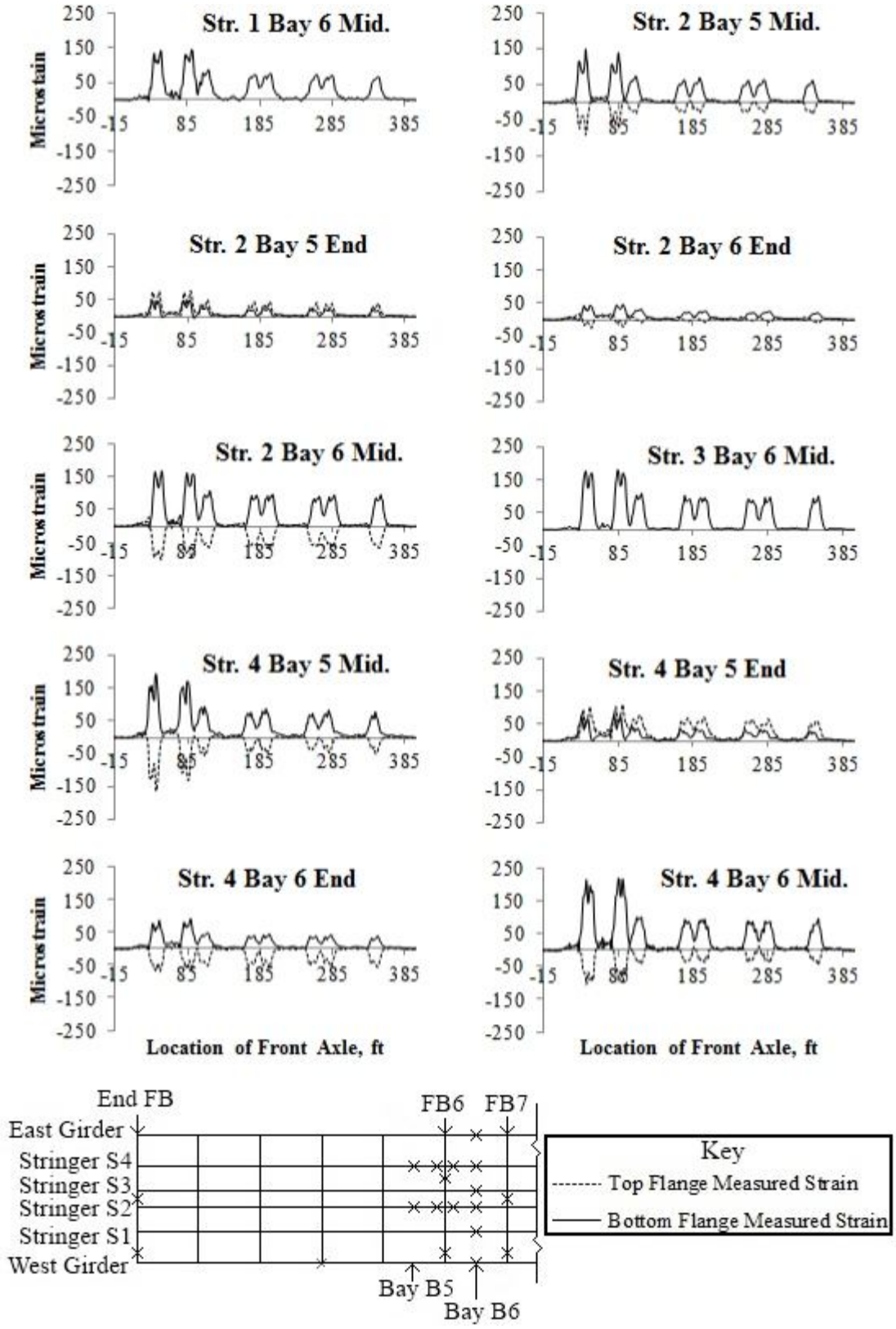

Figure A16: Measured strain data for Train 6 (cont.).

Distribution List

Douglas Adams
Purdue University
Director, Center for Systems Integrity
1500 Kepner Rd
Lafayette, IN 47905

Paulo Anchieta da Silva
Embraer
Av. Brigadeiro Faria Lima 2.170
12227-901 São José dos Campos, São Paulo
BRAZIL

Hesham Azzam
HAHN Spring Ltd
Little Spinney, Copse Lane
Chilworth, Southampton
United Kingdom SO16 7JY

Ted Barber
New Mexico Dept. of Transportation
Bridge Design Section
1120 Cerrillos Road
P.O. Box 1149
Santa Fe, NM 87504

Christian Boller
Fraunhofer Institut für zerstörungsfreie
Prüfung (IZFP)
Campus E3.1
66123 Saarbrücken, Germany

DOT/RSPA Volpe National Transportation
Systems Center
Environment, Safety and Health
Attn: Aviva Brecher
55 Broadway, DTS-30
Cambridge, MA 02142-1093

Byron Burns
Director Bridge Engineering
Burlington Northern Santa Fe Railway Co.
4515 Kansas Ave
Kansas City, KS 66106-1199

Jimmy Camp, PE
District Engineer
New Mexico Department of Transportation
South Hwy 85
PO Box 10
Las Vegas, NM 87701

Fu-Kuo Chang
Stanford University
Dept. of Aeronautics and Astronautics
Durand Building Room 250
Stanford, CA 94305

Federal Highway Administration
Attn: Chien-Tan Chang
MS HRDI-01
6300 Georgetown Pike
McLean, VA 22101

Roger Cheng
Dept. of Civil & Environmental Engineering
220 Civil/Electrical Building
University of Alberta
Edmonton, Alberta, Canada, T6G 2G7

Brett Commander
Chief Analysis Engineer
Bridge Diagnostics, Inc.
1995 57th Court North, Ste. 100
Boulder, CO 80301-2810

William Cox,
Texas Department of Transportation
Director of Bridge Division
125 E. 11th Street
Austin, TX 78701-2483

Andrew Daumueller, EIT
PhD Student
200 Cervantes Vlg Apt D2
Las Cruces, NM 88001

Chris Davis
Boeing
Structural Health Management
Boeing Research and Technology
MC: 42-25
Seattle, WA 98124-2207

Mark Derriso
AFRL/VASA
2130 8th St.
Wright-Patterson AFB, OH 45433-7542

Steve Dick, PE, SE, PhD
Senior Bridge Engineer
TranSystems Corporation
2400 Pershing Rd. Ste. 400
Kansas City, MO 64108

Alvin Dominguez, PE
Secretary of Transportation
New Mexico Department of Transportation
1120 Cerrillos Rd
PO Box 1149
Santa Fe, NM 87504-1149

Charles Farrar
Los Alamos National Laboratory
PO Box 1663
Los Alamos, NM 87545

University of California, Irvine
Henry Samueli School of Engineering
Attn: Maria Feng
Irvine, California 92697-2175

Robert Florom
Transportation Technology Center Inc.
55500 DOT Road
PO Box 11130
Pueblo, CO 81001

Peter Foote
BAE Systems
Sowerby Bldg. FPC 267
PO Box 5 Filton
Bristol BS34 7QW United Kingdom

Earl Franks
New Mexico Dept. of Transportation
2912 E. Pine Street
Deming, NM 88030

Ian Friedlander
Federal Highway Administration
6300 Georgetown Pike
MS - HRDI-03 Rm F211
McLean, VA 22101

Dave Galella
FAA WJ Hughes Technical Center
AJP-6360
Atlantic City Int'l Airport, NJ 08405

Eric Gleason
Director of Public Transportation
Texas Department of Transportation
Director of Bridge Division
125 E. 11th Street
Austin, TX 78701-2483

Grant Gordon
Honeywell Engines & Systems
1944 E. Sky Harbor Circle
M/S 2101-203
Phoenix, AZ 85034

Daniel Hebért
Transport Canada
330 Sparks Street
Ottawa, Ontario K1A 0N5
CANADA

Derrick Hongerholt
Goodrich Corporation
Advanced Sensors Technical Center
14300 Judicial Road
Burnsville, MN, 55306-4898

Jeong-Beom Ihn
Boeing Research & Technology
9725 East Marginal Way South, MC 42-25
Seattle, WA 98108

Dan Inman
Virginia Tech
Center for Intel. Material Sys. & Structures
Department of Mechanical Engineering
310 Durham Hall, Mail Code 026
Blacksburg, VA 24061

Firdausi Irani
Transportation Technology Center Inc.
55500 DOT Road
PO Box 11130
Pueblo, CO 81001

Ricardo Jacquez, PE, PhD
Dean of Engineering
New Mexico State University
PO Box 30001 MSC 3449
Las Cruces, NM 88003-8001

David Jauregui, PE, PhD
Associate Professor
New Mexico State University
Department of Civil Engineering
PO Box 30001 MSC-3CE
Las Cruces, NM 88003-8001

Xiaoning Jiang
North Carolina State University
Dept. of Mech. & Aerospace Engineering
Campus Box 791
Raleigh, NC 27695

Semih Kalay
Transportation Technology Center Inc.
55500 DOT Road
PO Box 11130
Pueblo, CO 81001

Seth Kessler
Metis Design Corporation
10 Canal Park, Suite 601
Cambridge, MA 02141

Gary Kinchen, PE
State Bridge Rating Engineer
New Mexico Department of Transportation
1120 Cerrillos Rd
PO Box 1149
Santa Fe, NM 87504-1149

Jake Kononov
Colorado Department of Transportation
DTD Applied Research and Innovation Branch
Shumate Bldg, 4201 E Arkansas Ave
Denver, CO 80222

Andrew Kornecki
Dept. of Computer and Software Eng.
Embry Riddle Aeronautical University
600 S. Clyde Morris Blvd
Daytona Beach, FL, 32114

Dy Le, Chief
Mechanics Division
Vehicle Technology Directorate
(AMSRD-ARL-VT-MD)
U.S. Army Research Laboratory
Building 1120-A
APG, MD 21005

Mark Leonard
Colorado Department of Transportation
4201 E. Arkansas Avenue
Staff Bridge Rm 107
Denver, CO 80222

Marcias Martinez
Nat'l Research Council Canada
1200 Montreal Rd, Bldg. M-14
Ottawa, Ontario K1A 0R6
CANADA

Scott McClure
Research Bureau Chief
NMDOT Research Bureau
PO Box 94690
Albuquerque, NM 87119-4690

Bill McCroskey
Intl Health Monitoring Systems
444 E. 2nd St.
Dayton, Ohio 45402

Richard Miller
Utah DOT
4501 South 2700 West
PO Box 148470
Salt Lake City, UT 84114-8470

Steve Millsap
Burlington Northern Santa Fe Railway Co.
2600 Lou Menk Dr - NOC 3
Fort Worth, TX 76131-2830

Martha Mitchell, PhD
Engineering Research Center
New Mexico State University
PO Box 30001 MSC 3805
Las Cruces, NM 88003-8001

Eric Munley
Federal Highway Administration
6300 Georgetown Pike
MS - HRDI-07
McLean, VA 22101

Arizona DOT
Attn: Jean Nehme, P.E.
205 S 17th Ave
MD 269E
Phoenix, AZ 85007

Toshimichi Ogisu
Commercial Programs Aerospace Company
Fuji Heavy Industries LTD,
1-1-11 Yonan, Utsunomiya, Tochigi,
320-8564, JAPAN

Ruben Pena
Transportation Technology Center Inc
55500 DOT Road
PO Box 11130
Pueblo, CO 81001

Kara Peters
North Carolina State University
Dept. of Mechanical and Aerospace Engineering
Campus Box 791
Raleigh, NC 27695

Bill Prosser
NASA Langley Research Center
Mail Stop 231
Hampton, VA 23681-0001

Sheila Rimal Duwadi
Federal Highway Administration
6300 Georgetown Pike
McLean, VA 22101

Ricardo Rulli
Embraer
Av. Brigadeiro Faria Lima 2.170
12227-901 São José dos Campos, São Paulo
BRAZIL

Luis Santos
Embraer
Av. Brigadeiro Faria Lima 2.170
12227-901 São José dos Campos, São Paulo
BRAZIL

Jeff Schultz
Bridge Diagnostics, Inc.
1995 57th Court North, Ste. 100
Boulder, CO 80301-2810

Edgar Small
Department of Civil Engineering
The Catholic University of America
620 Michigan Avenue
Washington, DC 20064

Hoon Sohn
Korea Institute of Science and Technology
Civil and Envir. Engineering Dept.
291 Daehak-Ro, Yuseong-Gu
Daejeon 305-701
Republic of South Korea

Holger Speckmann
AIRBUS Deutschland GmbH
Dept.: ESWNG / Testing Technology
Germany
Huenefeldstr. 1-5
28199 Bremen, GERMANY

Tom Styrbicki
Minnesota Department of Transportation
Bridge Office
3482 Hadley Avenue North
Oakdale, MN 55128

Paul Swindell
FAA WJ Hughes Technical Center
AJP-6360
Atlantic City Int'l Airport, NJ 08405

Research and Innovative Technology
Administration (RITA)
Attn: K. Thirumalai
Nassif Building, Room 7110
400 7th St., SW
Washington, DC 20590

Nilesh Tralshawala
General Electric - Energy
Advanced Controls and Sensors
1 River Road
Schenectady, NY 12345-6000US

Ray Trujillo, PE
State Bridge Engineer
New Mexico Department of Transportation
1120 Cerrillos Rd
PO BOX 1149
Santa Fe, NM 87504-1149

Moshe Tur
TEL AVIV UNIVERSITY
School of Electrical Engineering
Ramat Aviv, Tel Aviv 69978, ISRAEL

Jon Voeller
AFRL/RXSST
4750 Staff Dr
Bldg 3220, Rm 12
Tinker, AFB, OK 73145-3317

Jeff Vigil, PE
State Bridge Management Engineer
New Mexico Department of Transportation
1120 Cerrillos Rd
PO Box 1149
Santa Fe, NM 87504-1149

Douglass Volkman
Los Alamos National Laboratory
PO Box 1663
Los Alamos, NM 87545

Ken White, PE, PhD
Ret. Professor & Hwy Commissioner
New Mexico State University
Department of Civil Engineering
PO Box 30001 MSC-3CE
Las Cruces, NM 88003-8001

Matt Witte
Transportation Technology Center Inc.
55500 DOT Road
PO Box 11130
Pueblo, CO 81001

Dingyi Yang
Texas DOT Bridge Division
Construction & Maintenance Branch
125 E. 11th Street
Austin, TX 78701

Sandia National Labs:
MS-0724 Jill Hruby, 6000
MS-0769 Ron Moya, 6600
MS-0762 Brad Parks, 6630
MS–0768 Roberto Mata, 6620
MS-0615 Dennis Roach, 6620
MS-0782 Steve Heffelfinger, 6621
MS-0775 Robert Baca, 6622
MS-0790 Mark Soo Hoo, 6623

MS-0615 Roger Hartman, 6624
MS-0615 Mike Bode, 6624
MS-0615 Randy Duvall, 6624
MS-0615 Michael Holle, 6624
MS-0615 Stephen Neidigk, 6624
MS-0615 Tom Rice, 6624
MS-1451 Anthony Medina, 2500
MS-1072 Rita Gonzales, 1750
MS-0359 Donna Chavez, 1911
MS-0359 Yolanda Moreno, 1911
MS-1108 Mike Hightower, 6111

MS-0899 RIM - Reports MGMT, 9532

THIS PAGE INTENTIONALLY LEFT BLANK

Sandia National Laboratories